

# Air Flow in a High Aspect Ratio Heat Sink

by

Jonathan Michael Allison

B.S. Mechanical Engineering, Rice University, 2008

SUBMITTED TO THE DEPARTMENT OF AERONAUTICS AND  
ASTRONAUTICS  
IN PARTIAL FULFILLMENT OF THE REQUIREMENTS FOR THE  
DEGREE OF

MASTER OF SCIENCE

AT THE

MASSACHUSETTS INSTITUTE OF TECHNOLOGY

June 2010

© Massachusetts Institute of Technology 2010. All rights reserved.

Signature of Author .....  
Department of Aeronautics and Astronautics  
June 2010

Certified by .....  
John G. Brisson  
Professor of Mechanical Engineering  
Thesis Supervisor

Accepted by .....  
Eytan H. Modiano  
Associate Professor of Aeronautics and Astronautics  
Chair, Committee on Graduate Students

# Air Flow in a High Aspect Ratio Heat Sink

by

Jonathan Michael Allison

Submitted to the Department of Aeronautics and Astronautics  
on May 21, 2010, in partial fulfillment of the  
requirements for the degree of  
Master of Science

## Abstract

The increasing heat output of modern electronics requires concomitant advances in heat sinking technology: reductions in thermal resistance and required pumping power are necessary. This research covers the development of a novel type of air-cooled heat sink, in particular the air flow through such a heat sink. The research is carried out through theory, computation, and experiment. A nondimensionalization is carried out to determine scaling laws for such heat sinks. Correlations are provided for the prediction of performance of similar heat sinks.

Using these scaling laws a heat sink with an air flow volume of  $35 \text{ cm}^3$  is described with a convection thermal resistance of  $0.43 \text{ KW}^{-1}$  for a pumping power of  $0.72 \text{ W}$ .

Thesis Supervisor: John G. Brisson

Title: Professor of Mechanical Engineering

# Table of Contents

<b>Abstract</b> . . . . .	2
<b>Table of Contents</b> . . . . .	3
<b>List of Figures</b> . . . . .	6
<b>List of Tables</b> . . . . .	8
<b>Nomenclature</b> . . . . .	9
<b>Abbreviations</b> . . . . .	13
<b>Acknowledgements</b> . . . . .	14
<b>1 Introduction</b> . . . . .	15
1.1 Motivation . . . . .	15
1.1.1 Current Air-Cooled Heat Sinks . . . . .	15
1.1.2 An Improved Design . . . . .	16
1.2 Requirements . . . . .	17
1.3 Literature Review . . . . .	18
1.4 Thesis Overview . . . . .	18
<b>2 Correlation Based Model</b> . . . . .	20
2.1 Modeling Assumptions . . . . .	20
2.2 Input Variables . . . . .	21
2.3 Lengths and Areas . . . . .	22
2.4 Blade Shape . . . . .	24
2.5 Rates . . . . .	26
2.6 Pathlines . . . . .	27
2.7 Air Properties . . . . .	29
2.8 Dimensionless Numbers . . . . .	29
2.9 Power and Pressure . . . . .	31
2.10 Air and Stator Temperature . . . . .	34
2.11 Thermal Resistance . . . . .	35
2.12 Single Layer Model . . . . .	39
2.13 Buoyancy Effects . . . . .	41

---

2.14 Rotors as Fluid Bearings . . . . .	41
2.15 Conclusions . . . . .	44
<b>3 Nondimensionalization . . . . .</b>	<b>45</b>
3.1 Introduction . . . . .	45
3.2 Independent Parameters . . . . .	45
3.3 Dependent Parameters . . . . .	46
3.4 Performance Parameters . . . . .	47
<b>4 Computational Model . . . . .</b>	<b>49</b>
4.1 Model Description . . . . .	49
4.2 Computational Model Results . . . . .	52
4.3 Computational Model Conclusions . . . . .	56
<b>5 Experimental Model . . . . .</b>	<b>58</b>
5.1 Description of Apparatus . . . . .	58
5.2 Power Calibration . . . . .	59
5.3 Air Flow Experiments . . . . .	61
5.3.1 Hot-Wire Anemometer Technique . . . . .	61
5.3.2 Outflow Jet Entrainment . . . . .	62
5.4 Heat Transfer Experiments . . . . .	64
5.4.1 Heat Loss Analysis . . . . .	66
5.5 Results and Analysis . . . . .	67
5.6 Correlations and Design Charts . . . . .	69
<b>6 Multilayer Assembly . . . . .</b>	<b>77</b>
6.1 Design . . . . .	77
6.2 Construction . . . . .	79
6.3 Performance . . . . .	80
<b>7 Comparisons . . . . .</b>	<b>85</b>
7.1 Correlation based model versus experiment . . . . .	85
7.2 CFD versus experiment . . . . .	86
<b>8 Conclusion and Future Work . . . . .</b>	<b>91</b>
8.1 Future Work . . . . .	91
8.2 Conclusion . . . . .	92
 <b>Appendices</b>	
<b>A Blade Shape . . . . .</b>	<b>93</b>
<b>B Inflow Heat Transfer . . . . .</b>	<b>94</b>

---

<b>C Solid Mechanics</b> . . . . .	98
C.1 Statics . . . . .	98
C.2 Dynamics . . . . .	99
C.2.1 Natural Frequencies . . . . .	99
C.2.2 Shock Loads . . . . .	100
C.2.3 Centrifugal Acceleration . . . . .	100
<b>D Heat Sink Quantities</b> . . . . .	103
<b>E Selected Raw Data</b> . . . . .	105
E.1 Hot-Wire Anemometer Data . . . . .	105
E.2 Temperature Data . . . . .	110
<b>Bibliography</b> . . . . .	113

# List of Figures

1.1	PHUMP diagram . . . . .	17
2.1	Flow diagram . . . . .	23
2.2	Rotor shape . . . . .	25
2.3	Air velocities . . . . .	28
2.4	Reynolds numbers . . . . .	30
2.5	Heat transfer coefficient . . . . .	32
2.6	Temperature of air and stators . . . . .	36
2.7	Heat sink performance prediction . . . . .	38
2.8	Heat sink performance prediction – single layer . . . . .	40
2.9	Fluid bearings diagram . . . . .	41
2.10	Fluid bearings performance . . . . .	43
3.1	Length dimensions . . . . .	46
4.1	Computational model grid . . . . .	51
4.2	Computational model pathlines . . . . .	52
4.3	CFD model performance . . . . .	54
5.1	Experimental setup . . . . .	60
5.2	Hot-wire anemometer velocity components . . . . .	63
5.3	Jet entrainment and heat loss mechanisms . . . . .	65
5.4	Exit plane air velocity and temperature . . . . .	68
5.5	Comparison of fit equations and data . . . . .	71
5.6	Contours of $R$ and $\dot{W}$ . . . . .	73
5.7	Single layer experiment performance . . . . .	76
6.1	Drawing of multilayer assembly . . . . .	78
6.2	Multilayer assembly photo . . . . .	79
6.3	Drawing of jig for multilayer assembly . . . . .	81
6.4	Multilayer assembly construction process . . . . .	82
6.5	Multilayer assembly construction process, continued . . . . .	83
7.1	Compiled performance plots . . . . .	87
7.2	Compiled mass flow plots . . . . .	88
7.3	Comparison of performance of CFD versus experiment . . . . .	90

---

B.1	Inflow convection . . . . .	96
B.2	Inflow Nusselt number . . . . .	97
C.1	Centrifugal blade straightening . . . . .	102

# List of Tables

2.1	Input variables . . . . .	21
4.1	Specifications of CFD models . . . . .	55
D.1	Pareto optimal design . . . . .	103
D.2	Pareto optimal design, continued . . . . .	104
E.1	Hot wire anemometer raw data . . . . .	105
E.2	Thermocouple raw data, 1 . . . . .	110
E.3	Thermocouple raw data, 2 . . . . .	111
E.4	Thermocouple raw data, 3 . . . . .	111
E.5	Thermocouple raw data, 4 . . . . .	111
E.6	Thermocouple raw data, 5 . . . . .	112



# Nomenclature

Note that some symbols are used to refer to several different variables. When this is the case, alternate meanings are separated by a comma.

## Roman Symbols

$A$	area
$AR_{cs}$	aspect ratio of flow channel cross section
$B$	blade aspect ratio
$c_p$	heat capacity of air
$c_0, c_1$	hot-wire anemometer calibration coefficients
$C$	constant of integration
$C_f$	flow coefficient
COP	coefficient of performance
$D_h$	hydraulic diameter
$E$	elastic modulus
$f$	angular speed, friction factor
$F$	force
$g$	gravitational acceleration
$G$	flow channel aspect ratio
$Gr$	Grashof number
$h$	height, heat transfer coefficient
$i, j$	indices
$I$	motor current, second moment of area
$\mathcal{I}$	inlet size ratio
$k$	yaw factor, beam stiffness
$K_e$	motor back EMF constant
$K_i$	inlet pressure loss coefficient
$K_{\text{turn}}$	turning loss coefficient
$l$	length
$L$	length of heat sink side
$L_s$	length of shaft
$m$	mass
$\dot{m}$	mass flow rate

---

$n$	number of discrete points
$n_b$	number of blades per rotor
$n_r$	number of rotors
$n_s$	number of stators
$Nu_L$	Nusselt number on top insulation surface
$\Delta p$	gage pressure
$\mathcal{P}(r)$	wetted perimeter of a single stator
$Pr$	Prandtl number
$q$	dynamic pressure
$\dot{Q}$	thermal power sunk by heat sink
$\dot{Q}_{\text{bot}}$	thermal power lost through bottom insulation
$\dot{Q}_{\text{in}}$	power into resistive heaters
$\dot{Q}_{\text{screws}}$	thermal power lost through screws
$\dot{Q}_{\text{sides}}$	thermal power lost through sides
$\dot{Q}_{\text{top}}$	thermal power lost through top insulation
$r$	radius
$R$	thermal resistance
$R_{\text{arm}}$	armature electrical resistance of motor
$Re$	Reynolds number based on air velocity in flow channel
$Re_i$	inlet Reynolds number
$Re_{\text{radial}}$	Reynolds number based on radial velocity
$Re_{\omega}$	rotational Reynolds number
$t$	thickness
$T$	air temperature
$T_o$	outlet air temperature
$\bar{T}_o$	bulk outlet air temperature
$T_s$	stator wall temperature
$v$	air velocity
$V$	motor voltage, beam shear force
$\dot{V}$	volumetric flow rate
$w$	width, distributed load (force per length)
$\dot{W}_i$	motor power input
$\dot{W}_{\eta}$	motor power loss
$\dot{W}$	pumping power
$\dot{W}_m$	mechanical power loss
$x$	coordinate along exit plane & orthogonal to $y$ and $z$
$y$	coordinate along shaft axis & orthogonal to evaporator
$\tilde{y}$	locations of rotors and stators along shaft axis
$z$	coordinate normal to exit plane

---

## Greek Symbols

$\alpha$	yaw angle of hot-wire probe with respect to flow direction
$\beta$	volumetric thermal expansion coefficient of air
$\beta_b$	blade angle
$\gamma$	angle of flow with respect to the normal to the exit plane
$\delta$	beam deflection
$\varepsilon$	exchanger effectiveness
$\eta$	motor efficiency
$\theta$	azimuthal angle
$\kappa$	thermal conductivity of air
$\kappa_{\text{insul}}$	thermal conductivity of thermal insulation
$\mu$	dynamic viscosity of air
$\xi$	pathline coordinate
$\rho$	density of air
$\sigma$	slip factor, stress
$\phi$	maximum allowable tilt angle of rotor
$\omega$	angular velocity of rotor

---

## Subscripts

1	fundamental mode
<i>a</i>	air
amb	ambient
<i>A</i>	sensor orientation A
<i>b</i>	blade
bot	bottom side
<i>B</i>	sensor orientation B
<i>c</i>	air flow channel, critical speed
conc	concentrated load
<i>cr</i>	camber line
<i>cs</i>	cross section
cut	cutoff
dev	developing flow
dif	difference
<i>e</i>	evaporator, effective
entrain	entrainment
entry	thermal entry region
<i>ff</i>	flow field
<i>g</i>	gap
<i>h</i>	hot-wire anemometer
<i>i</i>	inlet
<i>L</i>	lift
<i>m</i>	motor
max	maximum
<i>N</i>	normal direction
<i>o</i>	outlet
<i>r</i>	rotor
rel	relative
<i>s</i>	stator, shaft, per unit span
side	side wall (of experimental apparatus)
<i>t</i>	blade tip
top	top side
tot	total
<i>T</i>	transverse direction
unload	condition without rotor
<i>W</i>	weight
<i>y</i>	<i>y</i> direction
$\theta$	azimuthal direction
*	normalized

# Abbreviations

CAD	Computer Aided Design
CFD	Computational Fluid Dynamics
DARPA	Defense Advanced Research Projects Agency
EMF	Electromotive Force
EVA	Ethylene-Vinyl Acetate
MACE	Microtechnologies for Air-Cooled Exchangers (DARPA program)
NACA	National Advisory Committee for Aeronautics
PHUMP	High-Power Pumped Heat Exchanger
PTFE	Polytetrafluoroethylene

# Acknowledgements

An undertaking as large as a graduate education and thesis is not possible without the help and understanding of many people. I thank everyone who has been a positive influence in my life even though you are too numerous to mention by name.

I thank Professor Brisson and Professor Wang for challenging me and directing me in this project. I thank Dr. Stu Jacobson for his help in getting me off on the right foot. Thanks to Naomi Zabel who helped order and build many parts of the experiment and to Ayaboe Edoh who performed many of the experiments. Thanks to Dr. Barbara Hughey for generously lending use of her hot-wire anemometer. Thanks also to DARPA MACE program manager, Dr. Thomas Kenny. This research is funded by DARPA grant # W31P4Q-09-1-0007.

I thank my fellow students in the Cryogenics Lab: Wayne Staats, Barbara Botros, Martin Segado, Alonso Dominguez, Jake Hogan, and Kevin DiGenova, for their helpful insights and friendliness. I particularly thank Wayne Staats and Martin Segado without whom several parts of this thesis would look markedly different. I thank David Jenicek for his camaraderie and offers of free beers. I thank my Mates: Zach Bailey, Hemant Chaurasia, Sydney Do, Pritesh Mody, Hiten Mulchandani, and Russ Stratton for their stress relief.

Lastly, I would like to thank my family who have supported me at all times.

*You will keep in perfect peace  
him whose mind is steadfast,  
because he trusts in you.  
Isaiah 26:3*

# Chapter 1

## Introduction

The ever increasing computational power of modern electronics systems necessarily increases the concentration of waste heat on the chip. Without proper cooling, central processing units are easily capable of overheating and destroying themselves. To maintain electronics' temperatures at a reasonable level, new heat sinking approaches are needed. Air-cooled heat sinks are a simple, proven technology, that require only a small volume and input electrical power. Herein, an air-cooled heat sink with an improved design is proposed.

### 1.1 Motivation

#### 1.1.1 Current Air-Cooled Heat Sinks

The geometry of current air-cooled heat sinks consists of a baseplate, made of copper or aluminum, which is compressed against the heat source via screws with a layer of thermal grease to reduce the contact resistance between heat source and baseplate. The purpose of the baseplate is to provide a stiff mechanical support with minimal thermal resistance.

The opposite side of the baseplate is connected to an extended surface consisting of fins, shaped either as pins or as sheets, which are typically oriented normal to the baseplate. The fins are also typically copper or aluminum. These fins function to increase the surface area over which heat is able to transfer from heat sink to air. The convection over the fins is increased by an axial flow fan that is placed on the side of or on top of the heat sink to enhance convection by forcing air flow between the fins. Although not strictly required in a heat sink design, a fan is generally necessary to keep thermal resistance acceptably low.

Optionally, heat pipes may be incorporated into the heat sink design to reduce thermal resistance. Heat pipes are sealed tubes containing a two-phase fluid. When there is a temperature difference across the length of the heat pipe, and the hot side temperature is greater than the boiling temperature of the fluid, the fluid boils absorbing heat at high temperature and the vapor moves through the center of the pipe toward the cool side where it condenses releasing heat at a cooler temperature. A wick structure, using capillary pressure, draws the condensate back along the inside walls of the heat pipe to the boiling section to close the cycle. As long as the capillary pressure rise in the wick is greater than the sum of all pressure losses in the system, the fluid will flow without the benefit of any pumps or input pumping power. Thus heat pipes can be thought of, externally, as a material with very high thermal conductivity in the axial direction. Heat pipes are often incorporated into the base plate of heat sinks and pierce orthogonally through the fins. This circumvents the thermal resistance through the fins and allows the heat sink to keep

the far ends of the fins at a higher temperature, closer to that of the baseplate. Heat pipes thereby decrease the thermal resistance of the heat sink.

### 1.1.2 An Improved Design

The heat sink style described above is the standard electronics heat sink, with most current designs making only slight variations on the theme. The heat sink design discussed in this thesis, named PHUMP, is shown in Fig. 1.1. The rationale for the PHUMP heat sink design will first be described and terms introduced, and then the configuration will be discussed in reference to Fig. 1.1.

The most important contributor to the thermal resistance in the heat sink is the convection thermal resistance between the ambient air and the fins. Current designs have the fan remotely located from the fins, allowing separate manufacture of fan and fins, but with an associated increase in thermal resistance. This novel design calls for a series of fan rotors on the same shaft that are interdigitated among the fins to enhance the air flow over each fin. As the rotor blades pass over each fin, they shear off the thermal boundary layer, thereby increasing the temperature gradient in the air at the fin walls and thus increasing the heat flux through the fins.

The rotors are centrifugal fans, meaning that they impart an azimuthal velocity to the air, causing a centrifugal acceleration that blows the air radially outwards. The air blown out of the heat sink is replaced by new air that is drawn into the center of the heat sink. Air enters the heat sink through a circular inlet at the top, and turns radially outward through each air flow channel. The rotors are connected to a central shaft which is in turn connected to the motor that drives the rotors.

The second main contributor to the overall thermal resistance is the fins. Due to their small cross-sectional area, fins tend to have a rather high thermal resistance over their length. As discussed previously, this can be mitigated by heat pipes. However, heat pipes are typically designed to intersect the fins orthogonally and have a contact resistance with the fins, increasing the thermal resistance of these heat sinks. In this new design, the fins are themselves the condensing section of the heat pipe, thus the fins are also referred to as stators or condensers. Additionally, the baseplate is to be the evaporator section of the heat pipe system. This combination of fins and heat pipes should make the thermal resistance in the stators all but negligible. The design and operation of the heat pipe component of the heat sink will not be dealt with herein.

Fig. 1.1 is a cross-sectional diagram that shows the configuration and operation of the PHUMP. The orientation of the design is such that the evaporator is at the bottom of the heat sink, the shaft is oriented orthogonal to the evaporator, with the rotors spinning in a plane parallel to that of the evaporator. The stators are likewise parallel to the evaporator and are linked to it via vertical pipes that exchange liquid and vapor between the evaporator and stators. The motor is a radial flux permanent magnet synchronous motor, mounted to the shaft at the top of the heat sink, with a hole in its center to allow air flow through it. The motor design is described in an upcoming Master's Thesis by D. Jenicek. Air enters the system from the top, passing through the inlet. Next, the air turns in between the



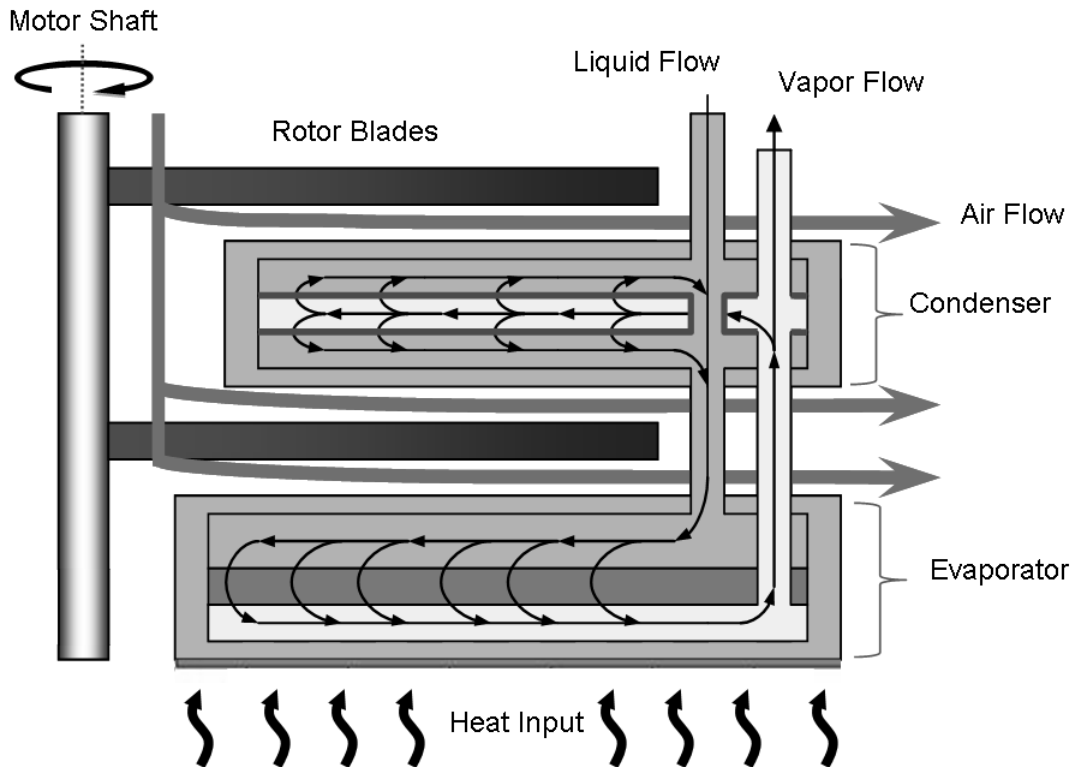


Figure 1.1: Cross-sectional diagram of the PHUMP design. Air enters at top left and is blown to the right across the stators by rotors connected to a common shaft driven by a permanent magnet synchronous motor. Two-phase fluid evaporates in the evaporator and flows through vertical pipes to the stators where it condenses and returns via wicking structure to the evaporator.

stators. This region between the stators is referred to as the flow channel. The rotor drives the air across the higher temperature stators, heating the air in the process, and sends it out of the heat sink.

## 1.2 Requirements

The requirements specified for the PHUMP are as follows. The maximum allowed temperature rise above ambient is 50 K and the temperature of the bottom of the evaporator must not go over 80 °C. The heat sink must dissipate at least 1000 W of heat into the air with 33.3 W of electrical power available to create forced convection. The heat sink must fit within a cube 4 inches (101.6 mm) to a side. Additionally, the heat sink must sustain performance in the presence of 10 g shock loads of 11 ms duration. It must also sustain storage temperatures ranging between -54 °C and 100 °C. Finally, the operating life of

the device must be greater than 10,000 hours.

### 1.3 Literature Review

Grimes et al. have studied the performance of commercial miniature, high aspect ratio, radial fan heat sinks for portable electronics applications [1]. The exhaust of the fan is routed toward a single exit and impinges on a heat transfer surface outside of the region of the fan's rotation. In that research, two different heat transfer surfaces were considered, 'finned' and 'finless'. The finned heat sink had straight fins immediately downstream of the fan exhaust, which were optimally spaced and connected to a heated surface on the perimeter of the flow. In contrast, the finless design had no fins and only a heated surface on the perimeter of the flow. For this thin flow (3.5 mm tall by 8.1 mm wide), the finless design provided reduced thermal resistance due to its lower pressure drop and higher flow rate in comparison to the finned heat sink. This suggests that the interplay between maximizing heat transfer surface area and minimizing pressure drop for air-cooled heat sinks gives an optimal channel thickness (where thickness refers to the thinnest dimension of the channel cross section) on the order of 3 mm which corroborates with commercially available heat sinks and is in the range of dimensions explored in this work.

Several authors have explored heat transfer between rotating disks and stators [2][3]. That research has been aimed toward understanding heat transfer in gas turbines. Thus, the flow regimes (rotational Reynolds numbers) and geometries (flat disk or bladed rotors, open or closed peripheral boundaries) differ significantly between the previous research and the current research. Webb advocates the analysis and understanding of electronics heat sinks as heat exchangers [4]. In this work, a nondimensionalization of fan-driven heat sinks gives nondimensional numbers relevant to both heat exchangers and turbomachines. This indicates that fan-driven heat sink should be thought of as both heat exchangers and turbomachines, and corroborates Webb.

In the Request for Proposals for this program, DARPA, specified the current state-of-the-art in air-cooled heat sinks as a heat sink comprising the volume of a 4 inch cube with a thermal resistance of  $0.2 \text{ KW}^{-1}$ , a thermal power dissipation of 1000 W, and an electrical power consumption of 100 W [5]. Thus the goals for this novel heat sink represent a significant advance on the current state-of-the-art.

### 1.4 Thesis Overview

This thesis focuses on the air flow through the heat sink described above. The thermal resistance associated with the air convection is expected to be the largest thermal resistance in the system due to the low heat capacity of air in comparison to the two-phase liquid in the heat pipe. Thus, improvements in the heat transfer in the air flow through the heat sink will yield the best improvements in thermal resistance and reduce the required heat transfer surface area which reduces the complexity of assembly by requiring fewer stators

with larger channel spacings between them.

The initial design of the improved heat sink was a correlation based model, done via computation of performance based on input design criteria, friction factors, and Nusselt numbers as listed in the literature for similar geometries. The next stage of design was to model the heat sink with computational fluid dynamics program to relate thermal and fluid flows. Then a single layer (one rotor and one stator) experimental device was built and tested. Finally a demonstration device of the heat sink was designed and built that simulates the air flow in a final prototype. Appendices give a Nusselt correlation for an inlet flow geometry and calculations of solid mechanics relevant to the behavior of the rotors and shaft.

## Chapter 2

# Correlation Based Model

The correlation based model takes in correlations from the literature such as friction factors and Nusselt numbers, along with simplifying assumptions to model the performance of the PHUMP heat sink of the type described in Ch. 1.

The analysis of the design will focus primarily on the volume between the rotor and the stator because all of the heat transfer and much of the pressure drop takes place in this region. The corners of the heat sink are neglected, as mentioned in the assumptions section. This assumption is conservative in terms of the resistance, because it underestimates the surface area available for heat transfer, but it is nonconservative for pumping power demands because it underestimates the surface area causing frictional pressure loss.

### 2.1 Modeling Assumptions

Several simplifying assumptions are specified in the correlation based model, please refer to Fig. 2.1 for a diagram of the model. The first assumption is that the preswirl at the beginning of each flow channel is zero, that is the blades are assumed to not induce swirl in the flow before it enters the flow channel. Next, as flow moves through the inlet passage it splits into each of the various rotor layers (shown diagrammatically in Fig. 2.1), the flow is assumed to divide equally among the several flow channels, which is equivalent to saying that the fluidic resistance through the inlet passage is much less than the fluidic resistance through the flow channels. In the flow channel, the azimuthal velocity of the air flow is assumed to be the same as that of the rotor, which is equivalent to assuming that there is no azimuthal flow slip relative to the rotor. As stated above, the stators are modeled as circular disks rather than square plates to maintain symmetry in the cylindrical coordinate system. Also, there is no variation in gravitational potential energy throughout the system because of the low density of air and the small size of the heat sink. The effect of the blades passing over the stator surfaces on the heat transfer is not considered in this model. Instead, the effect of flow development on momentum transfer and heat transfer is considered as the flow enters the flow channels as if there were no passing blades. Also, the rotors are considered to be adiabatic, having no conduction through them. Additionally, convection is assumed to be the primary mode of heat transfer into the air; radiation is neglected. The flow in the flow channel is modeled as an internal flow in a flat duct (an infinite aspect ratio rectangular duct) where both walls (the stator walls) are constant temperature over their length. Lastly, the temperature of the entire surface of the stators is the same and it is determined by changes in the thermal power or thermal resistance and the stator walls share the same temperature. The justification for each of these assumptions will be

Table 2.1: Input variables for the correlation based design

Variable	Description
$\omega$	angular velocity
$h_c$	height of the flow channel
$h_b$	height of the blade
$h_g$	height of the gap
$h_s$	height of the stator
$h_m$	height of the motor
$h_e$	height of the evaporator
$r_s$	radius of the shaft
$r_i$	radius of the inlet
$r_t$	radius of the rotor tip
$n_b$	number of blades per rotor
$w_b$	width of the blade
$\beta_b(r_t)$	blade angle at the tip

considered as they are applied.

## 2.2 Input Variables

A variety of variables can be specified and varied to optimize the performance of the correlation based model. These are listed in Table 2.1, and some are drawn in Fig. 2.1. These variables will now be described.

The angular velocity of the rotor,  $\omega$ , is the angular velocity at which the motor, shaft, and rotors turn; its units are rad/s. Higher  $\omega$  causes higher air velocities and mass flow rates through the heat sink, increasing the Reynolds number of the flow, and decreasing the thermal resistance between the air and the stator surfaces. Increased mass flow rates also increase the pumping power required to turn the fan.

The next several dimensions are length dimensions referred to as ‘heights’ because they all measure lengths in the vertical direction of the device. First, the height of the channel,  $h_c$ , determines the hydraulic diameter and the required manufacturing tolerances.  $h_c$  is depicted in Fig. 2.1 a and b. The height of the blade,  $h_b$ , is the thickness of the blade, affects how well the flow is driven by the blades. Since no slip along the blades is assumed,  $h_b$  is less important in this analysis, but is critical in later experiments. The relative sizes of  $h_c$  and  $h_b$  determine the required manufacturing tolerances. Finally, the distance between the stator and rotor referred to as the gap height,  $h_g$ , is also depicted in Fig. 2.1 b.

The next three length dimensions measure the vertical space consumed by fixed components of the heat sink. The height of the stator,  $h_s$ , is the thickness of the stator, including

the thickness of each wall of the stator, the wick structure, and the open vapor flow space. Sufficient  $h_s$  must be allocated such that the heat pipe is manufacturable and operable. The height of the motor,  $h_m$ , incorporates the vertical space consumed by the top bearing and must be sufficient to produce the required shaft power. The height of the evaporator  $h_e$  must be sufficient to ensure that the evaporator is also manufacturable and operable.

The next several length dimensions measure lengths in the radial direction. The radius of the shaft,  $r_s$ , should be small so as to reduce its consumption of inlet area that would otherwise be available for air flow while large enough to minimize deflection due to whirling. The radius of the inlet,  $r_i$ , is the radius of the holes in the stators allowing air to pass through to lower layers.  $r_i$  must be large enough to keep air velocities manageable in the inlet, while not consuming too much area that could otherwise be used for heat transfer by the stators. The radius of the rotor tip,  $r_t$ , should be as large as possible to increase the azimuthal velocity at the tip without exceeding the allowed width of the heat sink. A larger  $r_t$  allows more pumping power at a given  $\omega$ .

Having more blades on each rotor,  $n_b$ , reduces the amount of flow area available in the flow channel. More blades also increases manufacturing complexity. However, if there are too few blades per rotor, flow will begin to slip around the blades. The in-plane width of the blade,  $w_b$ , also affects the total flow area available in the flow channel. As a result,  $w_b$  tends to decrease as the number of blades increases so that the rotor does not consume excess space in the flow channel.  $w_b$  affects the stiffness of the blade.

As shown in Fig. 2.2,  $\beta_b$  is the angle that the blade chord makes with the radial direction. In this device  $\beta_b$  is a function of the radius.  $\beta_b(r_t)$  is the blade sweep at the tip.  $\beta_b(r)$ , comes into the equation for azimuthal velocity, which has effects on thermal resistance and power consumption.

## 2.3 Lengths and Areas

As depicted in Fig. 2.1 b, the flow channel height is

$$h_c = h_b + 2h_g \quad (2.1)$$

Which is the normal distance between two stators. The total allowed height of the heat sink is 101.6 mm. As many layers of rotors and stators as possible are stacked into the allowed height. Each layer consists of one rotor and one stator and there is one more rotor than stator such that the evaporator has a rotor above it such that the highest stator also has a rotor above it. The total height is then

$$h_{\text{tot}} = n_s h_s + n_r h_c + h_m + h_e \quad (2.2)$$

where  $n_s$  and  $n_r$  are the number of stators and rotors, respectively. This accumulation of heights can be seen in Fig. 2.1 a. It is desirable for a heat sink to have a large heat transfer surface area a large number of stators is the best way to achieve this goal with the PHUMP.

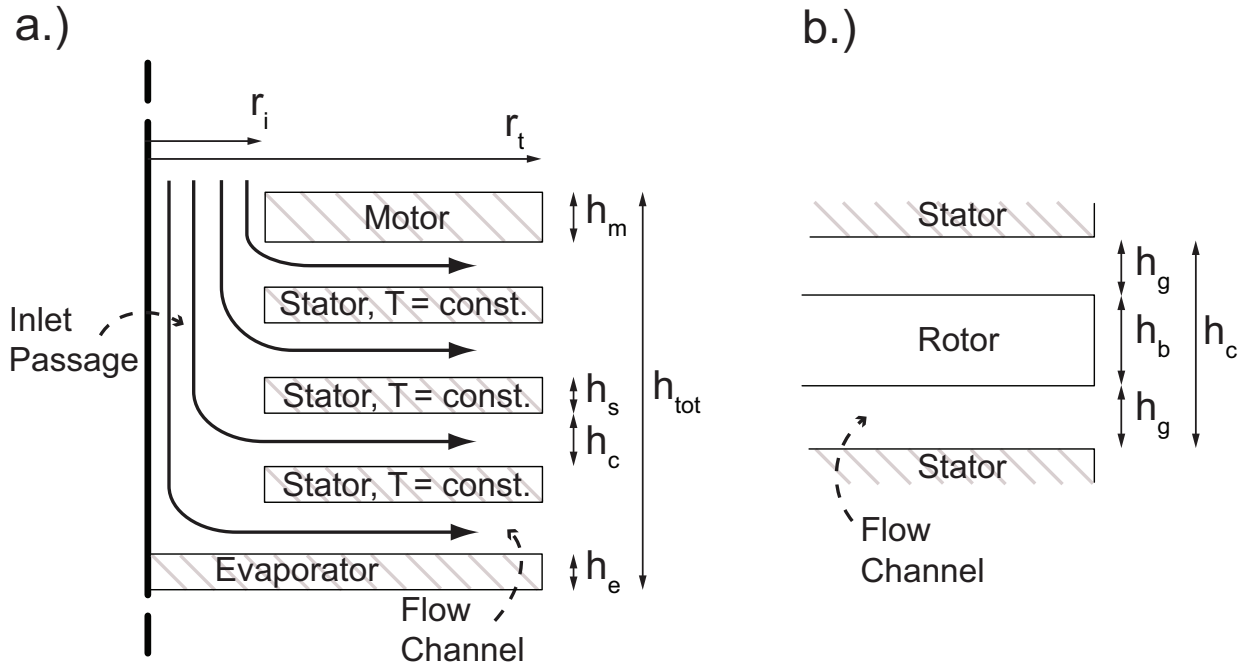


Figure 2.1: **a.)** Cross-sectional flow diagram of correlation based model. The model is rotationally symmetric about the center line marked on the left side of a.). Three stators are shown, although there may be more. The correlation based model sets equal flow splitting among layers and assumes constant stator temperatures. Flow is axially in and radially out. The inlet passage, through which flow passes axially, and a flow channel, through which flow passes radially, are labeled. Also, several length dimensions are labeled. Rotors are not drawn in a.) for simplicity. **b.)** Zoom view of a flow channel and rotor with length dimensions labeled.

Because air velocities and temperatures change as flow moves radially outward in the flow channel from  $r_i$  to  $r_t$ , it is necessary to define a radial coordinate,  $r$ , from  $r_i$  to  $r_t$ .  $r$  is discretized into  $n$  points, the  $i^{\text{th}}$  point being  $r(i)$ . The distance between  $r(i)$  and  $r(i+1)$  is referred to as  $\Delta_r$ .

We also need to define a vector,  $\tilde{y}$ , that defines the locations along the vertical axis at which air is split off.  $\tilde{y}$  is defined from  $h_m$  to  $n_r h_c + n_s h_s + h_m$ , in increments of  $h_s + h_c$  because each subsequent layer is that distance apart.  $j$  will be used here as an index for the vector,  $\tilde{y}$ .

The high aspect ratio of the flow channel makes it a flat duct flow. A flat duct flow is a flow with a rectangular cross-section in which the aspect ratio of the cross-section is large enough that the effect of the two short sides on the fluid mechanics and heat transfer are negligible. The hydraulic diameter of a flat duct is twice the height of the duct, thus the hydraulic diameter of the flow channel is:

$$D_h = 2h_c \quad (2.3)$$

In calculating velocities and flow rates later, the cross sectional areas of the inlet and the flow channel will be needed. The area of the inlet is

$$A_i = \pi(r_i^2 - r_s^2) \quad (2.4)$$

The cross sectional area of the flow through the flow channel increases linearly with  $r$ :

$$A_{cs}(r) = h_c n_r (2\pi r - n_b w_b) \quad (2.5)$$

## 2.4 Blade Shape

The shape of the blades will now be considered. It is desirable for the blades to be aerodynamically shaped to reduce drag and flow separation, however the need for high heat transfer surface area reduces the available vertical height for the blades. Thus the blades will only be designed aerodynamically in the plane of the rotor and be a constant extrusion shape in the axial direction. This means that the cross-section of the blade is rectangular and all of the following discussion of blade shape is with regard to the shape when viewed from overhead, or in the axial direction. This is in contrast to a typical airfoil where the aerodynamic profile faces the oncoming flow. The 2 dimensional shaping of this rotor allows the blade to be made out of plastic or metal sheet with a simple cutting process.

The blade, as viewed from above, is shaped like the back half of a NACA airfoil and the blade angle sweeps linearly from the radial direction at the blade root to  $\beta_B(r_t)$  at the tip. The blade begins at the shaft,  $r_s$ , and goes out to  $r_t$ . The specific blade shapes used in the experiment are discussed in Ch. 5.



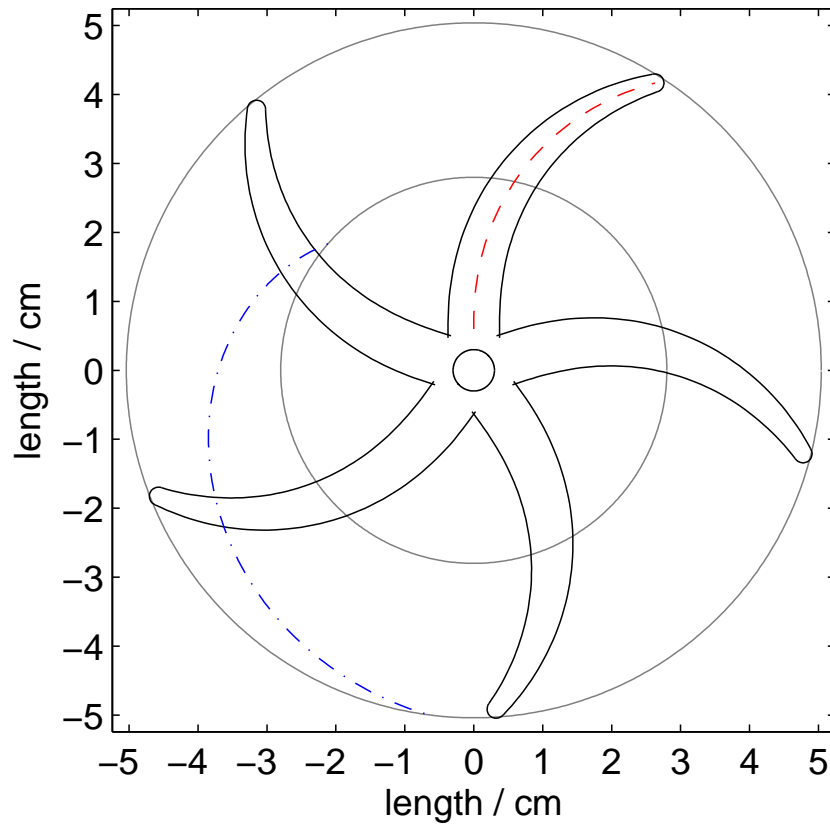


Figure 2.2: Overhead view of rotor shape. Camber line of one blade marked by a red dashed curve, blade edges and shaft marked in black. The innermost black concentric circle is the shaft,  $r_s$ , the next gray concentric circle is the edge of the inlet passage,  $r_i$ , and the outermost gray circle is the edge of the blade path,  $r_t$ . The pathline for a fluid particle entering the flow channel in front of the top blade at operating speed is drawn as a blue dash-dot curve. The angle of the blade at the tip,  $\beta_b(r_t)$ , is marked on the blade in the top right corner.

## 2.5 Rates

Air speeds are determined based on rotor speed, blade angles, and pressure drops and rises across the flow path. The frequency of the motor, in Hz, is

$$f_{\text{Hz}} = \frac{\omega}{2\pi} \quad (2.6)$$

Also, the frequency in rpm is

$$f = 60f_{\text{Hz}} \quad (2.7)$$

The air velocities can be found with the knowledge of the rotor speed, the blade angles, the pressure balance, and the assumptions stated in Sec. 2.1. The velocities described below are plotted in Fig. 2.3. We begin with the radial velocity,  $v_r(r)$ .  $v_r$  is not determined based on blade angles and assumptions about the flow following the rotor. Rather,  $v_r$  is induced by the pressure rise,  $\Delta p_{\text{rise}}$  the fan creates.  $v_r$  continues to increase until the pressure drop,  $\Delta p_{\text{drop}}$ , due to friction and minor losses in the flow path, exactly balances  $\Delta p_{\text{rise}}$ . At steady state operation, the difference of these two pressures,  $\Delta p_{\text{dif}}$ , will be zero.

This problem is fundamentally implicit, in the sense that what the mass flow rate through the system is (relating to what the radial velocity is) determines the pressure drop, while the pressure drop in turn also is a function of the mass flow rate. This system is thus solved with a line search algorithm that begins with an initial assumption for  $v_r$ , evaluates the resultant  $\Delta p_{\text{dif}}$ , and selects a new  $v_r$  that is expected to more closely approximate  $\Delta p_{\text{dif}}$ . The process is iterated until the solution is acceptably accurate.

Because of the recursive nature of this problem, the technique for solving  $v_r$  requires knowledge of terms that have not yet been defined. Suffice to say for now that a ‘for’ loop has been opened from this point and that the initial assumption is  $v_r(r_i) = 2\omega r_i$ .

The azimuthal component of the air velocity is a more direct problem.  $v_\theta(r)$  can be solved by velocity triangle [6]. Equations (2.8) to (2.13) are defined for  $r_i \leq r \leq r_t$ .

$$v_\theta(r) = \omega r + v_r(r) \tan \beta_b(r) \quad (2.8)$$

Note that  $\beta_b(r)$  is the blade sweep as a function of  $r$ , and it is typically negative. The mass flow rate can be determined by evaluating the flow at  $r_i$ .

$$\dot{m} = \rho v_r(r_i) A_{cs}(r_i) \quad (2.9)$$

Because  $\dot{m}$  is constant throughout the flow, the  $v_r(r)$  can be solved for all  $r$ .

$$v_r(r) = \frac{\dot{m}}{\rho A_{cs}(r)} \quad (2.10)$$

$v_r(r)$  decreases at an advective deceleration of  $1/r$  as it moves along the radial coordinate. This is because  $A_{cs}(r)$  is a linear function of  $r$ . It is useful to know what the relative velocity of the air over the rotor is;

$$v_{\theta, \text{rel}} = v_\theta - \omega r \quad (2.11)$$

The magnitudes of the absolute and relative velocities between  $r_i$  and  $r_t$  are the 2-norm of their respective velocities.

$$v = \sqrt{v_r^2 + v_\theta^2} \quad (2.12)$$

$$v_{\text{rel}} = \sqrt{v_r^2 + v_{\theta,\text{rel}}^2} \quad (2.13)$$

The air velocities and mass flow in the inlet are significant in determining the pressure drops due to friction. The assumption that the mass flow splits equally among the layers gives the mass flow through the inlet of the device at various heights gives:

$$\dot{m}_y(j) = \dot{m}(n_r - j) \quad (2.14)$$

Where  $j$  is an index, indicating which layer is being discussed. Equations (2.14) and (2.15) are defined from  $1 \leq j \leq n_r$ .  $j$  maps to  $\tilde{y}$  as

$$\tilde{y}(j) = j(h_c + h_s) + h_m \quad (2.15)$$

Rearranging (2.15) to solve for  $j$  and inserting into (2.14) gives

$$\dot{m}_y(\tilde{y}) = \dot{m} \left[ n_r - \frac{\tilde{y} - h_m}{(h_c + h_s)} \right] \quad (2.16)$$

The radially-averaged axial velocity in the core is then found by conservation of mass to be

$$v_y(\tilde{y}) = \frac{\dot{m}_y(\tilde{y})}{\rho A_i} \quad (2.17)$$

## 2.6 Pathlines

Since there is an azimuthal component to the velocity in the flow channel, the pathline of a fluid particle in the flow channel will not be purely radial, but will be curved along the direction of blade rotation. This has ramifications for pressure losses due to friction in the flow channel.

When  $\partial/\partial t = 0$ , the pathline is also the streamline. The streamlines are everywhere tangent to the velocity field. Using the natural coordinate system of this problem, polar coordinates:

$$\frac{r d\theta}{dr} = \frac{v_\theta}{v_r} \quad (2.18)$$

rearranging,

$$\int d\theta = \int \frac{v_\theta}{rv_r} dr \quad (2.19)$$

evaluating,

$$\theta(r) = \frac{\omega r}{2v_r} + \tan \beta_b(r) + C \quad (2.20)$$

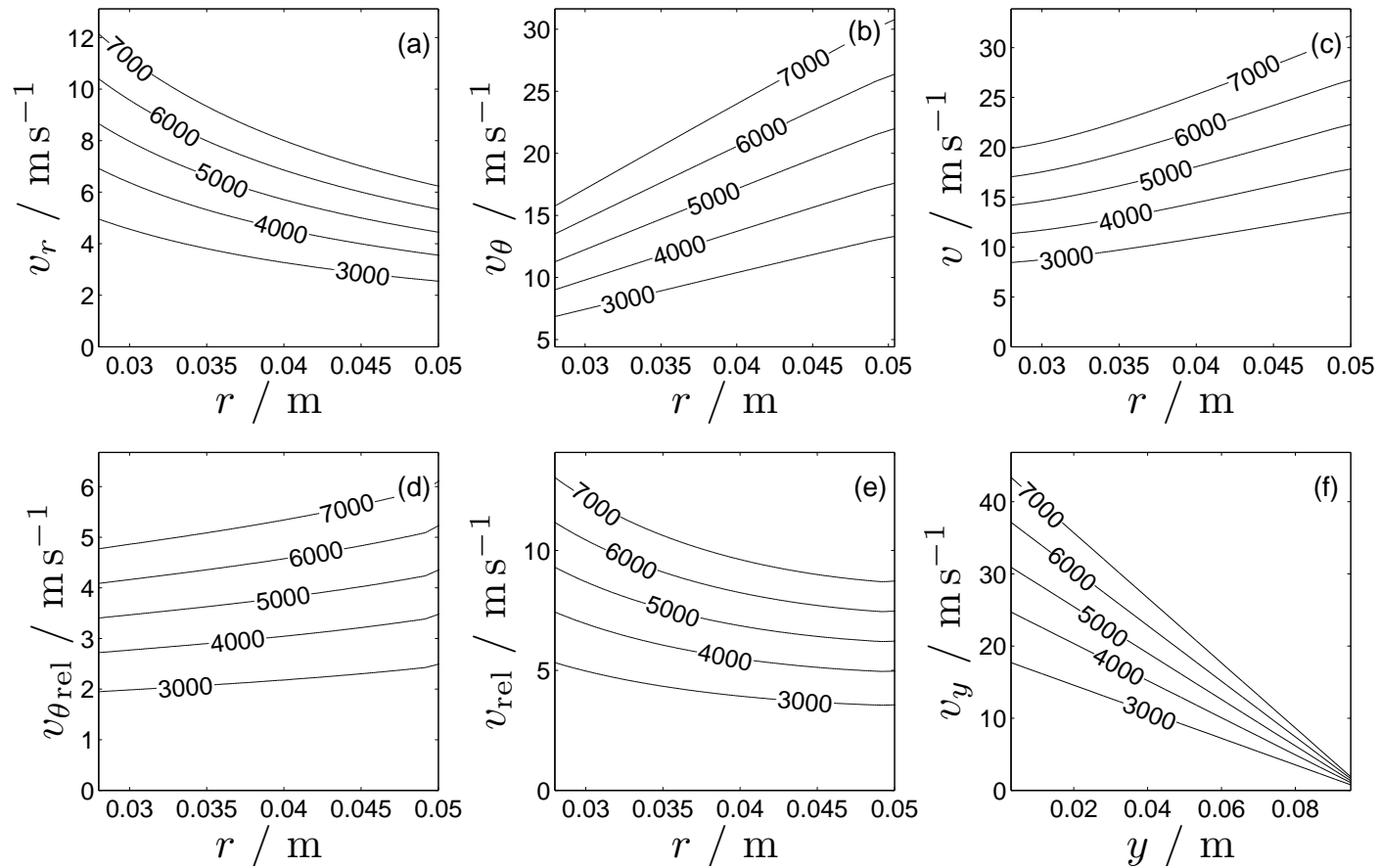


Figure 2.3: Plots of several air velocities. All velocities are the bulk velocities of the flow at the position marked on the abscissa. Velocities are plotted as level sets of angular speed as marked on the graph and have units of rpm. The abscissa of all plots is  $r$ , except the last which is  $y$ . **(a)** radial velocity of air in the flow channel,  $v_r$  advectively decelerates. **(b)** azimuthal velocity of air in the flow channel,  $v_\theta$  increases nearly linearly when the blade sweep is small. **(c)** magnitude of air velocity in the flow channel,  $v$  is the 2-norm of  $v_\theta$  and  $v_r$ . **(d)** Absolute value of relative azimuthal air velocity in the flow channel,  $v_{\theta_{\text{rel}}}$ . **(e)** magnitude of relative air velocity in flow channel,  $v_{\text{rel}}$  is the 2-norm of  $v_r$  and  $v_{\theta_{\text{rel}}}$ . **(f)** axial velocity of air in the inlet,  $v_y$ .

This is the equation for the angular position of a fluid particle given its radial position. The locus of points that satisfies this condition is the pathline.  $C$  is a constant of integration that indicates the initial direction of flow.

As a fluid particle moves through the flow channel, it follows the pathline experiencing frictional pressure losses along the path. The length of the path from the origin up to position  $r$  is referred to as  $\xi(r)$ . Fig. 2.2 shows the pathline in the lab reference frame as a blue line. The increment from  $\xi(r(i))$  to  $\xi(r(i+1))$  is  $\Delta\xi(r(i))$ . Using Pythagoras' theorem,

$$\Delta\xi(r) = \sqrt{(\Delta r)^2 + (r\Delta\theta(r))^2} \quad (2.21)$$

## 2.7 Air Properties

Air density, and all other air properties, are taken to be constant at this value for all temperatures and pressures, to maintain the linearity of the system. This is a good assumption because the heat transfer and air speeds are low enough to make the flow incompressible. The highest expected Mach number in the flow is 0.15 at the inlet of the heat sink. Other air properties that are used are: dynamic viscosity,  $\mu$  specific heat capacity at constant pressure,  $c_p$ , thermal conductivity,  $\kappa$ , and Prandtl number,  $Pr = c_p \mu / \kappa$ .

## 2.8 Dimensionless Numbers

In order to determine the friction factors and Nusselt numbers which will allow calculation of the pressure drop and heat transfer, respectively, several dimensionless numbers about the flow must be known. In this flow, these dimensionless numbers are calculated locally as a function of  $r$ , since the velocity is a function of  $r$ . The Reynolds number of the flow in the flow channel is

$$Re = \frac{\rho v D_h}{\mu} \quad (2.22)$$

This Reynolds number is defined for an internal flow, however this Reynolds number does not describe the rotor's rotation. The Reynolds number in the inlet passage is

$$Re_i = \frac{2\rho v_y r_i}{\mu} \quad (2.23)$$

Plots of these Reynolds numbers are shown in Fig. 2.4.

Nusselt numbers for the flow can now be determined. The flow is a flat duct flow where the two wall temperatures are uniform and equal. Note that a flat duct flow is a rectangular cross-section duct with a cross-sectional aspect ratio of infinity. The following correlations are local to the  $r$  position in the channel, but averaged across the channel width; this will allow the local heat transfer coefficient to be calculated and later the heat flux can be

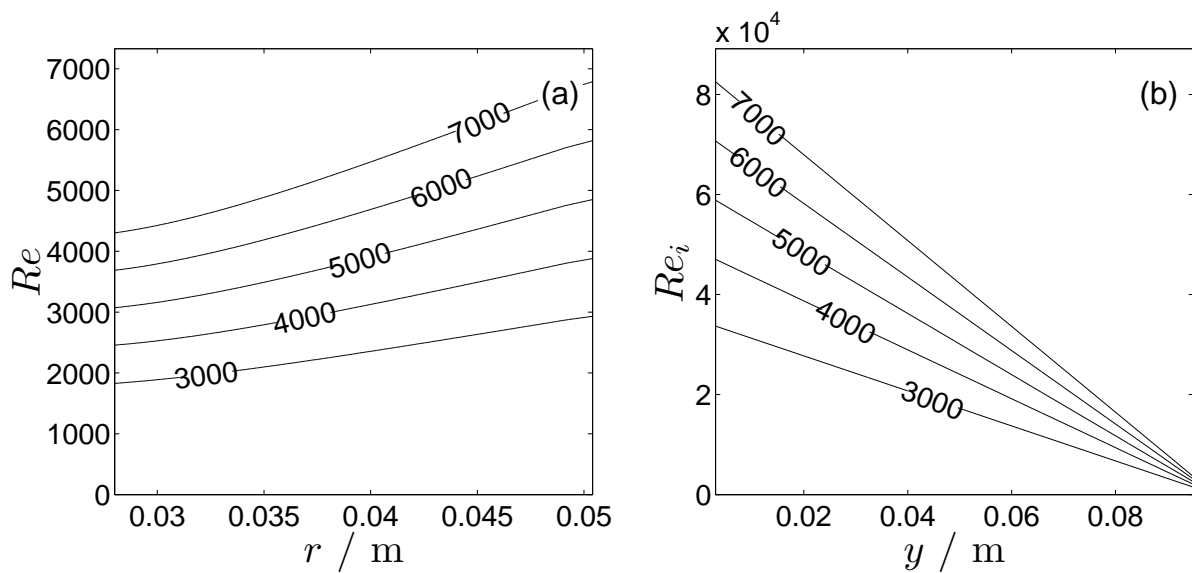


Figure 2.4: Plots of Reynolds numbers in the inlet passage and flow channel. Plots are shown as level sets of angular speed in rpm. **(a)** Reynolds number of air in the flow channel,  $Re$ . Plot is for the region in the flow channel and is a function of the radial coordinate,  $r$ . **(b)** Reynolds number of air in the inlet passage,  $Re_i$ . Plot is for the region in the flow channel and is a function of the axial coordinate,  $y$ .

integrated over all of the local heat fluxes. The local Nusselt correlation in the developing region for laminar flow with constant temperature walls is [7]

$$Nu_{\text{lam,dev}} = 7.55 + \frac{0.024r^{*-1.14} \left( 0.0179Pr^{0.17}r^{*-0.64} - 0.14 \right)}{\left( 1 + .0358Pr^{0.17}r^{*-0.64} \right)^2} \quad (2.24)$$

Where  $r^* = r/D_h Pr Re$ , is the dimensionless radial coordinate for the thermal entrance region. The Nusselt number for laminar, fully developed flow in a flat duct with both wall temperatures uniform and equal is [8]

$$Nu_{\text{lam}} = 7.541 \quad (2.25)$$

There are no Nusselt correlations for simultaneously developing, turbulent, flat duct flows for fluids with  $Pr = 0.7$  [9]. However, with the hydraulic diameter assumption a correlation based on circular cross section flows is available [10]. This correlation is for a 90° elbow turn entrance, similar to the flow turn from the inlet passage to the flow channel; this correlation was created using constant heat flux boundary conditions, but behaves similarly to constant temperature conditions, especially at high  $Re$ . Equation (2.26) is a local Nusselt correlation and was obtained by differentiating the mean Nusselt correlation given by the authors in reference [10].

$$Nu_{\text{turb,dev}} = Nu_{\infty} \left( 1 + 0.7779(r/D_h)^{-0.614} \right) \quad (2.26)$$

Where  $Nu_{\infty}$  is the Nusselt number for turbulent, developed flow with a circular cross section,

$$Nu_{\infty} = 0.0214(Re^{0.8} - 100) Pr^{0.4} \quad (2.27)$$

The proper Nusselt correlations for different  $r$  are assembled together into  $Nu(r)$  and the heat transfer coefficient can be determined

$$h(r) = \frac{\kappa Nu(r)}{D_h} \quad (2.28)$$

The heat transfer coefficient as a function of  $r$  is plotted in Fig. 2.5.

## 2.9 Power and Pressure

Now that the Reynolds numbers have been determined, an evaluation of the pressure rise and drop in the heat sink can be done. It is necessary to compute these pressure drops to see at what flow rate they balance with the pressure rise induced by the fan. This flow rate will be the steady state flow rate of the heat sink at that fan speed.

The pressure rise from the rotors,  $\Delta p_{\text{rise}}$ , can be derived from the Euler turbine equation, which relates the pumping power produced by a turbine, or as in this case, required to turn an impeller:

$$\dot{W} = \omega \dot{m} r_t v_{\theta}(r_t) \quad (2.29)$$

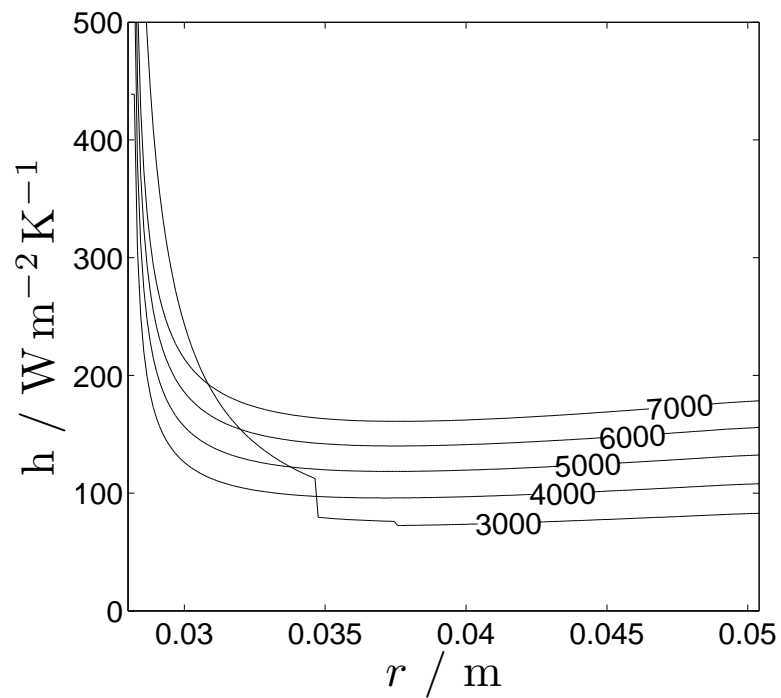


Figure 2.5: Plot of local heat transfer coefficient,  $h$ , over radial coordinate,  $r$ . Level sets of angular speed, in rpm, are plotted.  $h$  is higher at low  $r$  due to flow development. The 3000 rpm curve displays a transition to turbulence at  $r = 0.035$  m. The slight increase in  $h$  at higher  $r$  is due to increasing  $Re$  at the periphery.



Where  $v_\theta(r_t)$  is the mass-weighted average of the azimuthal velocity at the radius of the blade tips. The Euler turbine equation accounts for the change in angular momentum from the inlet to the outlet of a turbomachine. Thus the Euler turbine equation, in general subtracts has terms accounting for the inlet and the outlet angular momentum. In this case, preswirl is assumed to be zero and there is no angular momentum at the inlet.

Any power performing mechanical work can be written as the product of the time derivative of the mechanical thermodynamic conjugate pairs, pressure and volumetric flow rate:

$$\dot{W} = \Delta p_{\text{rise}} \dot{V} = \Delta p_{\text{rise}} \frac{\dot{m}}{\rho} \quad (2.30)$$

Rearranging

$$\Delta p_{\text{rise}} = \dot{W} \frac{\rho}{\dot{m}} \quad (2.31)$$

Thus

$$\Delta p_{\text{rise}} = \rho \omega r_t v_\theta(r_t) \quad (2.32)$$

Now the pressure drop due in the heat sink due to friction and minor losses,  $\Delta p_{\text{drop}}$ , is to be determined. First, the dynamic pressure in the inlet and in the flow channel are, respectively

$$q_i(\tilde{y}) = \frac{1}{2} \rho v_y(\tilde{y})^2 \quad (2.33)$$

$$q_r(r) = \frac{1}{2} \rho v_{\text{rel}}(r)^2 \quad (2.34)$$

These dynamic pressures are coupled with friction factors to determine the pressure drop in the system. The Darcy friction factors,  $f_i$  and  $f_r$  indicate the friction losses in the inlet passage and flow channels [11].

$$f_i(r) = \begin{cases} 64 Re_i^{-1} & \text{for } Re_i < 2100 \\ 0.0216 + 9.2 \times 10^{-8} Re_i^{1.5} & \text{for } 2100 < Re_i < 4000 \\ 0.00512 + 0.4572 Re_i^{-0.311} & \text{for } 4000 < Re_i \end{cases} \quad (2.35)$$

$$f_r(r) = \frac{4}{Re} \left( \frac{3.44}{(r^+)^{1/2}} + \frac{24 + 0.1685(r^+)^{-1} - 3.44(r^+)^{-1/2}}{1 + 0.000029(r^+)^{-2}} \right) \text{ for } Re < 2100 \quad (2.36)$$

$$f_r(r) = 0.0752 \left( 5.439 Re^{-0.08761} - 1.427 \right) \left( \frac{0.3626r/D_h + 0.8993}{r/D_h + 0.7321} \right) \text{ for } 2100 < Re \quad (2.37)$$

The friction factor in the inlet passage, (2.35), is based on friction factor correlations for flow in a circular cross section. Equation (2.36), describing the friction factor in the flow channel, is for laminar, developing flow in a flat duct geometry, where  $r^+ = r/D_h Re$ . Equation (2.37) is like (2.36) except that it is for turbulent flow. Equation (2.37) was created based on

tabular data in Ref. [11] for  $10^4 < Re < 10^5$  and extrapolated to the transitional flow regime, where (2.37) predicts higher friction factors, as would be expected. The length of the flow path in the flow channel is only 3 to 10 hydraulic diameters (depending on the height of the flow channel), which is less than the hydraulic entrance length for laminar or turbulent flows.

The friction factors are then used to find the pressure drop in the inlet passage and in the flow channel by adding the inlet minor loss and summing the frictional losses over the flow path.

$$\Delta p_{\text{drop},i}(j) = (1 + K_i)q_i(j=0) + \sum_{j=0}^j \frac{f_i(r)(h_c + h_s)}{D_{h_i}} q_i(\tilde{y}) \quad (2.38)$$

$$\Delta p_{\text{drop},r} = K_{\text{turn}}q_r(r=r_i) + \sum_{r=r_i}^{r_t} \left( \frac{f_r(r)\Delta\xi(r)}{D_h} q_r(r) \right) \quad (2.39)$$

$K_i$  and  $K_{\text{turn}}$  are the inlet and turning loss coefficients, respectively.  $K_i = 0.5$  and  $K_{\text{turn}} = 1.1$ [12]. Note that  $\Delta p_{\text{drop},i}(j)$  is a function of which layer is being discussed. Since the flow rate is assumed to split evenly among the channels, a mean value of  $\Delta p_{\text{drop},i}$  is used. The constant, 1, in (2.38) represents the pressure drop induced by the acceleration of the fluid from rest to the inlet velocity. In practice,  $\Delta p_{\text{drop},r}$  and the inlet pressure losses dominate over the component of pressure loss that varies as a function of layer, thereby justifying the assumption that flow rate is equal through all layers.  $\Delta p_{\text{drop},i}$  is set equal to the pressure drop through a typical layer. The total pressure drop is

$$\Delta p_{\text{drop}} = \Delta p_{\text{drop},i} + \Delta p_{\text{drop},r} \quad (2.40)$$

and the pressure difference is

$$\Delta p_{\text{dif}} = \Delta p_{\text{rise}} - \Delta p_{\text{drop}} \quad (2.41)$$

The value attained for  $\Delta p_{\text{dif}}$  is then used in the aforementioned line search algorithm to define a better  $v_r$  and the solution is iterated until it converges.

## 2.10 Air and Stator Temperature

Now we will see how the heat transfer coefficient affects the bulk temperature of the air as it moves through the flow channel,  $T(r)$ , and the temperature of the stator,  $T_s$ . As air moves downwards through the inlet of the heat sink it does not interact with an extended surface over which heat transfer can take place, thus the temperature in the inlet is assumed to be ambient temperature. As air moves outward through the flow channel, it passes over the stators and gains heat, causing its temperature to rise. By the conservation of energy leaving the stators and entering the air as sensible heat, the air temperature at the exit can be determined.

$$T(r_t) = \frac{\dot{Q}}{\dot{m}c_p} + T(r_i) \quad (2.42)$$

The air temperature as a function of path coordinate,  $T(r)$ , is a problem that is very much like the temperature of fluid flow in a pipe of constant temperature. Following the solution technique of Naterer [13],  $T(r)$  can be derived. The conservation of energy through an annular control volume at  $r$  that is  $\Delta r$  thick is:

$$\dot{m}c_p(T_s - T(r + \Delta r)) - \dot{m}c_p(T_s - T(r)) = n_s \mathcal{P}(r)h(r)\Delta r(T_s - T(r)) \quad (2.43)$$

where  $\mathcal{P}(r)$  is the wetted perimeter of the cross section at  $r$  over which heat transfers:  $\mathcal{P}(r) = 4\pi r$  (this includes both top and bottom surfaces of the stator). Note the  $n_s$  term indicating that heat transfers through every stator. Taking the limit as  $\Delta r \rightarrow 0$  and rearranging,

$$\frac{d(\Delta T)}{\Delta T} = -\frac{n_s \mathcal{P}(r)h(r)}{\dot{m}c_p} dr \quad (2.44)$$

Where  $\Delta T = T_s - T(r)$ . Integrating both sides and evaluating from  $r_i$  to  $r$ , we have

$$\log\left(\frac{T_s - T(r)}{T_s - T(r_i)}\right) = \frac{-2\pi n_s}{\dot{m}c_p} \int_{r_i}^r h(r)r dr \quad (2.45)$$

Define the right hand side to be  $C(r)$ , and  $C(r_t) = C_{r_t}$ . Exponentiating and rearranging to solve  $T(r)$ :

$$T(r) = T_s - (T_s - T(r_i)) e^C \quad (2.46)$$

$T_s$  is still unknown; evaluating at  $r_t$ , and solving for  $T_s$ ,

$$T_s = \frac{T(r_t) - T(r_i) e^{C_{r_t}}}{1 - e^{C_{r_t}}} \quad (2.47)$$

When the flow channel is short and the mass flow is high,  $T(r_t)$  is significantly less than  $T_s$ .  $T(r)$  is plotted in Fig. 2.6. For scaling reasons,  $T_s$  is not shown in Fig. 2.6. Note that because  $\partial/\partial\theta = 0$ , The differential element through which flow is evaluated is only an annular ring, rather than a discrete element as a function of  $\theta$ . Thus, considerations of the pathline are irrelevant to the heat transfer to the air.

## 2.11 Thermal Resistance

The thermal resistance of the entire system is

$$R_{\text{tot}} = \frac{T_e - T_{\text{amb}}}{\dot{Q}} \quad (2.48)$$

Where  $T_e$  is the temperature of the bottom of the evaporator, where it is affixed to the heat source, and  $T_{\text{amb}}$  is the ambient temperature, which is also  $T(r_i)$ .

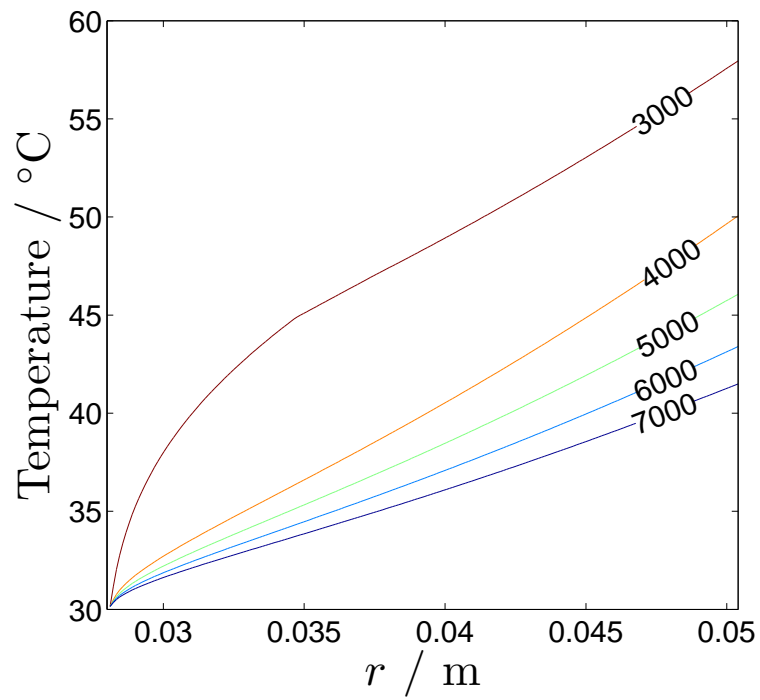


Figure 2.6: Plot of air temperature,  $T$  over radial coordinate,  $r$ . Heat flux is held constant and  $T_s$  varies. Level sets of angular speed are marked with units of rpm.

Moving along the path of travel of the heat,  $R_{\text{tot}}$  may be broken into the following components:  $R_{\text{evap, conduct}}$ ,  $R_{\text{heat pipe}}$ ,  $R_{\text{stat, conduct}}$ , and  $R$ .  $R_{\text{evap, conduct}}$  is the thermal resistance through the solid wall of the evaporator, into the evaporator proper.

$$R_{\text{evap, conduct}} = \frac{t_{\text{evap wall}}}{\kappa_{\text{evap}} A_{\text{evap}}} \quad (2.49)$$

Where  $t_{\text{evap wall}}$ ,  $\kappa_{\text{evap}}$ , and  $A_{\text{evap}}$  are the thickness, thermal conductivity, and area of the evaporator wall, respectively.

$R_{\text{heat pipe}}$  is dependent on the interaction of the two-phase fluid with the wick structure inside the heat pipe component of the design and is very important to the design of the heat sink but is not handled here.  $R_{\text{stat, conduct}}$  is the resistance through the solid wall of the stator.

$$R_{\text{stat, conduct}} = \frac{t_{\text{stat wall}}}{\kappa_{\text{stat}} A_{\text{stat}}} \quad (2.50)$$

The variables of (2.50) are like those of (2.49).  $R$  is the thermal resistance due to the interaction between the stator surface and the air

$$R = \frac{T_s - T_{\text{amb}}}{\dot{Q}} \quad (2.51)$$

Finally, the total resistance is the sum of the components and must be less than the design criteria.

$$R_{\text{tot}} = R_{\text{evap, conduct}} + R_{\text{heat pipe}} + R_{\text{stat, conduct}} + R \quad (2.52)$$

The desired operating speed will be that at which the maximum allowed power is used. Fig. 2.7 plots air convection resistance, pumping power, and mass flow rate of air against angular speed. There is a transition to turbulence around 3500 rpm that causes a jog in the behavior of the thermal resistance. As can be seen in the figure, the predicted performance is well below the requirements set for the project. Later results show improved performance over this estimate. This discrepancy is due to the use of duct flow friction factor and Nusselt number correlations in this model, whereas the actual application has a rotating rotor within the channel, a geometry for which there are no previously available correlations.

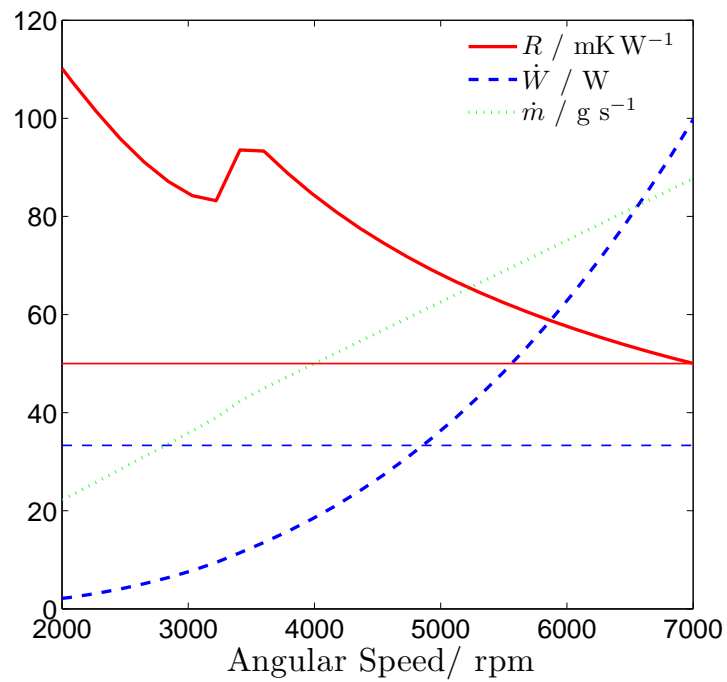


Figure 2.7: Plot of various parameters germane to heat sink performance, as a function of angular speed,  $f$ . Units listed in the legend. The minimum allowable total resistance is indicated by a horizontal solid red line and the maximum allowable pumping power is indicated by a horizontal dashed blue line.

## 2.12 Single Layer Model

The performance of a heat sink design with only one rotor and one stator was also predicted with this model to allow comparisons with computational and experimental data discussed in later chapters. This model is like the multilayer model shown above but with the pumping power of only a single rotor and without a pressure drop in the inlet passage of the heat sink. The results of this model are plotted in Fig. 2.8 where thermal convection resistance,  $R$ , is plotted as a function of pumping power,  $W$ . As pumping power increases, thermal resistance decreases. Since it is desirable to reduce both the thermal resistance and the pumping power, this is a case of multivariate optimization in which the optimal value for two variables is sought but there is some tradeoff between the two. In the field of multivariate optimization, the concept of Pareto optimality is central. A Pareto optimal solution is a solution in which at least one of the variables to be optimized is optimum when all other variables to be optimized are at a fixed value. In the case of a heat sink, a Pareto optimal solution is one in which, for a given pumping power, the thermal resistance is lower than for any other design. This solution is said to ‘dominate’ other solutions. The set of solutions that are Pareto optimal are referred to as the Pareto frontier. In this work, the Pareto frontier for a given set of data is generated by a single heat sink design, with different points along the curve representing different angular speeds of the rotor. Thus, the pumping power is parametrized by the angular speed of the fan so that increased fan speed increases the pumping power (and decreases the convection thermal resistance). In Fig. 2.8, the Pareto optimal design is the plot with white triangles.

This concept of Pareto optimality has been used previously in the heat sink literature, as in [14][15][16]. It is possible and desirable to create plots of convection thermal resistance versus pumping power to characterize any forced convection heat sink and compare it with any other forced convection heat sink. Most commonly in the literature the pumping power is plotted on the abscissa and the convection thermal resistance on the ordinate. This convention rightly implies that pumping power is the independent variable while thermal resistance is the dependent variable; this convention is recommended and followed here.

In the single layer model, the optimal performance was achieved at  $r_i = 20$  mm, however in the multilayer model above, this optimum widened out to 28 mm to accommodate the higher mass flow rate through the multilayer design.

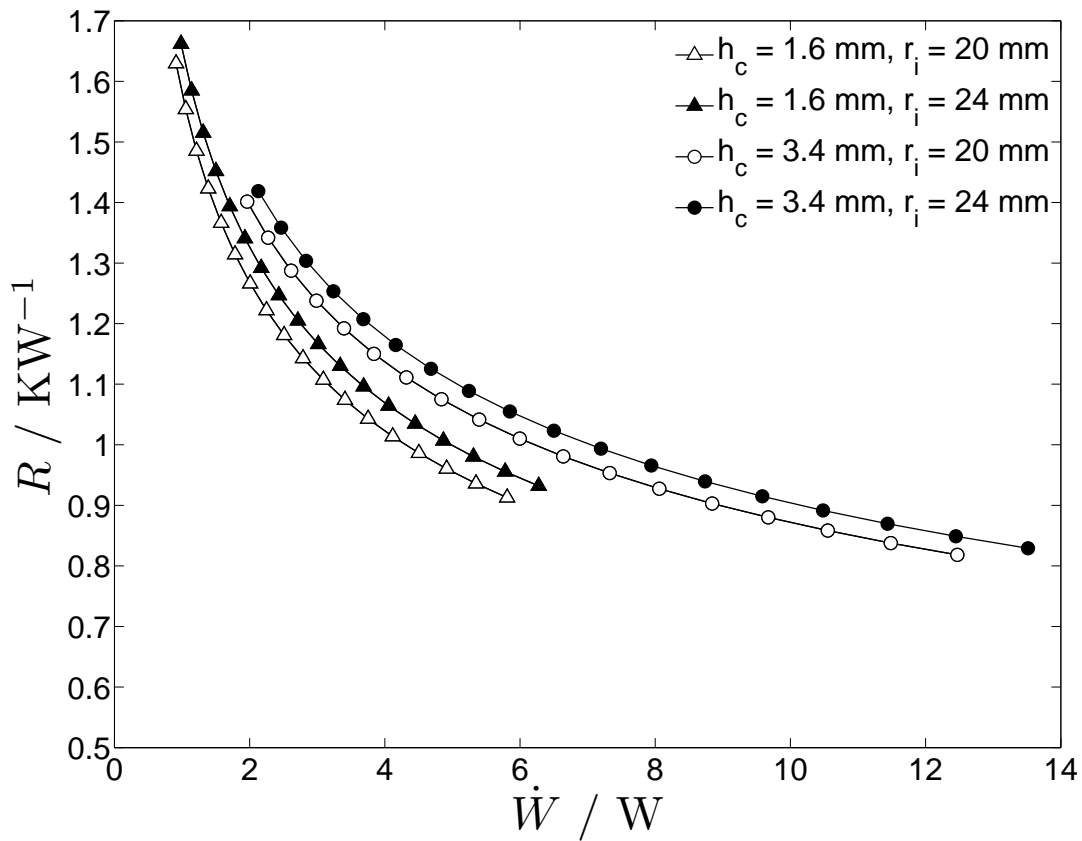


Figure 2.8: Plot of predicted values of  $R$  versus  $\dot{W}$  for a single layer heat sink. Curves are shown for several combinations of  $h_c$  and  $r_i$ , as described in the legend. Curves are plotted from 3000 to 7000 rpm.



## 2.13 Buoyancy Effects

Since this flow has a body force due to the centrifugal acceleration it experiences, and there is a temperature gradient along that direction, it is prudent to calculate the ratio of buoyant forces to inertial forces. This is the Richardson number, which is the Grashof number divided by the square of the Reynolds number.

$$Ri = \frac{\omega^2 r \beta [T(r_t) - T(r)] (r_t - r_i)}{v(r)^2} \quad (2.53)$$

Where  $\beta$  is the volumetric thermal expansion coefficient. Note that this ratio is a function of the radius,  $r$ , of the fluid particle in discussion. (2.53) is found to be no more than 0.002 for representative designs, meaning that buoyancy effects due to centrifugal acceleration are negligible.

## 2.14 Rotors as Fluid Bearings

Due to the small clearances between rotor and stator, the possibility of shaping the blades to be hydrodynamic fluid bearings was considered. This design was explored because it could possibly reduce the difficulty of aligning the rotors axially between the stators. In such a design the rotors would be radially confined to rotate with the shaft but be axially free to float in the center of the flow channel; the hydrodynamic forces would center the rotor within the channel. This design would eliminate the need for the complicated assembly processes that would otherwise be required to achieve the necessary clearances between the rotors and stators. Fig. 2.9 shows a diagram of the wedge shaped cross-section of rotors that act as their own fluid bearing.

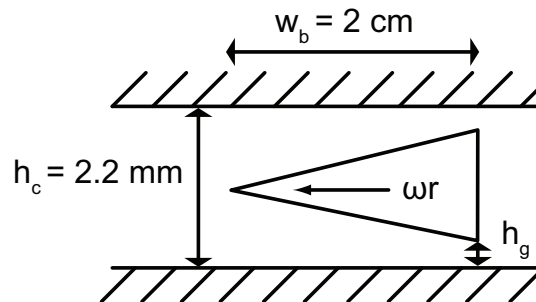


Figure 2.9: Diagram of design of rotors to act as their own fluid bearing. Specified dimensions are the same as those used in Fig. 2.10.

A Couette flow in which the gap between the walls is convergent in the flow direction generates a pressure field which can support a load in the transverse direction. This pressure field is approximately parabolically distributed in the flow direction. The maximum gage pressure is [17]

$$p|_{max}(r) = \frac{3\mu\omega r w_b (h_c - 2h_g)}{h_c h_g (h_c + 2h_g)} \quad (2.54)$$

Where the rotor is wedge shaped, pointed end towards the flow;  $h_c$  is the distance between stators, but  $h_g$  is the shortest distance from the rotor to the stator, i.e., the distance from the trailing surface of the rotor to the stator. The lift force on the rotor is the integral of the pressure field over the rotor surface.

$$F_L = \iint p(r, w) n_b dr dw \approx \int_0^{r_t} \frac{2}{3} p|_{max} n_b w_b dr \approx \frac{\mu\omega r_t^2 n_b w_b^2 (h_c - 2h_g)}{h_c h_g (h_c + 2h_g)} \quad (2.55)$$

The average pressure in the width-wise direction is approximately two thirds of  $p|_{max}$ . The weight of the rotor is

$$F_W = \frac{1}{2} n_b \rho_b g w_b r_t (h_c - 2h_g) \quad (2.56)$$

Where  $\rho_b$  is the density of the rotor material. The factor of 1/2 accounts for the triangular cross-section of the blade, where  $h_c - 2h_g = h_b$  is the thickness of the blade at the trailing edge. The ratio of lift to weight should be significantly greater than one in order for the rotor to lift off the surface of the stators.

$$\frac{F_L}{F_W} \approx \frac{2\mu\omega r_t w_b}{\rho_b g h_c h_g (h_c + 2h_g)} \quad (2.57)$$

(2.57) is plotted in Fig. 2.10 for  $h_c = 2.2$  mm,  $w_b = 2$  cm, and a rotor made of high density polyethylene, for a variety of angular speeds and a variety of  $h_g$ . As  $f$  increases, the lift ratio increases. Lift ratio increases dramatically with decreased  $h_g$ . The lift ratio should be high enough that the rotor is hydrodynamically trapped between the stators above and below it. Unfortunately, however,  $h_g$  must be on the order of 0.15 mm or less in order to achieve sufficient lift at reasonable speeds, because of the very low viscosity of air. Small  $h_g$  would specify a small difference between  $h_b$  and  $h_c$ . The manufacturing tolerances required to implement this design make it more difficult than a more traditional approach in which the rotor is axially fixed during construction. Thus this design was not pursued further.

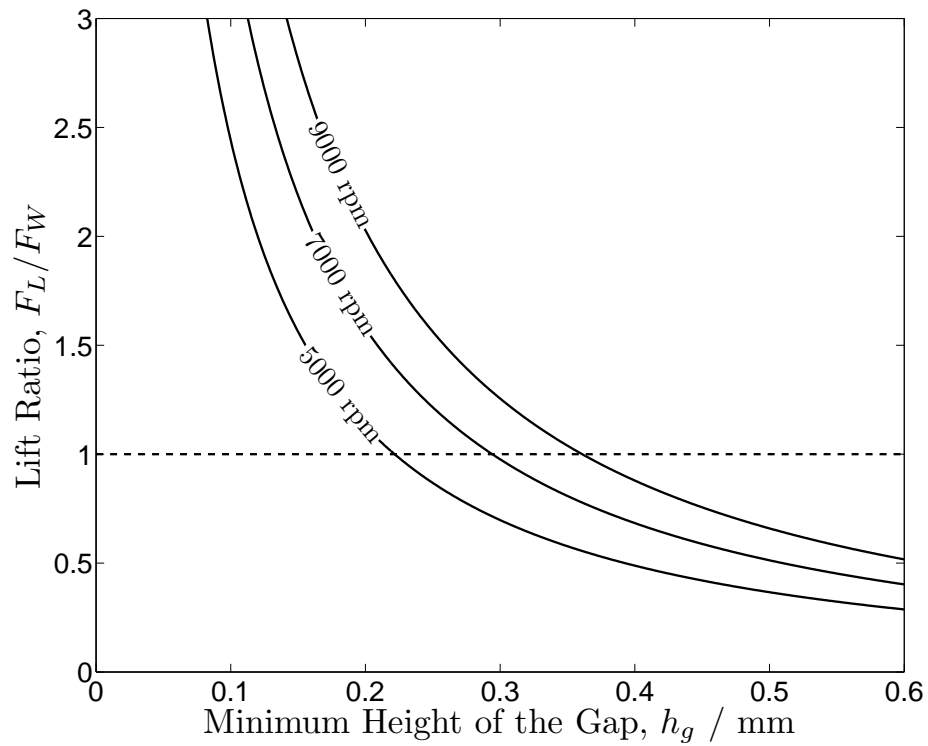


Figure 2.10: Lift ratio as a function of  $h_g$  for several angular speeds.  $h_c = 2.2$  mm,  $w_b = 2$  cm, rotor is made of high density polyethylene. Minimum feasible lift ratio of one is plotted as a dashed line.

---

## 2.15 Conclusions

This chapter has shown some of the physics of how air flow is induced through the device and how heat is transferred into the air. Air is pumped through the heat sink via a radial fan that spins the air azimuthally and thereby subjects the air to a centrifugal acceleration which blows the air out of the heat sink. This develops a low pressure zone inside of the heat sink which draws fresh air into the heat sink. In this way, the fan creates a pressure rise in the air. The air flow through the heat sink increases until the pressure losses induced by frictional effects inside the heat sink balance the pressure rise due to the fan and the flow rate reaches its steady state for that given fan speed. This flow rate then sets the air velocities flowing past the heated surfaces of the heat sink and induces heat transfer into the air.

In this chapter, this flow was modeled by a correlation based model that depends on correlations developed for flow in ducts. This flow however is much more complicated than duct flow, having velocities and Reynolds numbers that change as a function of location in the heat sink, and with significant radial and azimuthal velocity components. Additionally, there are complicated flow turns and rotating blades that cannot be modeled with previously available correlations. Due to these discrepancies between the model and the real flow, this model predicts poorer performance than the requirements for this project specify, as well as poorer performance than the experimental results show. Improved performance is created by the higher heat transfer coefficients induced by the passing blades.

# Chapter 3

## Nondimensionalization

### 3.1 Introduction

In this chapter, a nondimensionalization is carried out to allow analysis of similar heat sinks on a variety of scales.

The approach of Ch. 2 was to determine as much as possible with information available from the literature. This chapter will focus on determining what information should be known in order to thoroughly characterize the single-layer heat sink experiment described in Ch. 5 and make predictions about the performance of similar heat sinks.

A nondimensional study of this single layer heat sink gives nine parameters. Five of these parameters are classified as independent, because they can be independently varied. The other four dependent parameters are functions of the independent parameters. The nondimensional dependent parameters can be used in concert with other dimensioned variables to predict the pumping power,  $\dot{W}$ , and the air convection thermal resistance,  $R$ . In Sec. 5.6, correlations are presented for the dependent parameters as a function of the independent parameters in certain ranges.

### 3.2 Independent Parameters

The radius of the tip of the rotor,  $r_t$ , is set to be tangent to the boundary of the device to allow the fan to cover the largest possible area of the heat sink. The following length dimensions are shown in Fig. 3.1.  $r_t$  is used as the generating length dimension for nondimensionalization. The first dependent parameter,  $B$ , describes the aspect ratio of the blade.

$$B = \frac{h_b}{r_t} \quad (3.1)$$

$G$  describes the aspect ratio of the flow channel.

$$G = \frac{h_c}{r_t} \quad (3.2)$$

$\mathcal{I}$  is defined as the ratio of the inlet radius to the radius of the blade.

$$\mathcal{I} = \frac{r_i}{r_t} \quad (3.3)$$

In the experimental setup discussed in Sec. 5.1,  $\mathcal{I}$  cannot be easily varied so a single value is selected and its effect on the dependent parameters is not explored further here.

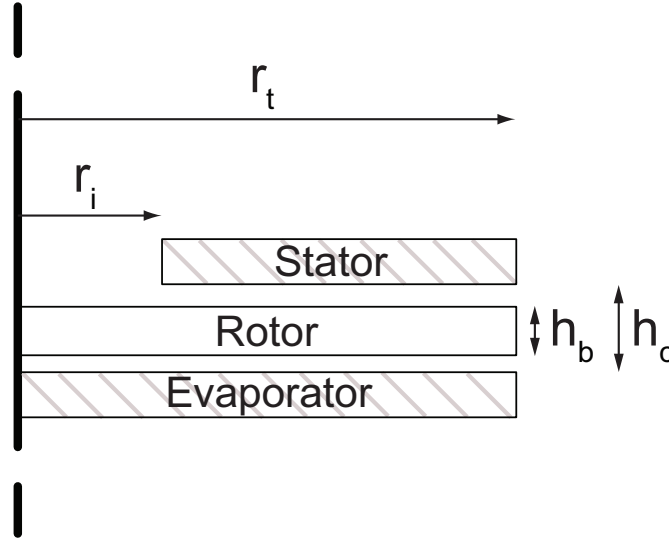


Figure 3.1: Cross-sectional diagram of the flow volume with length dimensions  $r_t$ ,  $r_i$ ,  $h_b$ , and  $h_c$  marked.

The Prandtl number of the convecting fluid (always air in this analysis),  $Pr$ , and the rotational Reynolds number of the rotor are also independent parameters. Rotational Reynolds number is most commonly defined as [2][3]:

$$Re_\omega = \frac{\rho\omega r_t^2}{\mu} \quad (3.4)$$

### 3.3 Dependent Parameters

The dependent parameters begin with the flow coefficient,  $C_f$ , a turbomachinery parameter [18] giving a linearly scaled ratio of  $\dot{m}$  through the system to the mass of the air in the volume swept out by the rotor per unit time.

$$C_f = \frac{\dot{m}}{\rho\omega r_t^3} \quad (3.5)$$

The slip factor,  $\sigma$ , is another turbomachinery parameter that gives the ratio of the azimuthal velocity of the air at the blade tip to the velocity of the blade tip itself, describing how well the flow is driven by the blade. A slip factor of one implies the fluid is perfectly driven by the rotor.

$$\sigma = \frac{\dot{W}}{\dot{m}\omega^2 r_t^2} \quad (3.6)$$

This can be seen by substituting the Euler turbine equation with no preswirl (2.15) into (3.6). Note that in the limit of perfectly driven flow, the numerator of (3.6) equals the

denominator. Slip factor correlations in turbomachinery are functions of number of blades on the rotor, and blade angle at the tip [19].

The next parameter comes from heat exchanger analysis. The exchanger effectiveness,  $\varepsilon$ , is the ratio of the actual energy exchanged to the maximum amount of energy that could be exchanged. Herein  $\varepsilon$  is defined for only the air flow, although it could be defined between the heat pipe two-phase fluid and the air.

$$\varepsilon = \frac{\dot{Q}}{\dot{m}c_p(T_s - T_{\text{amb}})} = \frac{\bar{T}_o - T_{\text{amb}}}{T_s - T_{\text{amb}}} \quad (3.7)$$

Where  $c_p$  is the specific heat of air at constant pressure and  $T_s$  and  $T_{\text{amb}}$  are the temperature of the stator wall and ambient, respectively. Because no phase change occurs in the air flow,  $\varepsilon$  is merely the ratio of the temperature differences between the outlet,  $\bar{T}_o$ , and the ambient and the stator surface and the ambient. The final parameter is the coefficient of performance, COP, which gives the ratio of total heat transferred ( $\dot{Q}$ ) to the work required to drive the fan ( $\dot{W}$ ).

$$\text{COP} = \frac{\dot{Q}}{\dot{W}} \quad (3.8)$$

Though COP is commonly used to quantify the performance of heat pumps where heat is moved against a thermal gradient by doing work, COP is less useful as an indicator of performance in heat sinks where heat is helped along a favorable temperature gradient by doing work, because work is not strictly required to cause the heat transfer in question. For example, heat sinks without fans have no work input and would therefore have a COP of infinity.  $\dot{W}$  itself is a better indicator of the performance of a given heat sink, and will be used herein.

### 3.4 Performance Parameters

$\dot{W}$  and  $R$  are referred to as performance parameters because they quantify the performance of the heat sink. The definitions of  $\dot{W}$  and  $R$  can be rearranged in terms of nondimensional parameters and known quantities to predict heat sink performance.

Substituting (3.5) into (3.6) and rearranging,

$$\dot{W} = \sigma C_f \rho \omega^3 r_t^5 \quad (3.9)$$

The thermal resistance of air convection, from ambient to the surface temperature,  $R$ , is the largest part of the thermal resistance in the heat sink because of the low thermal conductivity and heat capacity of air relative to the two-phase fluid in the heat pipe.

$$R = \frac{T_s - T_{\text{amb}}}{\dot{Q}} \quad (3.10)$$

This is a restatement of (2.51). Rearranging (3.7) and inserting,

$$R = (\varepsilon \dot{m} c_p)^{-1} \quad (3.11)$$

---

and rearranging (3.5) and (3.4) to solve for  $\dot{m}$  and  $\omega$ , respectively and inserting into (3.11),

$$R = (\varepsilon C_f Re_\omega Pr \kappa r_t)^{-1} \quad (3.12)$$

Note that the last two variables in parenthesis ( $\kappa$  and  $r_t$ ) on the right hand side of (3.12) are dimensioned, together having units of thermal conductance, their inverse being a thermal resistance.

Equations (3.9) and (3.12) are general to any fan-driven, forced convection heat sink, with any convecting fluid (typically air). These equations may be used to predict the performance given  $r_t$ ,  $\omega$ , the nondimensional independent parameters, the properties of the convecting fluid, and provided that  $C_f$ ,  $\sigma$ , and  $\varepsilon$  are known for the particular set of independent parameters to be used. Correlations of  $C_f$ ,  $\sigma$ , and  $\varepsilon$  are provided in Sec. 5.5 for heat sinks of the type described herein, across a range of independent parameters.



# Chapter 4

## Computational Model

### 4.1 Model Description

Computational fluid dynamics (CFD) models using GAMBIT and ANSYS Fluent were created to achieve higher fidelity over the correlation based model, by modeling the effect of rotor blades. This model was created only for a single layer heat sink to maintain reasonable computational costs; the mesh of a representative model is shown in Fig. 4.1. The computational model is a 3-dimensional, time-averaged flow, in a rotating reference frame with fixed walls, solved via pressure based Navier–Stokes with a Spalart–Allmaras turbulence model, with the energy equation. The rotational symmetry of the flow means that only one blade must be modeled. The corners of the heat sink are not modeled for simplicity. Neglecting the corners reduces the heat transfer area but also reduces the wall area, thereby reducing pressure drop due to shear stress in the fluid at the wall. Neglecting this slight pressure drop causes the angular velocity to increase slightly, increasing the heat transfer and making up for the lost surface area in the corners. Additionally, in the complete heat sink there are pipes in the four corners to convey the two-phase heat pipe fluid, which also cannot be modeled in the CFD model. These pipes will impede the actual flow somewhat, causing a fluidic resistance. The necessity of neglecting these pipes will have an effect that will cause the CFD model to be overly optimistic.

The model volume has pressure inlet and pressure outlet boundary conditions, the flow being driven by the rotation of the blades. This means that the velocity at the inlet and outlet of the flow is not specified, rather it is induced by the rotating blades. Furthermore, there is no location in the flow where a fluid velocity is specified, the only specified velocity is the blade rotation rate. The pressure rise induced by the rotating blades induces flow in the system. Calming lengths at the inlet and exit with no-shear wall conditions are added, effectively enforcing a jet inflow and jet outflow. These volumes improve the solution by separating regions where significant pressure variations occur from the fluid inlet and outlet boundaries where constant pressure is enforced. The true walls of the heat sink (stators) and the rotor are modeled as smooth walls with a no-slip condition and the stator walls are set to an isothermal boundary condition. In the actual heat sink the isothermality of the stator walls is set by the phase change of the fluid inside the stator. The grid is a structured mesh of hexahedral cells, with a boundary layer mesh to improve solution accuracy near solid–fluid boundaries. Typical models contain 500,000 to 1,000,000 cells. A grid study found that an order of magnitude more cells results in only a 2% change in precision of relevant results. The problem is iterated until the residuals (a measure of how well conservation laws are adhered to in each cell of the model) no longer change with

---

iteration. Additionally, monitors of the net heat flux or mass flow rate through the system may be used to indicate that the solution has converged.

In post-processing,  $\dot{Q}$  is measured as the surface integral of the heat flux through the stator walls.  $\dot{m}$  is measured as the surface integral of the air flux through the inlet or outlet.  $\dot{W}$  is calculated as in (2.29).

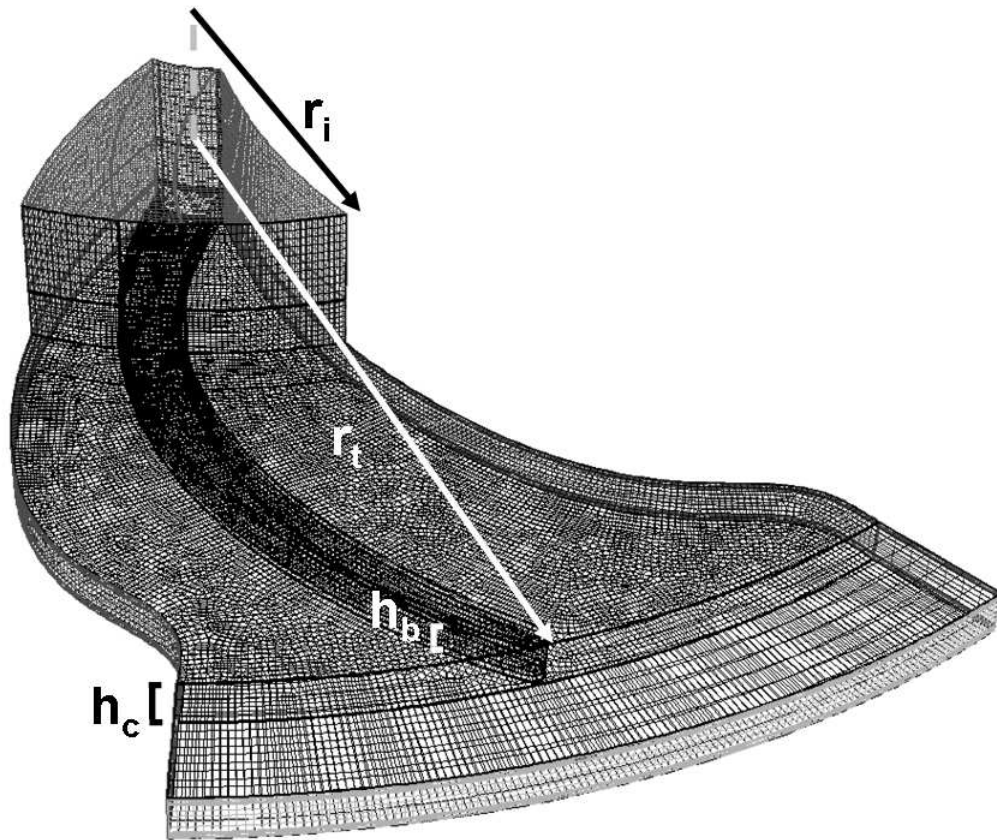


Figure 4.1: Structured CFD model grid. Grid is only shown on the face of solid–fluid and model boundaries, internal grid is not shown. The grid contains only one blade with rotational symmetry boundary conditions on the left and right sides. Fluid enters the model going downward through the inlet face at the top left and turns to flow radially outward. The rotor blade is visible inside the channel. This model is of an eight blade rotor and is representative of the dimensions and grid density of typical models. The length dimensions  $r_i$ ,  $r_t$ ,  $h_b$ , and  $h_c$  are labeled.

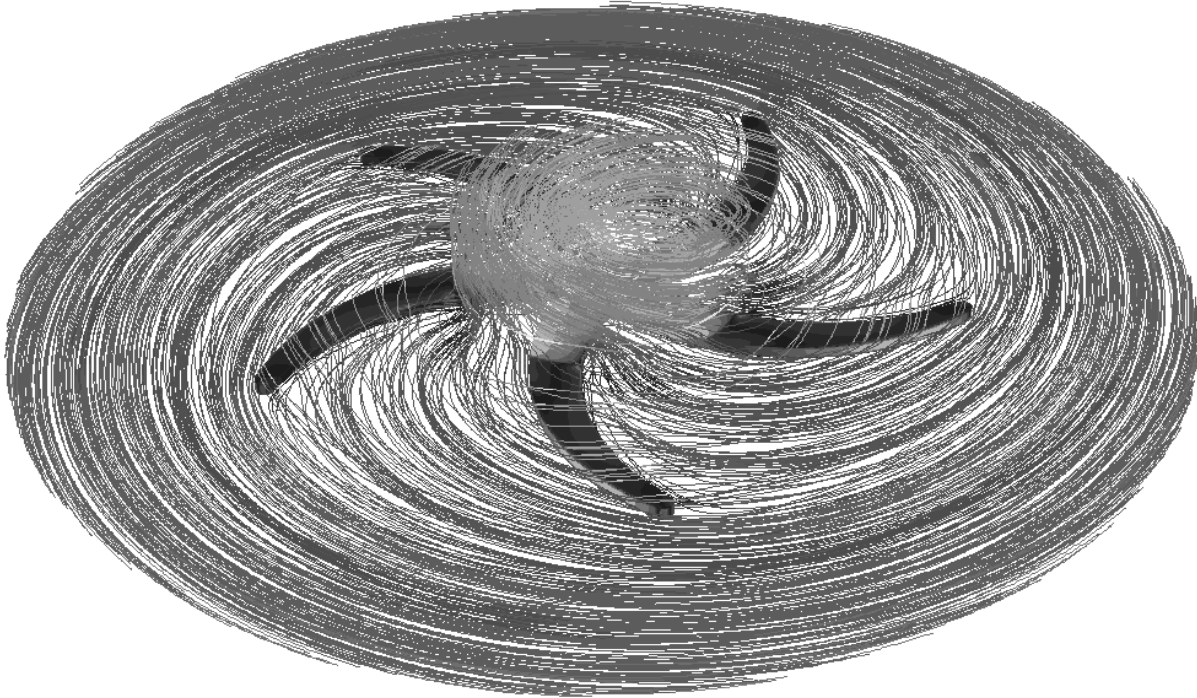


Figure 4.2: Plot of air pathlines in the rotor reference frame.

## 4.2 Computational Model Results

An example of a typical CFD model result is shown in Fig. 4.2. Pathlines of air flow are plotted in the relative frame of the rotor. Air enters from the top and turns radially outwards, following the blades. Some air slips behind the blade by passing above and below it. As air passes near the heated walls, it heats up as well.

The results of the CFD design studies were processed and are shown in Fig. 4.3, in which  $R$  (the convection thermal resistance of the single layer heat sink as defined in (2.51)) is plotted as a function of  $\dot{W}$  (the pumping power of the single layer heat sink as defined in (2.29)). In Fig. 4.3 different marker types are used to show various designs; these are interpreted in Table 4.1. All models shown in Fig. 4.3 have the height of the channel and the radius of the blade tip held constant at 2.2 and 50 mm, respectively. This was done to fix the volume consumed by the heat sink so that the thermal resistance and pumping power of different models could be compared on an equal basis. The models described in Table 4.1 can be categorized into four different design studies, each designed to optimize one of the following four variables: the number of blades per rotor, the blade sweep at the tip, the height of the blade in the channel, and the radius of the inlet passage. Models were

run at several different rotor angular velocities for each geometry, these angular velocities are also listed in Table 4.1. The results for each of the angular velocities are plotted with the corresponding marker. Data points with the same geometry (same marker type) but different speeds can be uniquely identified by noting that higher angular velocities always yield higher pumping power and lower thermal resistance. Table 4.1 also contains the data for  $\dot{m}$ ,  $\dot{W}$ , and  $R$ .

Data points closer to the origin represent designs that require low power and offer a low thermal resistance, making them better than other designs. The data points of Fig. 4.3 only span a narrow range, but they still give an idea of the tradeoff between  $R$  and  $\dot{W}$ . Some models in Fig. 4.3 correspond to the experimental data in Ch. 5. These sets of results will be compared in Ch. 7. Fig. 4.3 also shows a fit curve to the best performing data in the dataset. Defined for  $0.75 \text{ W} \leq \dot{W} \leq 2.6 \text{ W}$ , the equation for this curve is

$$R = 0.339\dot{W}^{-0.643} + 0.373 \quad (4.1)$$

One possible issue with these CFD models is that by pumping from atmospheric pressure to atmospheric pressure, these models do not account for the static pressure drop at the inlet due to either the acceleration of the flow from the quiescent environs to the inlet velocity or the inlet minor losses.

$$\Delta p_i = -(1 + K_i)q_i \quad (4.2)$$

Where  $\Delta p_i$  is the static pressure drop at the mouth of the inlet, relative to the ambient static pressure. The unity term accounts for the Bernoulli pressure drop, and  $K_i$  accounts for the inlet minor loss (0.5 for a sharp corner). Lastly,  $q_i$  is the dynamic pressure at the mouth of the inlet. Of course, some of this pressure drop is recovered as the fluid decelerates inside the device, but (4.2) is a conservative bound. Expected values of  $\dot{m}$  can be used to get an expected pressure drop that the heat sink will have to overcome. Then the CFD model is run with that adverse pressure gradient and the resultant mass flow rate and inlet pressure drop can be compared to the predicted value and the process can be iterated to convergence. When this process was followed for several models, the effect of the inlet pressure drop on the mass flow rate was found to be small for the flow rates associated with the single layer heat sink. For the models marked in Fig. 4.3 and Table 4.1 as diamonds and dotted triangles, the inlet pressure drop ranged from 4 to 13 Pa and the mass flow rates when the inlet pressure drop was not accounted for were no more than 1.5% more than the mass flow rates when this effect was accounted for. Thus, this effect need not be accounted for in the single layer model. In later chapters, this pressure drop was found to be significant and even dominant for multilayer heat sinks where a greater mass flow and much greater dynamic pressure is experienced at the mouth of the inlet. This greater pressure drop can significantly affect the mass flow rate of the multilayer heat sink versus the mass flow rate that would be expected from as many single layer heat sinks as there are layers in a multilayer heat sink. This reduction in mass flow rate will increase the thermal resistance of the multilayer heat sink because there is a lower thermal capacity flow rate through the heat sink. At the same time, the pumping power will be increased because the rotors are working against a larger pressure drop.

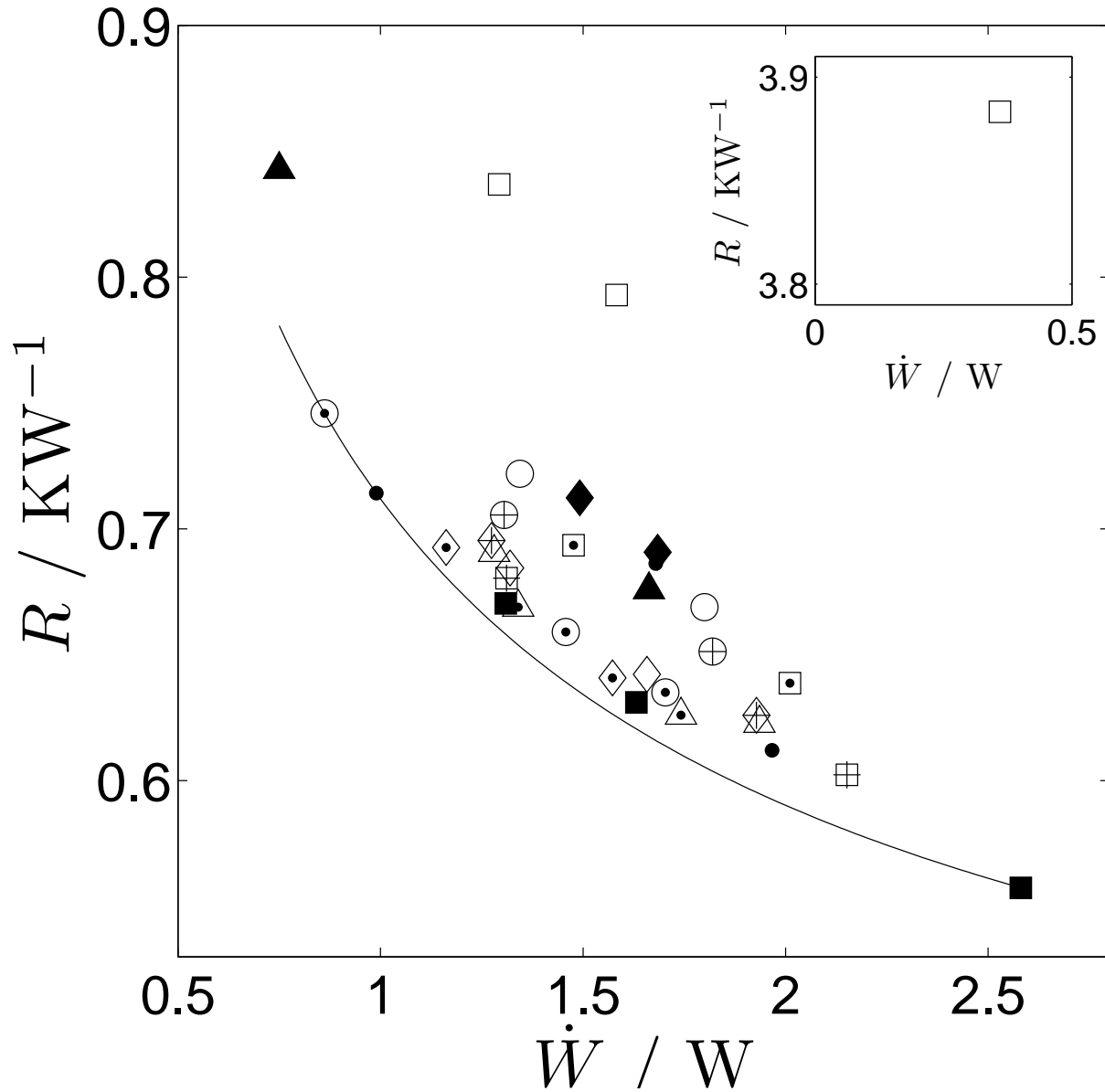


Figure 4.3: CFD model results. Plot of convection thermal resistance,  $R$ , versus pumping power,  $\dot{W}$ . The various symbols represent different designs and are interpreted in Table 4.1. Most data was taken in the vicinity of 1.5 W of pumping power, but one data point at a low pumping power and high resistance was taken; this point is shown inset. A fit curve is plotted as a solid line representing the best performance within the CFD models here.

Table 4.1: Specifications and performance of CFD models

Symbol	$r_i$ / mm	$h_b$ / mm	$n_b$	$\beta_b(r_t)$ / °	$\omega$ / rad s <sup>-1</sup>	$\dot{m}$ / g s <sup>-1</sup>	$\dot{W}$ / W	$R$ / KW <sup>-1</sup>
○	24	1.4	5	-20	[500, 550]	[5.10, 5.66]	[1.34, 1.80]	[0.722, 0.669]
⊙	24	1.4	8	-20	[400, 475, 500]	[4.49, 5.38, 5.68]	[0.862, 1.46, 1.70]	[0.746, 0.659, 0.635]
⊕	24	1.4	9	-20	[450, 500]	[5.11, 5.71]	[1.31, 1.82]	[0.706, 0.653]
●	24	1.4	13	-20	[400, 475, 500]	[4.46, 5.34, 5.67]	[0.989, 1.68, 1.97]	[0.714, 0.686, 0.612]
□	24	0.4	9	-20	[500, 750, 800]	[5.46, 5.88, 6.87]	[1.31, 1.63, 2.58]	[0.670, 0.631, 0.557]
◻	24	1.2	9	-20	[450, 500]	[5.23, 6.21]	[1.31, 2.15]	[0.680, 0.602]
⊞	24	1.6	9	-20	[425, 500]	[5.16, 5.74]	[1.48, 2.01]	[0.693, 0.639]
■	24	1.8	9	-20	[400, 430, 500]	[2.55, 4.01, 4.30]	[0.360, 1.29, 1.58]	[3.88, 0.837, 0.793]
△	24	1.6	9	-45	[480, 550]	[5.08, 5.86]	[1.28, 1.94]	[0.691, 0.623]
◀△	24	1.6	9	-60	[550, 600]	[5.38, 5.89]	[1.34, 1.74]	[0.669, 0.626]
▲	24	1.6	9	-80	[600, 780]	[3.87, 5.09]	[0.750, 1.66]	[0.843, 0.676]
◇	16	1.6	9	-45	[530, 570]	[3.51, 3.82]	[1.32, 1.66]	[0.684, 0.642]
◊	20	1.6	9	-45	[480, 530]	[4.19, 4.64]	[1.16, 1.57]	[0.693, 0.64]
◆	28	1.6	9	-45	[500, 520]	[5.96, 6.24]	[1.49, 1.68]	[0.712, 0.691]

### 4.3 Computational Model Conclusions

The results of the computational model were used to inform the design of the experiment discussed in the next chapter. It was found that for the single layer heat sink, the pressure drop created by accelerating the air flow from the ambient to the inlet velocity did not have a significant effect on the mass flow. Also, the number of blades per rotor was found to have little affect on the performance of the heat sink, thus this parameter may be varied to optimize other design goals, such as manufacturability. Similarly, the sweep of the blades at the tip was found not to have a significant effect on heat sink performance; however as blade sweep increases, the required rotor angular speed also must increase in order to maintain a constant pumping power. In this way, the design of the rotor may be tailored across a range of ratios of flow rate to rotor angular speed if a certain the flow rate and angular speed need to be varied independently. The computational results also found that for a given pumping power and a given channel height, an increased blade height will always reduce thermal resistance, although this is at variance with the experimental results. Lastly, an optimum inlet radius was found for a single layer heat sink of  $r_i = 20$  mm, although this optimum radius will change for a multilayer heat sink.

The CFD design study showed that when the data of Fig. 4.3 is interpolated such that  $\dot{W}$  is fixed to be 1.5 W, there is less than 8% variation in thermal resistance for rotors with blade numbers ranging from 5 to 13; there is no clear trend in the data. Thus the number of blades per rotor is not expected to affect heat sink performance. This lack of dependence on the blade number indicates that the quantity of flow that slips around the blade is not a function of blade number within the range tested.

Similarly, when  $\dot{W}$  is again fixed to be 1.5 W, there is less than 8% variation in thermal resistance for blade tip sweep angles ranging from  $-20^\circ$  to  $-60^\circ$ . Greater blade sweep causes larger  $\omega$  when  $\dot{W}$  is held constant, because more highly swept blades put less torque on the air and must turn faster to maintain an equal  $\dot{W}$  consumption. For the geometries described by the three triangle markers and the square with a ‘plus’ sign, in Table 4.1, every degree of increased blade back sweep requires the angular velocity to increase by nearly 5 radians per second to maintain 1.5 W of pumping power.

The next design study covers a variation in  $h_b$ . Since  $h_c$  is fixed for all CFD models, varying  $h_b$  changes the proportion of the channel that is filled by the blade. Again, this design study interpolates to  $\dot{W} = 1.5$  W. Thermal convection resistance decreases linearly as  $h_b$  increases. For  $h_b = 0.4$  mm,  $R = 0.80$  KW<sup>-1</sup> while for  $h_b = 1.8$  mm,  $R = 0.65$  KW<sup>-1</sup>. This improvement in performance could be attributed to the reduced distance between rotor and stator which increases the temperature gradient in the fluid at the stator wall. However, this result is at variance with the experimental results of Ch. 5 in which an optimum ratio of blade height to channel height is found that does not drive the height of the blade to be nearly the height of the flow channel.

The design study of the inlet radius found an optimum at  $r_i = 20$  mm ( $\mathcal{I} = 0.4$ ) that maximizes heat sink performance for the single layer heat sink. Smaller radii will cause too much pressure loss in the inlet and larger radii will consume too much stator surface area. This optimum radius has been selected for the physical experiment. However, this



---

optimal value is not very sensitive to  $r_i$ , with a variation of less than 10% across the range of  $16\text{mm} < r_i < 28\text{mm}$ . As mentioned previously in Ch. 2, the optimum inlet radius of a multilayer heat sink is likely to be larger because of its higher flow rates.

# Chapter 5

## Experimental Model

### 5.1 Description of Apparatus

In this chapter, an experiment to test the results of models in the previous chapters is discussed. The experiment models a single layer heat sink. The experimental setup is shown in Fig. 5.1. The condensing section of the heat pipe system is simulated by two square copper plates, each backed by four polyimide film heaters. These combinations of copper plates and heaters are referred to as stator analogs. The copper plates are 6.35 mm (1/4 inch) thick and 101.6 mm (4 inch) to a side plates. The top plate has a 40 mm diameter hole through its center to allow air intake. This is the optimal diameter for a single-layer heat sink as determined by CFD models. The sides of the plates facing the flow were supplied with a polished finish, and every effort has been made to minimize scratching or tarnishing the plates. The heaters are connected thermally and electrically in parallel and powered by a DC power supply. The exterior side of each stator analog is insulated with thermal insulation to reduce the thermal power lost to the environment other than through the flow channel. The top piece of insulation has a round at the inlet hole to reduce inlet pressure losses. Sec. 5.4.1 provides estimates of thermal power losses through various directions, including the thermal insulation. The aforementioned components are mounted atop an aluminum table fixed to an optical table. The top copper plate is mounted above the bottom plate with round shims in the corners. The plates, insulation, and shims, have clearance holes and are fastened with machine screws to the aluminum table. Adding or removing shims allows  $h_c$  to be varied. These components are shown in Fig. 5.1 a and b.

All thermocouples used are Omega Engineering, Inc. # 5TC-TT-J-30-36 with limits of error of 2.2°C and a bead junction of diameter 0.5 mm. Three thermocouples are embedded in each copper plate, with thermal grease, at increasing radii from the center to test the isothermality of the plates. Another thermocouple is placed above the top thermal insulation piece and another sandwiched between the bottom thermal insulation piece and the aluminum table, to quantify thermal power losses through the top and bottom.

A rotor is shown in Fig. 5.1c. The rotor is cut out of acrylic sheets of a variety of thicknesses so as to create a variety of blade heights ( $h_b$ ) with a laser cutter programmed by a CAD file. The rotor blades are shaped as the trailing end of an NACA 0011 airfoil. The blade angle sweeps smoothly backward from the root to a sweep of  $-45^\circ$ . The trailing edge was rounded off with a circular arc of radius 1.3 mm. This description of the blade design is offered for the benefit of future workers in this research area. After experimentation with rotors of a variety of numbers of blades, five blades was selected because this number gives blades that are wide enough to prevent warping due to laser heating and because five is an

odd number, staggering any possible effects of blades interacting with the vertical posts.

A rotor is mounted to the shaft which passes through a central hole on the bottom stator analog, bottom insulation, and the aluminum table. This shaft is supported by two self-aligning, double row, unshielded, oiled ball bearings which are in turn fixed to a 5-degree of freedom translation and rotation stage which is fixed to the same optical table as the aluminum table. The 5-degree of freedom stage allows the rotor to be positioned precisely within the flow channel. The shaft is driven by a commercially supplied DC motor; the two are connected by a flexible coupling. A reflective material was taped to the shaft as a target for a laser tachometer which measures angular velocities.

## 5.2 Power Calibration

The electrical power into the motor,  $\dot{W}_i$ , is consumed in three components: motor losses ( $\dot{W}_\eta$ ), mechanical losses ( $\dot{W}_m$ ), and pumping power ( $\dot{W}$ ).

$$\dot{W}_i = \dot{W}_\eta + \dot{W}_m + \dot{W} \quad (5.1)$$

The pumping power,  $\dot{W}$ , can be determined by a calibration of the motor, shaft, and bearings with and without the rotor. The motor's efficiency is defined as the ratio of shaft power output to electrical power input.

$$\eta = \frac{\dot{W}_m + \dot{W}}{\dot{W}_i} \quad (5.2)$$

$\eta$  is a function of  $\omega$  and  $\dot{W}_i$ . Now, the input electrical power,  $\dot{W}_i$ , is the product of voltage,  $V$ , and current,  $I$ .

$$\dot{W}_i = IV \quad (5.3)$$

The shaft power is the sum of the mechanical power losses and the pumping power.

$$\dot{W}_m + \dot{W} = \dot{W}_i - \dot{W}_\eta = K_e \omega I \quad (5.4)$$

where  $K_e$  is the motor's back EMF constant:

$$K_e = \frac{V - IR_{\text{arm}}}{\omega} \quad (5.5)$$

Where  $R_{\text{arm}}$  is the armature resistance of the motor. Combining (5.4) and (5.5), the shaft power is  $\dot{W}_i$  minus the energy lost due to resistive heating in the motor,  $\dot{W}_\eta$ , which is the motor power loss.

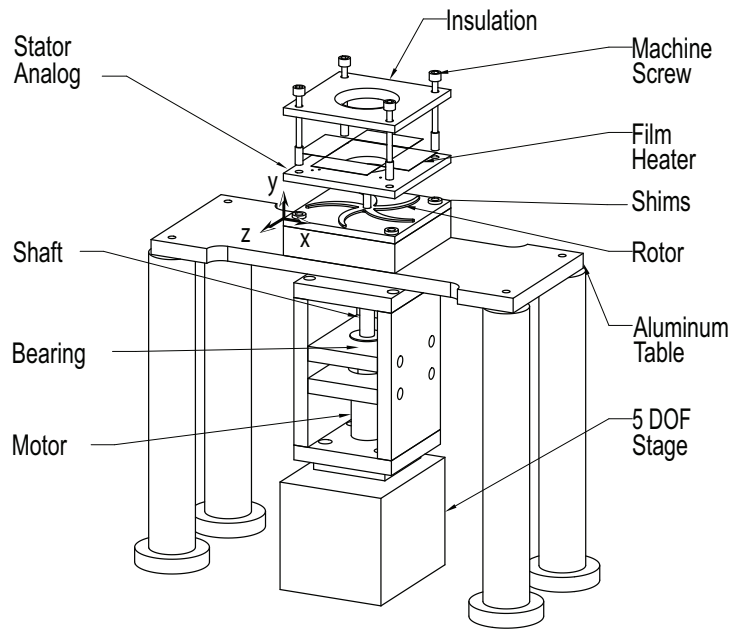
$$\dot{W}_\eta = I^2 R_{\text{arm}} \quad (5.6)$$

The motor and bearing losses are calibrated by subtracting the shaft power output without the rotor from the shaft power output with the rotor to remove the effects of mechanical losses (most of which is in the bearings), giving the pumping power.

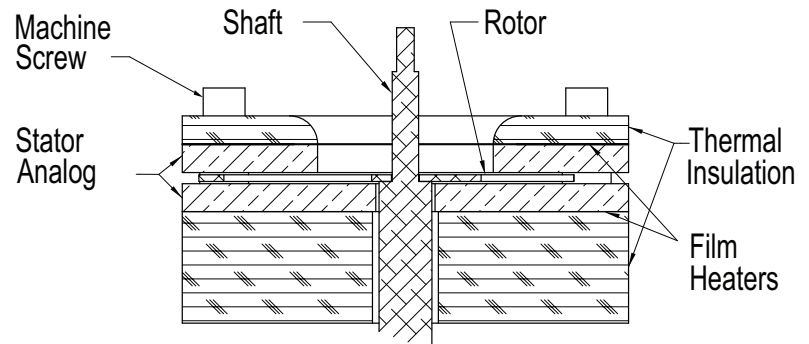
$$\dot{W} = \eta \dot{W}_i - \eta_{\text{unload}} \dot{W}_{\text{unload}} \quad (5.7)$$

Where  $\dot{W}_{\text{unload}} = \dot{W}_\eta + \dot{W}_m$  and  $\eta_{\text{unload}}$  is the motor efficiency at the unloaded condition, which is separately calibrated.

a.)



b.)



c.)

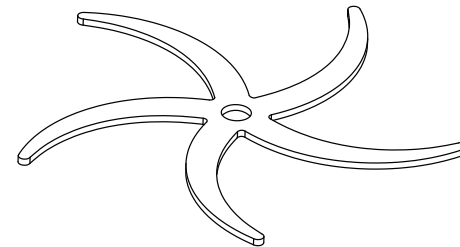


Figure 5.1: **a.** Experimental setup, exploded view. The coordinate system in (a.) is also used in Fig. 5.2, Fig. 5.3 and the text. **b.** Side cutaway view of air flow test section. **c.** Oblique view of rotor.

## 5.3 Air Flow Experiments

When air velocity and mass flow is to be measured, a single wire hot-wire anemometer (TSI Inc. model # 1210-60) is mounted to a horizontal and vertical translation stage that allows rastering across the entire exit plane. Hot-wire anemometry was selected for its minimal impact on the flow, making measurement of the mass flow possible without the large pressure drops associated with flow meters and similar techniques.

### 5.3.1 Hot-Wire Anemometer Technique

Hot-wire anemometry measures 1, 2, or 3 velocity components. Hot-wire probes require as many wires as velocity components to be measured. If there are fewer wires than non-zero velocity components, the probe measures an effective cooling velocity, which is the velocity that would create the same amount of cooling if it were approaching the probe head on.

In this application, the flow immediately downstream of the heat sink exit is mostly 2 dimensional, having  $x$  and  $z$  components (the coordinate system is defined in Fig. 5.1 a). The wire length was approximately 4 mm, which would make a multi-wire probe too large to measure the flow exiting the channel. A single wire probe was selected because the wire could be oriented along the width of the channel. Two scans of the probe were required to resolve the  $v_x$  and  $v_z$  velocity components.

The hot-wire probe is oriented at angles of  $45^\circ$  and  $-45^\circ$  to the exit plane, referred to as sensor orientations A and B, as seen in Fig. 5.2, and repeatedly scanned in both the vertical and horizontal directions, less than one channel height downstream of the exit of the channel. The direction of the mean flow is calculated from the components measured at the two hot-wire orientations. The flow rate is then calculated as the integral over the exit plane of the velocity component normal to the exit plane.

A more detailed explanation of the calculation of exit plane velocity follows. The effective cooling velocity,  $v_e$  as measured by the hot-wire anemometer is calculated by King's law [20]:

$$v_e = \left( \frac{V_h^2 - c_0}{c_1} \right)^2 \quad (5.8)$$

where  $V_h$  is the voltage signal of the anemometer, and  $c_0$  and  $c_1$  are constants determined by calibration with a flow of known speed. The data is filtered to remove high frequency components due to turbulence, since only mean flow is considered. As seen in Fig. 5.2, the hot-wire probe is oriented in the plane of the exit flow, which creates a plane jet. The probe is very close to the exit plane, and thus the out-of-plane velocity is expected to be zero and the hot-wire probe is expected to have zero pitch angle with respect to the local flow. Since there are no out-of-plane velocity components,  $v_e$  can be decomposed into it's normal and transverse components to the wire, in plane with the plane jet and the hot-wire probe [21]:

$$v_e = \left( v_N^2 + k^2 v_T^2 \right)^{1/2} \quad (5.9)$$

where  $k$  is known as the yaw factor, an indication of a hot-wire probe's sensitivity to yaw with respect to the flow direction. Yaw factors are available in the literature for various models of hot-wire probes as a function of both flow speed and yaw angle [22]. Since  $k$  is mutually dependent with flow angle and speed, the value of  $k$  in given conditions is determined by an iterative process. It is apparent from the equalities in Fig. 5.2 that the effective cooling velocity for both sensor orientations can be written

$$\begin{bmatrix} v_{eA}^2 \\ v_{eB}^2 \end{bmatrix} = \begin{bmatrix} 1 & k^2 \\ k^2 & 1 \end{bmatrix} \begin{bmatrix} v_{NA}^2 \\ v_{TA}^2 \end{bmatrix} \quad (5.10)$$

where  $A$  and  $B$  subscripts indicate the sensor orientation. The vector on the right hand side of (5.10) is solved by elimination. The magnitude and orientation of the flow with respect to the normal of orientation  $A$  are

$$\|\vec{v}_e\| = \left( v_{NA}^2 + v_{TA}^2 \right)^{1/2} \quad (5.11)$$

and

$$\alpha_A = \arctan \left( \frac{v_{TA}}{v_{NA}} \right) \quad (5.12)$$

from Fig. 5.2, the flow angle with respect to the normal to the exit plane of the device is

$$\gamma = 45^\circ - \alpha_A \quad (5.13)$$

and the flow components normal and transverse to the exit plane are

$$\begin{bmatrix} v_z \\ v_x \end{bmatrix} = \|\vec{v}_e\| \begin{bmatrix} \cos \gamma \\ \sin \gamma \end{bmatrix} \quad (5.14)$$

$v_z$  is then integrated over the width and height of the exit plane and multiplied by the air density to acquire  $\dot{m}$ . Note that the  $x, y, z$  coordinate system used in (5.14) is used throughout the text and is depicted in Fig. 5.1, Fig. 5.2, and Fig. 5.3.

### 5.3.2 Outflow Jet Entrainment

The effect of flow entrainment in the jet is accounted for in the calculation of  $\dot{m}$ . The plane jet exiting the device is a free shear flow with excess momentum. The shearing effect of the jet on the surrounding fluid causes a diffusion of momentum outwards and entrains new fluid into the jet. Thus, any downstream measurement of flow rate in a free shear flow must account for entrainment effects in order to determine the volumetric flow rate at the exit,  $\dot{V}_o$ . Kotsovinos offers a correlation of entrainment for plane jets as a function of distance downstream of the flow exit,  $z$ , in the zone of flow establishment ( $z/h_c < 6$ ). The zone of flow establishment is the region in which information about changes in momentum at the edge of the jet has not yet reached the core of the jet, a similar concept as developing flow in a pipe [23]. This correlation is

$$\frac{d\dot{V}_s}{dz} = 0.064\bar{v}_z|_o \quad (5.15)$$

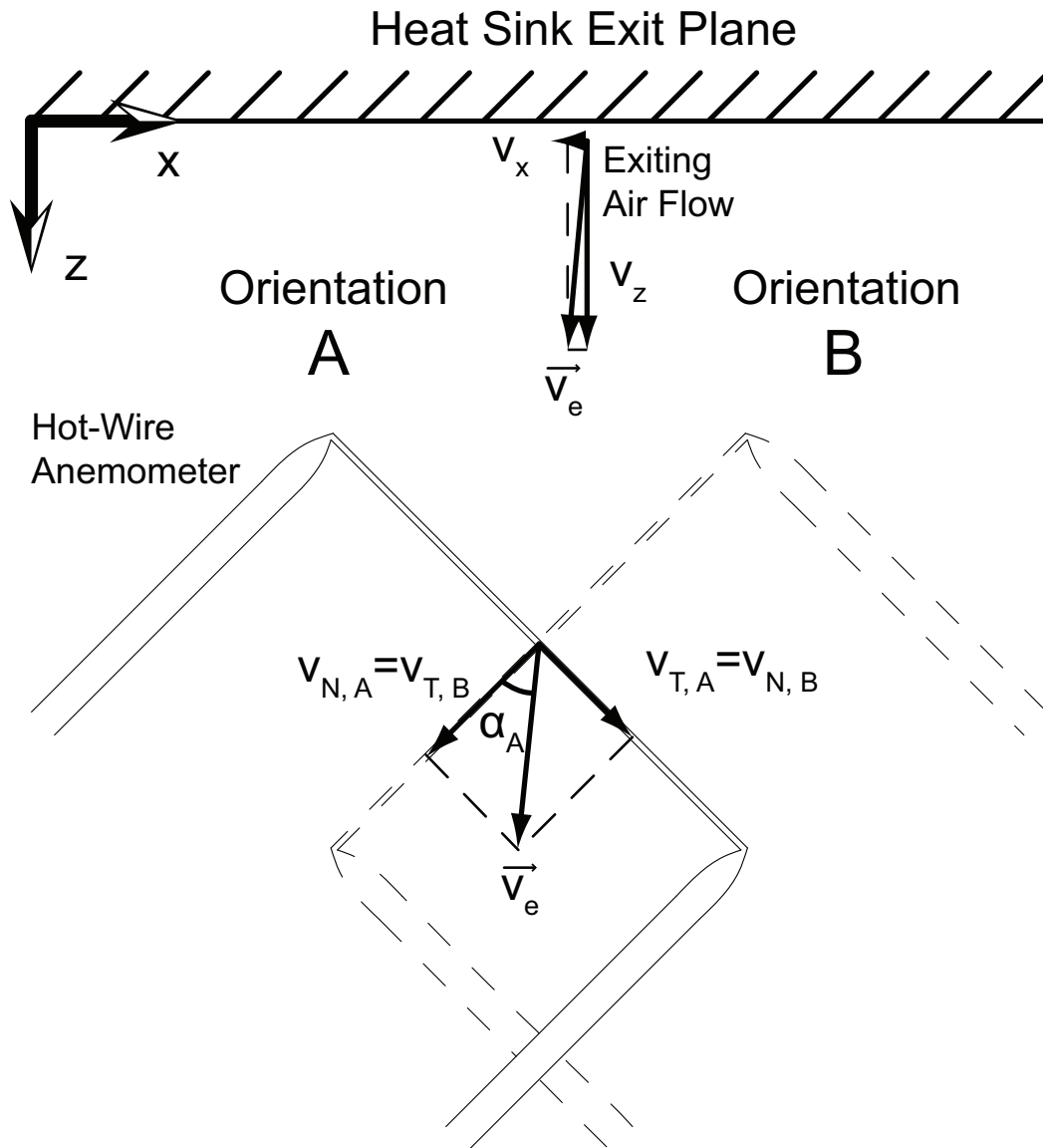


Figure 5.2: Diagram of exit air flow velocity,  $\vec{v}_e$ , as measured by hot-wire anemometer in orientations A (solid lines) and B (dashed lines). View is from above, air exits heat sink at top of figure and convects across hot-wire anemometer downstream of exit. The coordinate system in the top left is also used in Fig. 5.1, Fig. 5.3 and the text.

where  $\dot{\mathcal{V}}_s(z)$  is the volumetric flow rate of the jet per unit width of the channel at position  $z$  downstream of the exit and the  $s$  subscript indicates that the equation is per unit span of the jet so that (5.15) has units of length per time.  $\bar{v}_z|_o$  is the bulk velocity normal to the exit plane at the jet exit. Note that (5.15) assumes a rectangular velocity profile at the exit of the flow from the channel, while the velocity profile exiting the device is not rectangular, but is somewhat rounded in the vicinity of the stator walls. Now define  $L$  as the length of a side of the heat sink then the span of the jet exiting the device is  $4L$ . The volumetric flow rate at position  $z$  can be written as a function of the volumetric flow rate at the exit plane,  $\dot{\mathcal{V}}_o$ , as

$$\dot{\mathcal{V}}(z) = \dot{\mathcal{V}}_o \left( 1 + 0.064 \frac{z}{h_c} \right) \quad (5.16)$$

which may then be rearranged to solve for  $\dot{\mathcal{V}}_o$ .

$$\dot{\mathcal{V}}_o = \frac{\dot{\mathcal{V}}(z)}{1 + 0.064z/h_c} \quad (5.17)$$

where  $\dot{\mathcal{V}}(z)$  is the measured volumetric flow rate when the sensor is distance  $z$  downstream of the exit. The hot-wire probe must be located slightly downstream of the exit, but the effect of flow entrainment on the measured mass flow rate can be removed with (5.17).

The velocity at which air is entrained into the jet in the zone of flow establishment is

$$v_{\text{entrain}} = 0.064 \frac{\dot{\mathcal{V}}_o}{4h_c L} \quad (5.18)$$

$v_{\text{entrain}}$  is shown in Fig. 5.3. The linear nature of Equation (5.15) makes  $v_{\text{entrain}}$  a constant value as a function of  $z$  in the zone of flow entrainment, which is the region that the hot-wire anemometer is located.  $v_{\text{entrain}}$  is used to define a freestream velocity adjacent to the side walls of the experiment.

## 5.4 Heat Transfer Experiments

When experiments related to heat transfer are carried out, a thermocouple is fixed to a vertical translation stage that allows the thermocouple to scan the temperature profile at the exit of one side of the heat sink, between the two plates. This stage may also be moved side to side to allow measurement of temperature across the width of the device, at the exit plane. Several scans of temperature from bottom to top of the channel, at various horizontal positions are made. This data is later assembled to determine the bulk temperature of the flow at the exit by taking the mass-weighted average of the exit temperature data. Alternate means of determining the bulk temperature, such as adiabatic mixing via baffles, would cause unacceptably large pressure drops and dramatically affect the flow.

Heat transfer experiments are controlled through a National Instruments Labview program that controls motor power and takes in temperature, angular speed, and potentiometer voltage, and records all of this data.



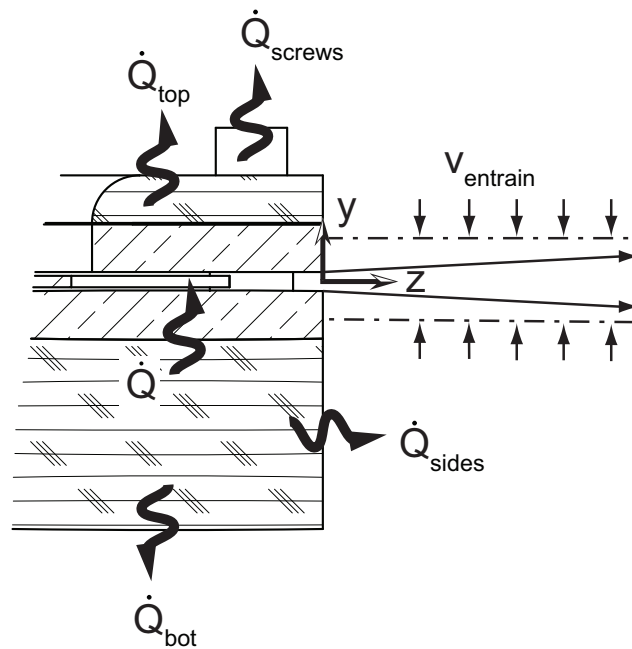


Figure 5.3: Cutaway view of jet entrainment and heat loss mechanisms. The plane jet exiting the heat sink entrains air at velocity  $v_{\text{entrain}}$ . Thermal power losses from equation (5.19) are shown diagrammatically. The coordinate system in the center of the figure is also used in Fig. 5.1, Fig. 5.2 and the text.

### 5.4.1 Heat Loss Analysis

There are several directions through which the heat generated in the resistive heaters may be sunk to the environment. Heat loss through mechanisms other than forced convection along the stator analog walls are quantified and minimized to determine how much thermal power is actually sunk through the walls of the stator analogs. Other than through forced convection along the stator analog walls, heat may also pass through the side walls of the copper plates and thermal insulation, as well as through the top insulation to the ambient air and through the bottom insulation to the aluminum table. Lastly, thermal power may conduct through the machine screws in the corners and convect into the ambient air or conduct through the aluminum plate. Fig. 5.3 depicts each of these loss mechanisms.

$$\dot{Q}_{\text{in}} = \dot{Q} + \dot{Q}_{\text{top}} + \dot{Q}_{\text{bot}} + \dot{Q}_{\text{sides}} + \dot{Q}_{\text{screws}} \quad (5.19)$$

Where  $\dot{Q}_{\text{in}}$  is the electrical power into the resistive heaters,  $\dot{Q}$  is the power sunk by the heat sink through the intended heat flow path,  $\dot{Q}_{\text{top}}$  and  $\dot{Q}_{\text{bot}}$  are the power lost through the top and bottom insulation,  $\dot{Q}_{\text{sides}}$  is the power lost through the sides, and  $\dot{Q}_{\text{screws}}$  is the power lost through conduction through the screws to the environment.

Thermal power lost through conduction in the top and bottom insulation is calculated by measurements of the temperature difference across the insulation, coupled with knowledge of the thermal conductivity of the thermal insulation and the dimensions of the insulation.

$$\dot{Q}_{\text{top,bot}} = \frac{T_s - T_{\text{top,bot}}}{R_{\text{top,bot}}} \quad (5.20)$$

where  $T_{\text{top,bot}}$  is the insulation temperature at the surface opposite the resistive heaters, and

$$R_{\text{top,bot}} = \frac{t_{\text{top,bot}}}{\kappa_{\text{insul}} A_{\text{top,bot}}} \quad (5.21)$$

is the 1-dimensional thermal conduction resistance through the thermal insulation. The thermal resistance in the aluminum table from the bottom surface of the bottom insulation is assumed to be negligible in comparison to  $R_{\text{bot}}$ , which gives a conservative estimate of  $\dot{Q}$ . On the top surface, both the thermal resistance of conduction through the insulation and the thermal resistance of convection on the top surface of the top insulation are both non-negligible. The behavior of the convective heat transfer on the top surface of the insulation is further explored in Appendix B.

Thermal power lost through the side walls is determined by application of Nusselt correlations available in the literature. The side walls are heated and thus creating buoyant convection in the surrounding air, but the air flow being entrained into the jet exiting the experiment is a forced convection. The Richardson number indicates the degree to which convection is buoyant, forced, or mixed.

$$Ri = \frac{g\beta(T_{\text{side}} - T_{\text{amb}})l_{\text{side}}}{v_{\text{entrain}}^2} \quad (5.22)$$

$g$  is gravitational acceleration,  $\beta$  is the volumetric thermal expansion coefficient,  $T_{\text{side}}$  is the mean temperature of the side walls, and  $l_{\text{side}}$  is the height of the side walls. This dimensionless ratio was found to always be less than 1, indicating that the forced convection induced by jet entrainment dominates over buoyant convection.  $\dot{Q}_{\text{sides}}$  is then found via flat plate Nusselt correlation along the side wall.

The thermal resistance through the screws was calculated by measuring the temperature at the top and bottom surfaces of the screws as well as the ambient temperature and calculating the thermal resistance in the screws to determine the thermal resistance to the air from the screws. The shaft of the screws are turned down so that there is an 850  $\mu\text{m}$  gap between the copper plates and the screws. This air gap is small enough that the Rayleigh number is below the critical value at which convection cells begin to develop in the annulus. Thus the air in the annulus can be treated as a conducting body only, raising the thermal resistance of the heat loss path through the screw.

The sum of the loss mechanisms is on the range of 9–15% of  $\dot{Q}_{\text{in}}$ . In this way  $\dot{Q}$  is calibrated for these rather small thermal losses.

## 5.5 Results and Analysis

Experiments have been done with 10 different geometries in which the channel height has a range of 1.6–3.4 mm and the blade height has a range of 0.5–2.8 mm, corresponding to dimensionless length ratios,  $G = h_c/r_t$  and  $B = h_b/r_t$  of  $0.032 \leq G \leq 0.068$  and  $0.010 \leq B \leq 0.049$ . Angular speed ranges over 3000–7000 rpm; which corresponds to  $4.7 \times 10^4 \leq Re_\omega \leq 1.1 \times 10^5$ .

The three thermocouples in each plate were found to be isothermal to within a few tenths of a degree Celsius, on the order of the relative precision of the thermocouples and well below their absolute accuracy. This shows that the stator analogs were sufficiently thick and thermally conductive to spread the heat of the resistive heaters uniformly, indicating that convection resistance dominates over conduction, as in the physical heat sink. This validates the design of the copper plates and resistive heaters as analogs to the stators. The top plate tends to be about 2°C hotter than the bottom plate because it has less surface area but the same thermal power input. The stator wall temperature,  $T_s$ , refers to the mean of the top and bottom wall temperatures.

Fig. 5.4 a shows a typical contour plot of  $v_z$ , created by scans of the hot-wire anemometer in the  $x$  and  $y$  directions, as measured slightly downstream of the exit plane. The no-slip condition applies to the surfaces of the stator analogs, however, because the flow must be measured downstream of the exit, the measured  $v_z$  is greater than zero at the locations downstream of the walls of the stator analogs due to the expansion of the jet. The velocity profile in the  $x$  direction is affected by the length of the path through which a particle of fluid must travel, as well as the corner locations of the 4 screws. The low velocity region corresponding to  $x = 80$  to 100 mm in Fig. 5.4 a is due to a shadowing effect by the screw and shims that pass through the corner of the channel. These screws and shims are located 6 mm behind the exit plane at  $x$  positions of 6–15 mm and 85–94 mm in Fig. 5.4 a. The

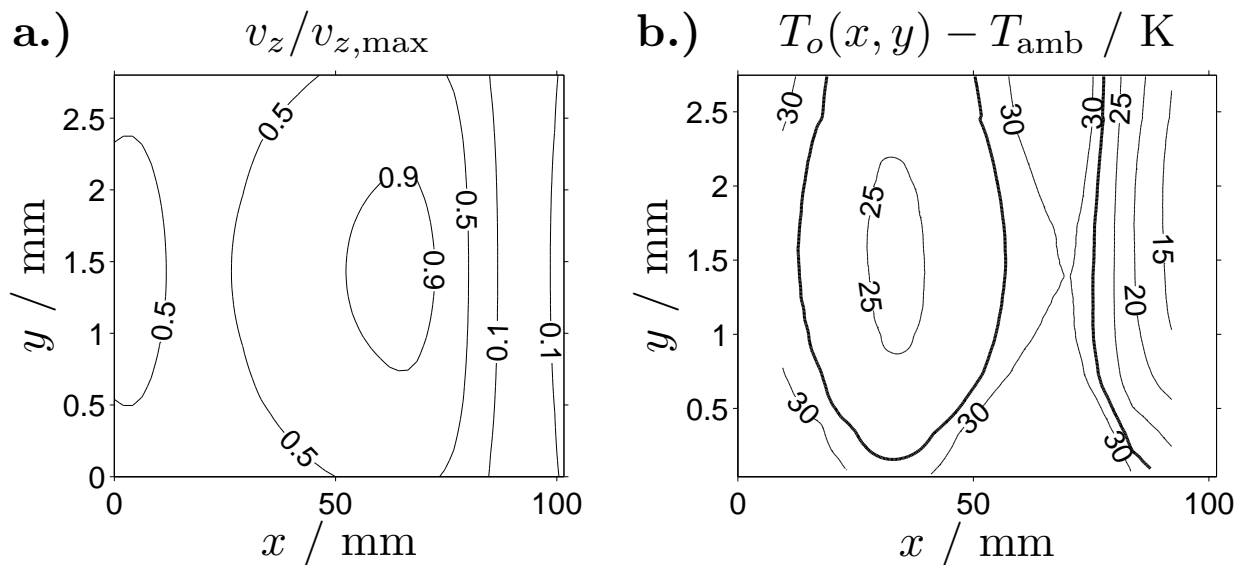


Figure 5.4: **(a.)** Normalized air velocity in the normal direction to the exit plane, averaged over various geometries. Air flow measured slightly downstream of the exit, generally 2 mm. Rotor rotates from right to left, axes are to different scales. **(b.)** Representative plot of air isotherms on experiment exit plane.  $\bar{T}_o - T_{\text{amb}}$  isotherm plotted in bold.  $\dot{Q} = 89 \text{ W}$ ,  $h_b = 1.65 \text{ mm}$ ,  $h_c = 2.8 \text{ mm}$ , angular speed of 3 krpm,  $\dot{m} = 3.69 \text{ g s}^{-1}$ ,  $\bar{T}_o - T_{\text{amb}} = 28.5 \text{ K}$ ,  $T_s - T_{\text{amb}} = 56.6 \text{ K}$

right side is particularly blanked by the flow because the rotor rotates from right to left and the stagnation line on the shims is directly opposite the measurement plane. The region near  $x = 60$  mm has a higher velocity because fluid particles exiting here experience a shorter path and therefore less frictional loss through the device.

The temperature at the exit plane is not uniform but varies as a function of distance from the stator plate analogs and to a lesser degree along the width of the exit due to variations in the residence time for fluid particles exiting at different locations. Fig. 5.4b shows a typical  $T_o$  profile.  $T_o$  is higher near the stator plate analogs, at  $y = 0$  mm and  $y = 2.8$  mm, although this effect is somewhat less in the case shown here because  $\dot{m}$  is low and  $\dot{Q}$  is high. The region on the right side, that is blanked by the shims is significantly cooler because the air in that region does not travel through the device, but recirculates from the environment.

The bulk temperature at the exit,  $\bar{T}_o$ , is calculated as the mass-weighted average of  $T_o$ . The location of the position where  $\bar{T}_o = T_o$  has been found to not vary significantly over  $\dot{Q}$  or  $\dot{m}$ . A reliable position was selected, and future data measure  $\bar{T}_o$  as the temperature at that position. The thermocouple was positioned approximately 2 mm inside of the exit plane to ensure that the thermocouple does not interact with air entrained by the exiting jet.

## 5.6 Correlations and Design Charts

The results of the experiment are converted into nondimensional form using the equations in Ch. 3 above and the results are fitted over relevant independent parameters. To recap, the dependent parameters are:  $C_f$ , the flow coefficient (the nondimensionalized mass flow rate),  $\varepsilon$ , the heat exchanger effectiveness ( a measure of the heat input into the system to the maximum possible heat input to the system), and  $\sigma$ , the slip factor (the ratio of the azimuthal air velocity at the blade tip to the blade tip speed). A larger  $\sigma$  indicates that the flow follows the blade well (i.e. the flow slips over the blade less). The independent parameters are  $G = h_c/r_t$ , the aspect ratio of the flow channel,  $B = h_b/r_t$ , the aspect ratio of the blade,  $Re_\omega = \rho\omega r_t^2/\mu$ , the rotational Reynolds number, and  $Pr$ , the Prandtl number of the convecting fluid (air).

First, the raw data was converted into nondimensional form as defined in Ch. 3. Then curves were fit to the dependent parameters as a function of the independent parameters and the fit equations were simplified by removing insignificant terms.

A least-squares fit curve was applied to the data for the first independent parameter,  $C_f$ , taking into account  $G$ ,  $B$ , and  $Re_\omega$ . The fit curve of (5.23) is plotted against the experimental data in Fig. 5.5 a.  $C_f$  was found not to be a function of  $Re_\omega$  in the range of

the experiment; thus the fit is only a function of  $G$  and  $B$ .

$$C_f = 0.32G + 2.4B - 0.035B/G$$

for

$$\begin{aligned} Pr &= 0.7 \\ \mathcal{I} &= 0.4 \\ 4.7 \times 10^4 &\leq Re_\omega \leq 1.1 \times 10^5 \\ 0.032 &\leq G \leq 0.068 \\ 0.010 &\leq B \leq 0.049 \\ B &\leq G - 0.012 \end{aligned} \tag{5.23}$$

The last line of (5.23) stipulates that  $B$  is less than  $G$  so that the blade can fit in the channel; the constant offset is due to the fact that there is a minimum spacing in which the blade can be spun within the channel without striking the walls. The standard deviation of the difference between the experimental data and the fit curve of (5.23) is 0.0038.

$C_f$  is so independent of  $Re_\omega$  that there are groupings of 3 points in Fig. 5.5 a which correspond to the data points taken at three different  $Re_\omega$  but with other independent parameters the same. This independence from  $Re_\omega$  means that the flow rate is linearly proportional to  $\omega$ , as  $\omega$  appears in the denominator of the definition of  $C_f$ .  $C_f$  is positively correlated with both  $G$  and  $B$ , although  $B$  has the stronger effect.

Increased  $G$ , which is a decrease in the channel aspect ratio, allows more fluid to flow through the channel with less frictional interaction with the wall, thereby increasing the flow rate. Increased  $B$ , a decrease in the blade aspect ratio, increases the size of the leading and trailing faces (pressure and suction surfaces, respectively) of the blade, positively affecting  $C_f$ . Note that in the limit of  $B$  approaching zero,  $C_f$  will not approach zero, due to viscous shear of air on the top and bottom surfaces of the blade. Extrapolation of the fit suggests that in the limit of  $B$  approaching zero,  $C_f$  is on the order of 0.01 to 0.02, across the range of  $G$ . The values of  $C_f$  tend to be much less than 1 because the largest length variable in the nondimensionalization,  $r_t$ , is used as the generating length scale. If  $C_f$  were renormalized such that the length scales corresponded to the volume of the rotors, this renormalized  $C_f$  would be on the order of 1.

Similarly, a least-squares fit curve was applied to the  $\varepsilon$  data, taking into account  $G$ ,  $B$ , and  $Re_\omega$ . The  $Re_\omega$  terms were again found to be negligible in comparison to the other terms so the  $Re_\omega$  terms were dropped and a new fit was applied.

$$\varepsilon = 1 - 7.2G + 4.5B - 0.55B/G \tag{5.24}$$

With the same bounds on the independent variables as the fit for  $C_f$ . This fit is plotted against the experimental data in Fig. 5.5b. The standard deviation of the difference between the experimental data and the fit curve is 0.038.  $\varepsilon$  is positively correlated with decreasing  $B$  in the range considered. To a lesser degree,  $\varepsilon$  is positively correlated with decreasing  $G$  in most of the range considered. Lower  $B$  causes the flow to be driven less effectively, thereby increasing the residence time. Lower  $G$  reduces the mean distance from the wall surface to any point in the fluid, which increases the interaction of the fluid with the wall,

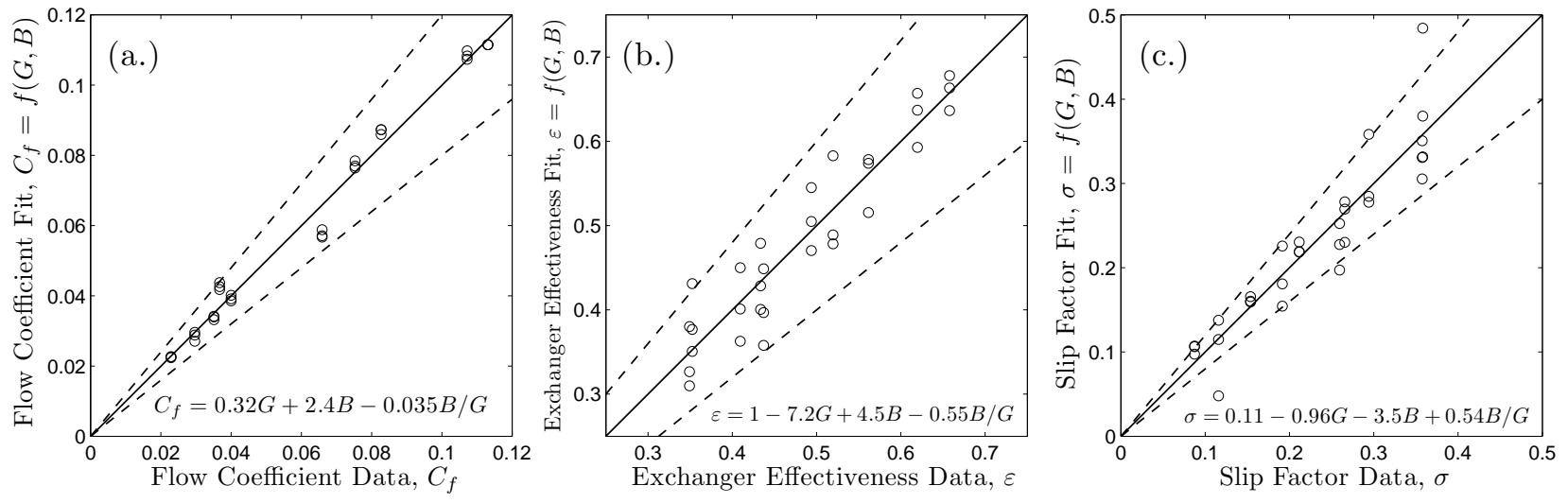


Figure 5.5: Plot comparing experimental data with fit equations of independent parameters:  $C_f$ ,  $\varepsilon$ , and  $\sigma$ . A perfect fit would fall along the solid lines; the dashed lines indicate  $\pm 20\%$  variation. Fit equations shown inset.

increasing heat transfer. In the limit where  $G$  and  $B$  both go to zero,  $\varepsilon$ , as fit by (5.24) goes to one, as would be expected for any single stream heat exchanger for which the wetted perimeter is insignificant in comparison to the flow length.

$\varepsilon$  was found to have a slight negative correlation with  $Re_\omega$ , but this effect was negligible (this was only a few percent effect) in comparison to the effects of  $G$  and  $B$ . Lower  $Re_\omega$  allows the fluid a longer residence time in the device, causing the flow to attain higher  $\varepsilon$ .

Note that  $C_f$  increases with increasing  $G$  and  $B$ , while  $\varepsilon$  decreases with these variables.  $C_f$ ,  $\varepsilon$ , and  $Re_\omega$  all appear in (3.12), meaning that some optimum must be found to balance these competing elements to minimize the thermal resistance in the air.

Lastly, a fit curve was applied to the  $\sigma$  data, taking into account  $G$ ,  $B$ , and  $Re_\omega$ . As above, the  $Re_\omega$  terms were found to be negligible in comparison to the other terms so the  $Re_\omega$  terms were dropped and a new fit was applied. This fit is:

$$\sigma = 0.11 - 0.96G - 3.5B + 0.54B/G \quad (5.25)$$

With the same bounds on the independent variables as the fit for  $C_f$ . This fit is plotted against the experimental data in Fig. 5.5c. The standard deviation of the difference between the experimental data and the fit curve is 0.037.  $\sigma$  tends to increase as the ratio  $B/G$  increases, since this ratio describes the fraction of the channel height that the blade fills. As the channel is more completely filled,  $\sigma$  increases. Recall that  $\sigma$  is defined from 0 to 1 where  $\sigma = 1$  corresponds to the flow being driven perfectly by the blades (azimuthal air velocity at the blade tip equals blade tip velocity) while  $\sigma = 0$  means that there is no azimuthal air flow (and therefore no flow whatsoever) for a nonzero blade velocity.

Thermal convection resistance,  $R$  is calculated by inserting (5.23) and (5.24) into (3.12).

$$R = [(1 - 7.2G + 4.5B - 0.55B/G)(0.32G + 2.4B - 0.035B/G) Re_\omega Pr \kappa r_t]^{-1} \quad (5.26)$$

This equation can be used to predict the thermal resistance of single layer heat sinks with a variety of geometries and speeds, as a function of  $G$  and  $B$ . The maximum error between (5.26) and the raw data is 28%, with most errors less than 15%; the mean error between (5.26) and the raw data was less than 0.02%, and the standard deviation is 11%. Eq. (5.26) is plotted in Fig. 5.6 a for particular conditions: the fluid is air,  $r_t = 5$  cm, and  $Re_\omega = 7.8 \times 10^4$ . For a given  $Re_\omega$  and  $r_t$ , thermal resistance is minimized in the range tested when both  $G$  and  $B$  are large. Large  $G$  and  $B$  allow higher flow rates and keep the thermal boundary layer thin. Increasing  $Re_\omega$  reduces thermal resistance by moving more air, but at the expense of an increased  $\dot{W}$ . Increasing  $r_t$  reduces thermal resistance by spreading the thermal power over a wider area, but at the expense of a larger footprint.

The pumping power,  $\dot{W}$ , is calculated by inserting (5.23) and (5.25) into (3.9).

$$\dot{W} = (0.11 - 0.96G - 3.5B + 0.54B/G)(0.32G + 2.4B - 0.035B/G)\rho\omega^3r_t^5 \quad (5.27)$$

This equation can be used to predict the pumping power of single layer heat sinks with a variety of geometries and speeds, as a function of  $G$  and  $B$ . The maximum error between



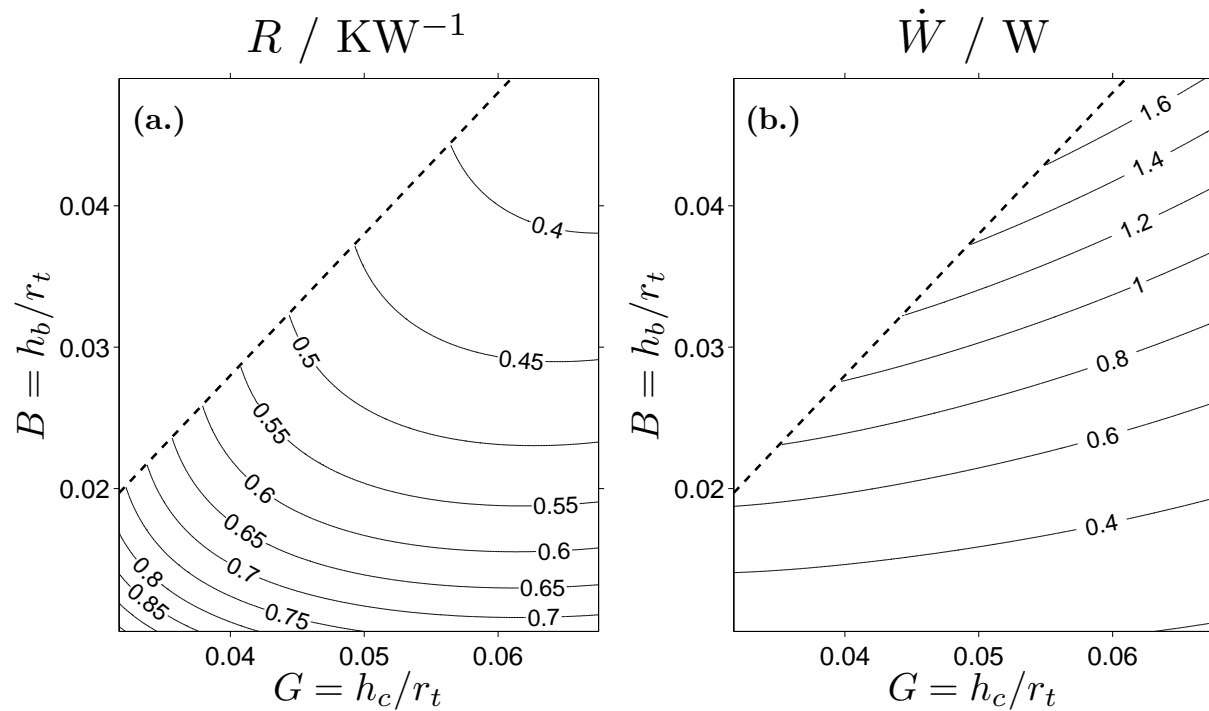


Figure 5.6: (a.) Contour plot of predicted air convection thermal resistance,  $R$ , for a single layer heat sink with  $r_t = 5$  cm, operating in air, with  $Re_\omega = 7.8 \times 10^4$  (a rotor speed of 5000 rpm). Isoclines have units of  $\text{KW}^{-1}$ .  $B$  is on the ordinate and  $G$  is on the abscissa. (b.) Contour plot of  $\dot{W}$ , isoclines have units of W.

(5.27) and the raw data is 30%, with most errors less than 20%; the mean error between (5.27) and the raw data was less than 0.9%, and the standard deviation is 13% (this analysis ignores one data point at a very low pumping power that could not be accurately measured). Eq. (5.27) is plotted in Fig. 5.6 b for the same conditions as Fig. 5.6 a. For a given  $Re_\omega$  and  $r_t$ ,  $\dot{W}$  decreases with higher  $G$  and lower  $B$ .  $\dot{W}$  is dependent on  $G$  because wider channels reduce the pressure losses on the walls, and  $\dot{W}$  is dependent on  $B$  because thinner blades drive less air flow at a given  $r_t$  and  $Re_\omega$ . Increasing  $Re_\omega$  strongly affects  $\dot{W}$  because  $\omega$  comes into (5.27) as the third power.  $\dot{W}$  increases at a very rapid rate with  $r_t$  due to the fifth power dependence in (5.27). Physically, this means that larger heat sinks trade off increased  $\dot{W}$  for reduced thermal resistance. As heat sink size increases, the increase in power consumption is much faster than the decrease in thermal resistance. This suggests that the performance is enhanced by using many small heat sinks distributed among various locations where thermal power is generated rather than using one large heat sink in a central location.

This tradeoff between pumping power and thermal resistance can be seen in Fig. 5.7, which plots the data in Fig. 5.6 a against the data in Fig. 5.6 b. The fluid in Fig. 5.7 is air and  $r_t = 5$  cm;  $f$  varies from 3000–7000 rpm.

The Pareto frontier of the performance of heat sinks are generally well suited to power law fits, sometimes requiring a constant offset. A fit curve of the Pareto frontier of Fig. 5.7 finds  $R$  as a function of  $\dot{W}$ .

$$R = 0.387\dot{W}^{-0.333} \quad (5.28)$$

for  $0.11 \text{ W} \leq \dot{W} \leq 1.4 \text{ W}$

This equation specifies the lowest possible thermal resistance that can be achieved for a given pumping power within the range given in (5.23). The Pareto optimal heat sink associated with (5.23) has  $G = 0.068$  and  $B = 0.023$ . Fortunately, these optimal values of  $G$  and  $B$  leave space for a considerable gap for clearance between the stator and the rotor. As can be seen in Fig. 5.7, the optimal performance is sensitive to  $G$ , but not very sensitive to  $B$ . This suggests that  $B$  can be varied with only a slight impact on the performance, while variations in  $G$  will cause significant changes in performance.  $G = 0.068$  is the largest value of  $G$  that was tested; even larger  $G$  will likely lead to designs that strictly dominate the Pareto efficient design described here. It should be noted however that Fig. 5.7 is for a fixed  $r_t$ , thus an increase in  $G$  implies an increase in overall heat sink volume. The total volume available to a heat sink is often restricted and thus making improvements to  $R$  by an increase in  $G$  may entail a tradeoff. In contrast to  $G$ , the value for  $B$  at which the optimal performance exists is not on the border of the parameter space, but within the parameter space. This suggests that  $B = 0.023$  successfully trades off the improved heat transfer created by having a thicker blade in a given channel (larger  $B$  for a given  $G$ ) which is created by the larger temperature gradient in the gap between the rotor and the stator versus the reduced pumping power requirements associated with having a lower  $B$  for a given  $G$ .

Each curve in Fig. 5.7 is parameterized by angular speed,  $f$ , which increases as the operating point moves to lower thermal resistances and higher pumping power. For example,

---

at an angular speed of  $f = 5000$  rpm, the Pareto optimal design has  $R = 0.43 \text{ KW}^{-1}$  and  $\dot{W} = 0.72 \text{ W}$ . The mass flow rate is  $4.9 \text{ g s}^{-1}$ , and the volume through which the air flows is  $35 \text{ cm}^3$ . Note that for a given  $G$ , an increasing  $B$  tends to move the operating regime to lower speeds because the air is being driven more effectively by the thicker blade. As has just been alluded to, all of the Pareto optimal solutions are for the same design, meaning that one design gives the optimal performance for any regime of pumping power.

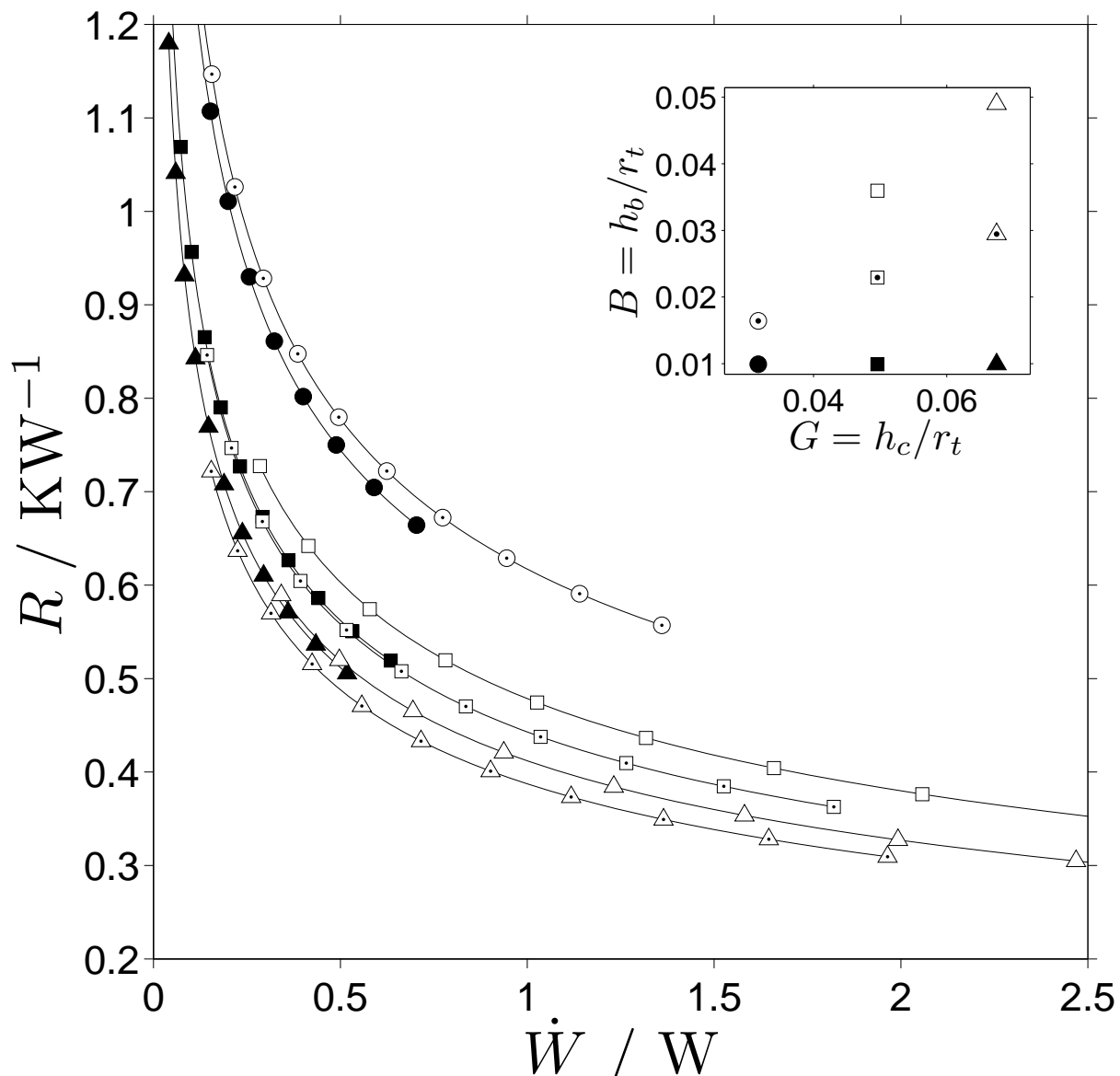


Figure 5.7: Plot comparing  $\dot{W}$  with  $R$  for single layer heat sink designs with  $r_t = 5$  cm. Curves are interpolated from Fig. 5.6. The inset figure is the legend showing the values of  $G$  and  $B$  for each design. The equation for the Pareto frontier of the data, marked with dotted triangles, is Eq. (5.28). The curves are plotted from 3000 to 7000 rpm, with markers at 400 rpm increments; parts of some curves are not shown.

# Chapter 6

## Multilayer Assembly

The next step in the process of producing a heat sink to meet the requirements listed in Sec. 1.2 is to create an assembly that generates air flow through multiple layers with the motor to be used on the final heat sink. Measurements of the air flow through this multilayer heat sink were done. This assembly also served to develop construction techniques and materials to be used in the final heat sink. This multilayer assembly, shown in drawings in Fig. 6.1 and in a photograph in Fig. 6.2, is a prototype of the final heat sink in every aspect but the heat pipe.

### 6.1 Design

This section gives an overview of the design of the multilayer assembly, the following section will discuss its construction in detail.

The assembly was designed to fit within a 4 inch cube; it is composed of an evaporator analog, four vertical rods, fourteen stator analogs, fifteen rotors, a shaft, two bearings, a top bearing support piece, a motor stator and a motor rotor as labeled in Fig. 6.1 b. The evaporator analog and stator analogs are solid stainless steel plates that represent the respective components of the heat pipe for the sake of testing the air flow in the heat sink. Likewise, the vertical rods in the current assembly are solid steel, but in the complete heat sink with the heat pipe, they will be hollow and allow transmission of vapor and liquid between the evaporator and stators. The vertical rods, evaporator analog, and bearing support were conventionally machined. The stator analogs were cut by water-jet.

Brazing was selected as the adhesion method for components that would be integrated into the heat pipe so as to maximize the fidelity of the assembly to the final heat sink. A jig (visible in Fig. 6.3, Fig. 6.4, and Fig. 6.5 i) was made to hold the evaporator analog, vertical rods, and stator analogs in the proper orientation with respect to each other to maximize the co-planarity of the stator analogs and evaporator analogs and ensure that the axis formed by the top and bottom bearings is orthogonal to the plane of the stator analogs. The evaporator analog, vertical rods, and stator analogs, are brazed together as in the final heat sink. All of the components, except the springs, mentioned later, that go into the brazing furnace are made of 403 stainless steel to prevent thermal expansion mismatch problems. The jig itself is shown in Fig. 6.3 and is composed of three pieces, a bottom piece that holds the evaporator analog and two vertical side pieces that hold the stator analogs and dummy bearing support.

The other components of the multilayer assembly are incorporated after the assembly has been removed from the jig after the brazing step. The assembly uses two bearings, one

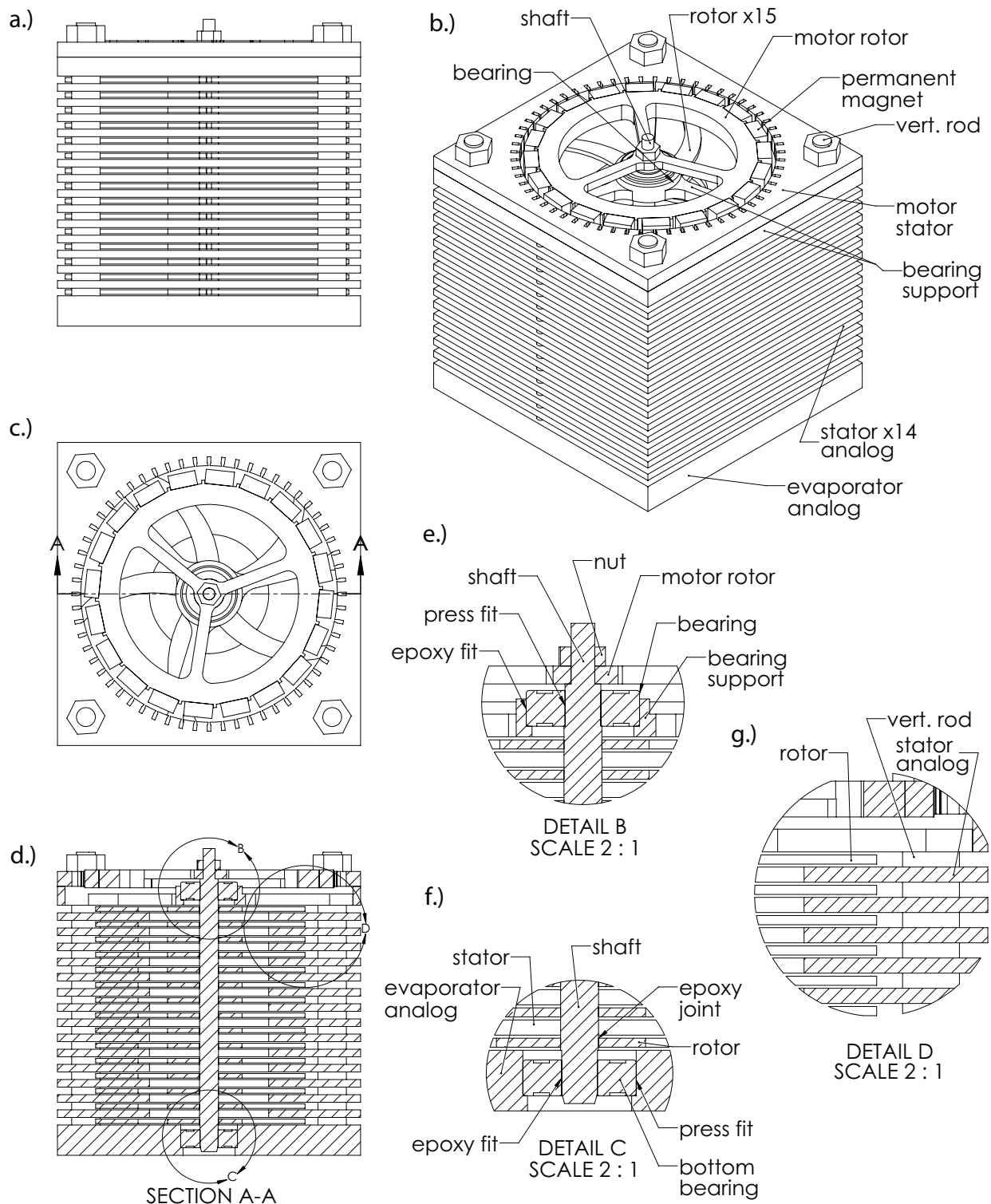


Figure 6.1: Drawing of multilayer assembly. **a.)** Side view. **b.)** Isometric view with labeled components. **c.)** Overhead view. **d.)** Cutaway view showing a cross section. **e.)** Detail view of top bearing and vicinity. The inner race is pressed onto the shaft and the outer race is epoxied to the bearing support. The motor rotor is fixed with a nut to the shaft. **f.)** Detail view of the bottom bearing. The rotors are fixed to the shaft with a ring of epoxy. The inner race is epoxied to the shaft and the outer race is pressed into the evaporator analog. The evaporator analog is counterbored all the way through to allow removal of the bottom bearing. **g.)** Detail view of flow channel; rotor, stator analog, and vertical rod are labeled.

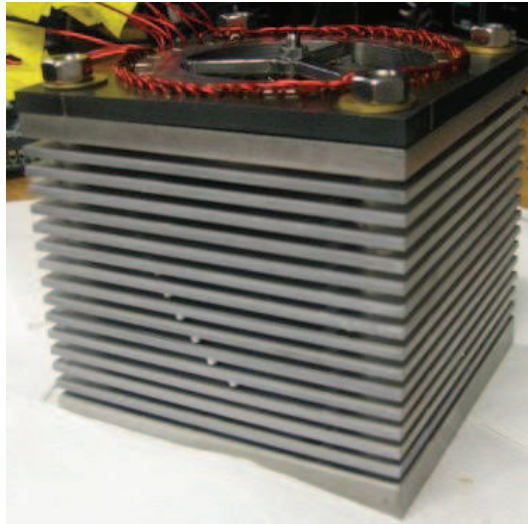


Figure 6.2: Completed multilayer assembly. Several blade tips are visible near the ends of the flow channel.

fixed into a hole at the bottom of the evaporator analog (Fig. 6.1 f), the other fixed in the top bearing support (Fig. 6.1 e). Self-aligning, double-row, oiled, radial ball bearings are used. The self-aligning nature of the bearings keeps the power loss in the bearings low even if the bearings are not centered such that the axis of the shaft's rotation is orthogonal to the planes of the bearings. The bearings support the shaft (Fig. 6.1 d), which is machined from highly straight driveshaft stainless steel stock. The rotors are epoxied to the shaft (Fig. 6.1 f). The motor stator and motor rotor are fixed to the vertical rods and shaft, respectively (Fig. 6.1 b and e). Power electronics are used to control the motor.

The rotors are made of 6061-T6 aluminum and laser cut according to the CAD pattern shown in Fig. 5.1 c. The rotors are then ground from 0.080 to 0.060 inches thick via double-disk grinding to achieve better than 0.001 inch flatness across the 4 inch diameter. The stator analogs are spaced apart such that the height of the flow channel is 0.100 inches, giving a nominal clearance between the rotors and the stator analogs of 0.020 inches. These dimensions were chosen because they had been studied in the single layer experiment and because they offered enough clearance between the rotor and stator analogs to be manufacturable.

## 6.2 Construction

The construction process of the multilayer assembly is shown in Fig. 6.4 and 6.5. The process begins by cleaning all components that will go into the brazing furnace. Components to be brazed are cleaned with a mixture of hydrofluoric acid and nitric acid, other components are cleaned with isopropanol and acetone.

After cleaning, the evaporator analog is placed in the bottom of the jig. The evaporator analog is registered against two registration points on the side and two in the back of the jig, as shown in Fig. 6.3 b and Fig. 6.4 a. The vertical pieces of the jig are then assembled and braze rings are placed in the proper location on the evaporator analog, Fig. 6.4 b, and stator analogs are slid into the side of the jig one by one, adding braze rings above each stator analog, Fig. 6.4 c and d.

The vertical rods are then inserted through the braze rings, and the holes in the corners of the stator analogs and the evaporator analog, Fig. 6.4 e–g. The dummy bearing support is placed on top of the vertical rods. The dummy bearing support is likewise registered against two registration points on the side and two in the back of the jig. Inconel leaf springs are inserted into slots on the front and left sides of the jig and on the top and bottom to register the evaporator analog and the dummy bearing support to the back right corner, Fig. 6.4 h. Inconel was chosen for its ability to maintain its strength at the high temperatures of the furnace. The jig and assembly are then placed in a vacuum furnace and brazed.

After brazing, the multilayer assembly is removed from the jig and the dummy bearing support is removed, Fig. 6.5 i. Next, The bottom bearing is installed in the evaporator analog from above and the actual bearing support is mounted in place of the dummy bearing support. Epoxy is applied to the inner race of the bottom bearing and rotors are slid in the sides of the flow channels starting with the bottom layer and working upwards. Epoxy is applied in a ring around the center hole of each rotor as each rotor is placed in the side. The shaft, with the top bearing already press fitted onto the shaft, is then passed through the rotors and inner race of the bottom bearing. The top bearing is epoxied to the bearing support.

Before the epoxy sets, the rotors are shimmed to define their axial position to be in the middle of the flow channel, Fig. 6.5 j and k. The blades are then rotated with respect to each other to reduce the fluidic resistance in the core of the device, Fig. 6.5 l. The epoxy cures and the shims are removed, Fig. 6.5 m. Next the motor stator is mounted to the vertical rods and the motor rotor is mounted to the shaft. The motor is controlled by commercially available hardware and software, Fig. 6.5 n–p.

## 6.3 Performance

The multilayer assembly has been spun by the motor at up to 4450 rpm. The rotors do not seem to strike the stator surfaces, any mechanical noise generated by the heat sink is thought to be due to the bearings. The expected mass flow rate for a single layer heat sink with the same blade height and channel height multiplied by the number of rotors in the multilayer assembly gives the mass flow rate that would exist if the effect of adding layers to the single layer heat sink is negligible. This mass flow rate is  $81 \text{ gs}^{-1}$ . Several tests of the mass flow rate through the multilayer assembly were attempted, including bag inflation tests and scans by hot-wire anemometer, giving preliminary results. The bag inflation tests gave mass flow rates on the order of  $10 \text{ gs}^{-1}$ . Hot-wire anemometer tests were done by



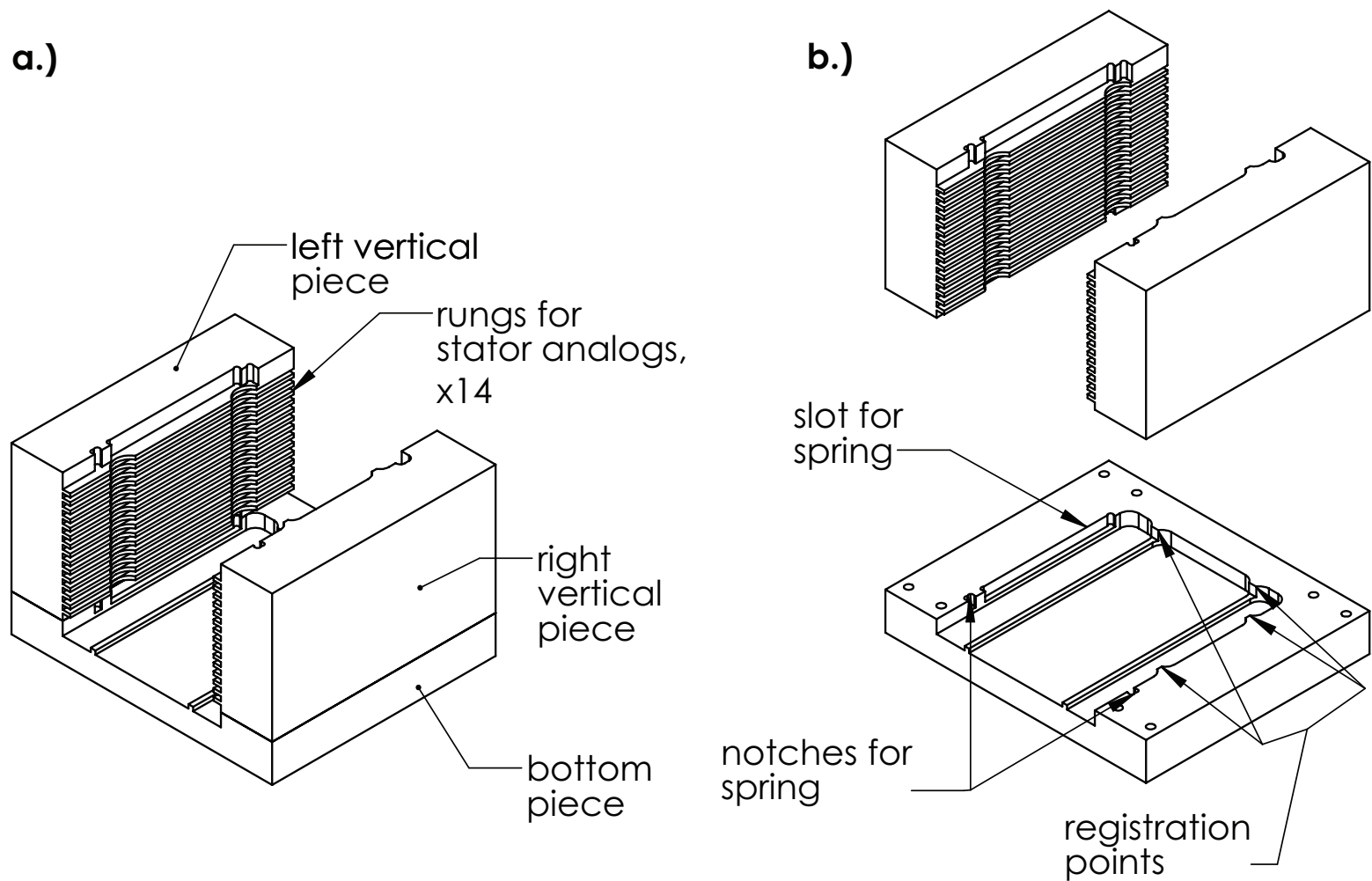


Figure 6.3: Drawing of jig for multilayer assembly. **a.)** Assembled jig with three pieces identified. Rungs on vertical pieces hold the stator analogs in place during brazing. **b.)** Exploded view with registration points for the evaporator analog and notches and slot for the bottom springs identified.

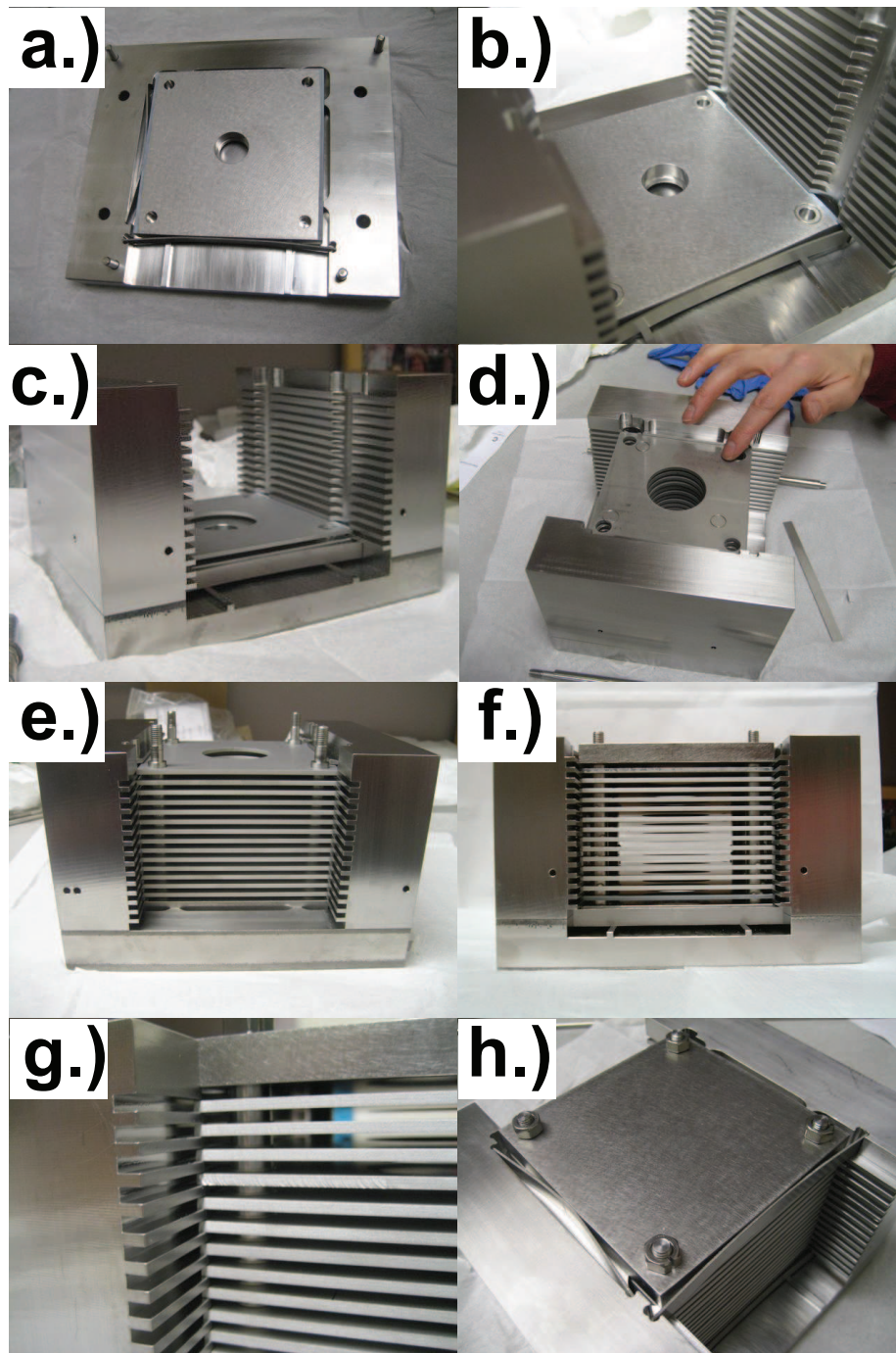


Figure 6.4: Multilayer assembly construction process. **a.)** Bottom jig piece with evaporator analog; side registration points visible. **b.)** Fully assembled jig with braze rings on evaporator analog **c.)** Fully assembled jig with first stator analog slid in the side of the jig **d.)** Braze rings being placed on last stator analog **e.)** Vertical rods inserted through stator analog and evaporator analog holes. Back registration points visible **f.)** Dummy bearing support mounted. Support rails visible underneath evaporator analog. **g.)** Close-up view of jig rungs and stator analogs **h.)** Top view of dummy bearing support and inconel springs.

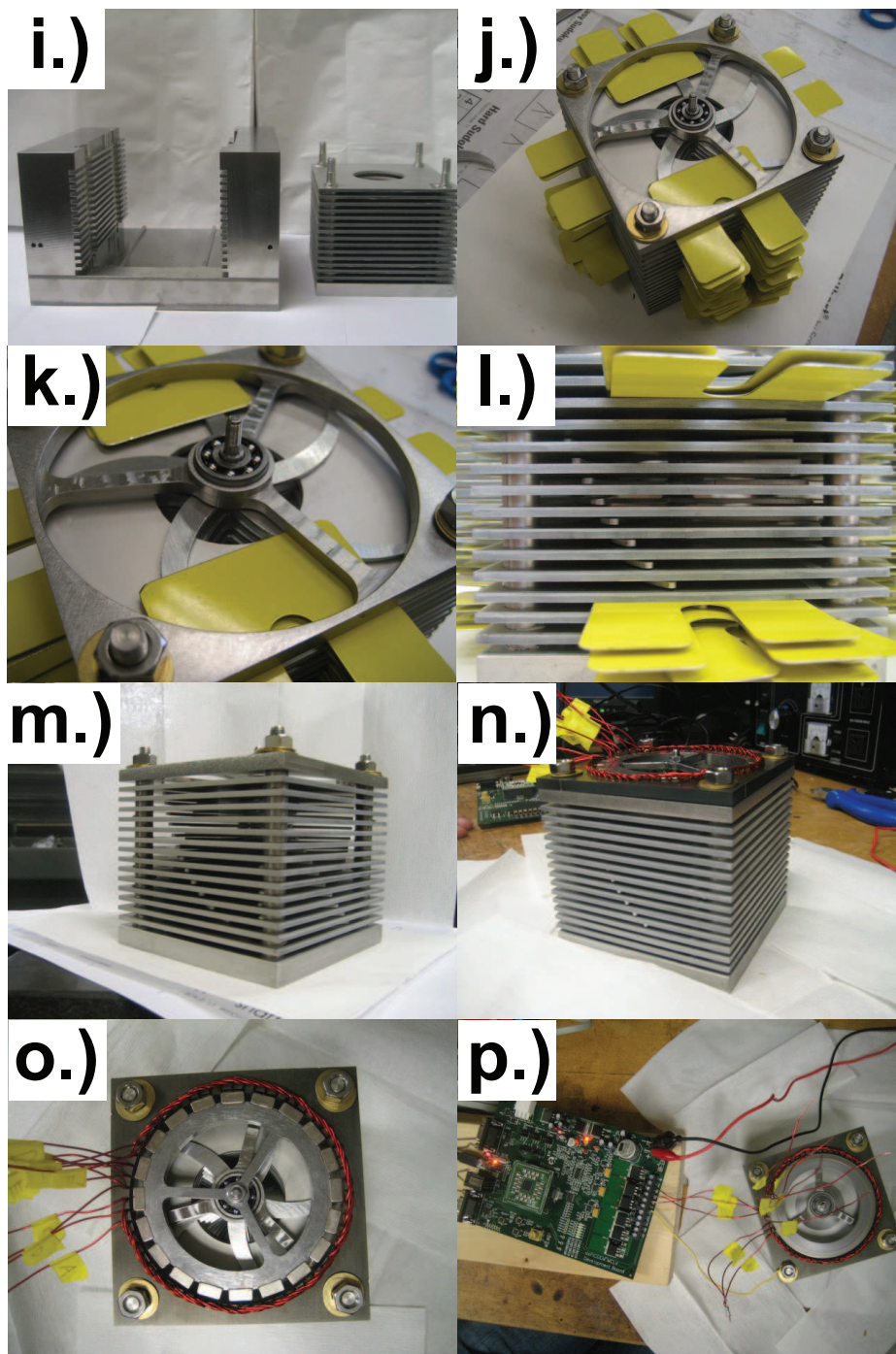


Figure 6.5: Multilayer assembly construction process, continued. **i.)** After brazing the assembly is removed from the jig, the dummy bearing support is removed **j.)** Shimmed rotors with curing epoxy. **k.)** Close-up view of top bearing, bearing support, rotor, stator, and shims **l.)** Side view of shimmed and staggered rotors **m.)** Epoxy cured, shims removed, rotors spin freely **n.)** Motor installed; gunmetal colored component is the laminated motor stator, red wires are the windings **o.)** Overhead view of motor; motor rotor with permanent magnets mounted to shaft **p.)** Motor spinning rotors, controlled by power electronics.

---

scanning the anemometer along the exit of the multilayer assembly from the top to the bottom at several  $x$  locations. The wire was oriented to face the exit plane. The data was then processed to determine the average cooling velocities experienced by the probe. These were then integrated over the exit plane giving a predicted mass flow rate. Similarly, the flow into the multilayer assembly was scanned. The mass flow rate at the exit was found to be  $40 \text{ g s}^{-1}$  and at the inlet it was found to be  $6 \text{ g s}^{-1}$ . This discrepancy can be explained by the complex nature of the flow through this type of device. Scans were not done at multiple orientations to allow the velocity components to be separated, thus causing the mass flow rate at the exit to overestimate the flow rate. Also, as the probe scans across the exit, it scans past alternating flow channels and stator analogs, where there are complex changes in flow direction and recirculation.

It was concluded that the flow rate through the multilayer assembly is significantly less than the flow rate for a single layer heat sink with similar geometry, multiplied by the number of rotors. This is thought to be due to the large pressure drops at the inlet to the heat sink that are induced by the accelerating the air from the ambient atmosphere. These pressure drops force the multilayer assembly to pump air against an adverse pressure gradient, reducing the flow rate it can output for a given pumping power. Future work will focus on ways to characterize and reduce this pressure loss so as to increase the flow rates of the multilayer heat sink sufficiently to achieve the performance goals for the final, multilayer heat sink.

# Chapter 7

## Comparisons

In this work, the heat transfer and fluid mechanics relevant to a high aspect ratio air cooled heat sink with a single rotor interdigitated between heat transfer surfaces has been studied via models based on correlations from the literature, another set of models created using computational fluid dynamics, and an experiment. The results of these models will now be compared.

Fig. 7.1 shows the results of  $R$  versus  $\dot{W}$  for the correlation based models, the CFD models, and the experiment. The correlation based model and the experiment have data taken under comparable conditions. These two datasets are plotted from 3000 to 7000 rpm for three different values of  $h_c$  ([1.6, 2.5, 3.4] mm), with all other parameters fixed to the same values:  $r_i = 20$  mm,  $r_t = 50$  mm,  $h_b = [1.2, 1.8, 2.5]$  mm, 5 blades per rotor, and a blade sweep at the tip of  $-45^\circ$ . The data from the correlation based model and the data from the experiment which produce their respective curves are discussed in Sec. 2.12 and Sec. 5.6, respectively. Additionally, the optimal design (Eq. (5.28)) found in the experiment is plotted as a solid line. The CFD data is somewhat different: several geometries were tested at only a few different speeds, thus the data is plotted as the Pareto optimal curve of this dataset which includes several different geometries, this curve is Eq. 4.1 and the data is depicted in Fig. 4.3.

Fig. 7.1 shows that both the correlation based model and the CFD model underpredict the experimental behavior, although the CFD is closer. The reasons for this discrepancy are further discussed in the two following sections.

### 7.1 Correlation based model versus experiment

The experimental data shows that as  $h_c$  increases, the performance improves. This is because, for a given pumping power, the heat sink is able to generate more flow rate with a wider flow channel, as seen in Fig. 7.2. However, the correlation based model, has worse performance as  $h_c$  increases even though it also has an increasing mass flow rate as  $h_c$  increases. The difference between the experiment and the model is that the experiment has its exchanger effectiveness nearly constant with increasing  $h_c$  but increasing with increasing  $h_b$ . (c.f. Eq. (5.24)) while the exchanger effectiveness of the correlation based model decreases with increasing  $h_c$ . This decrease in  $\varepsilon$  is due to the formulation of the model; developing flow Nusselt correlations were used in the flow channel to calculate the heat transfer, but the flow was found to not fully develop before exiting the heat sink. Thus the correlation based model predicts that, as the flow channel height increases, the core of unheated fluid will grow and performance will suffer. However, the opposing

behavior of the experimental results suggest that the flow is, in fact, thoroughly mixed by the rotating blades and thus exchanger effectiveness is not much affected by changes in the hydraulic diameter and correlations assuming flow development are irrelevant to this type of flow. Since the Nusselt correlations available in the literature do not accurately capture the behavior of this flow, future models of similar flows should avoid such correlations.

Returning to Fig. 7.2 and the fluid mechanics of the flow; it can be seen that the correlation based model shows similar behavior, in terms of mass flow rate, to the experiment and that for at least these cases, it provides reasonably accurate results (in terms of mass flow rate) for low  $h_c$ . It should be noted however that Fig. 7.2 is plotted for angular speeds from 3000 to 7000 rpm and that the curves are again parametrized by the angular speed of the rotor. The shift in the curves from the experimental data to the model data means that the model predicts a higher pumping power for a given angular speed than the experiment shows.

The differences between the mass flow rates of the model and the experiment in Fig. 7.2 do not account for the large difference in thermal resistance between the models (for a fixed pumping power). This difference in thermal resistance is approximately a factor of 4. Again, this suggests that the developing flow Nusselt correlations used in the correlation based model do not adequately capture the heat transfer in the actual system.

## 7.2 CFD versus experiment

The CFD data presented in Fig. 7.1 is for various geometries, but there are two CFD models of the same geometry at different angular speeds that have their geometry comparable to the experimental data. These datasets are compared in Fig. 7.3.

The CFD data is available at 4580 and 5060 rpm and plotted as circles, the experimental data is plotted from 3000 to 7000 rpm as a solid curve and at 4580 and 5060 rpm as triangles.  $r_i = 20$  mm,  $r_t = 50$  mm,  $h_c = 2.2$  mm,  $h_b = 1.6$  mm, and a blade sweep at the tip of  $-45^\circ$ . The only discrepancy between these CFD models and the experimental data is that the CFD has 9 blades on the rotor while the experiment has 5; but, as was discussed earlier in the chapter on the CFD models, the number of blades per rotor has been found to have little effect on the performance of the system.

The results show that the performance of the CFD model does indeed underpredict the performance of the experimental results. For a fixed pumping power, the thermal resistance of the CFD model is about 45% higher than the experiment. The inset of Fig. 7.1 gives some indication why: the mass flow rate of the CFD model is also less than the experimental results. This suggests that some element or elements of the CFD model does not completely capture the fluid mechanics (and possibly the heat transfer) of the physical system. Looking more closely at the inset, it can be seen that the CFD model predicts mass flow rate rather accurately for a given rotor angular speed, but rather poorly for a given pumping power. This suggests that the CFD model is rather accurately predicting the flow coefficient,  $C_f$ , but is not accurately predicting the slip factor,  $\sigma$ . Since the pumping power is overestimated by the CFD model (as seen in Fig. 7.1 in both the

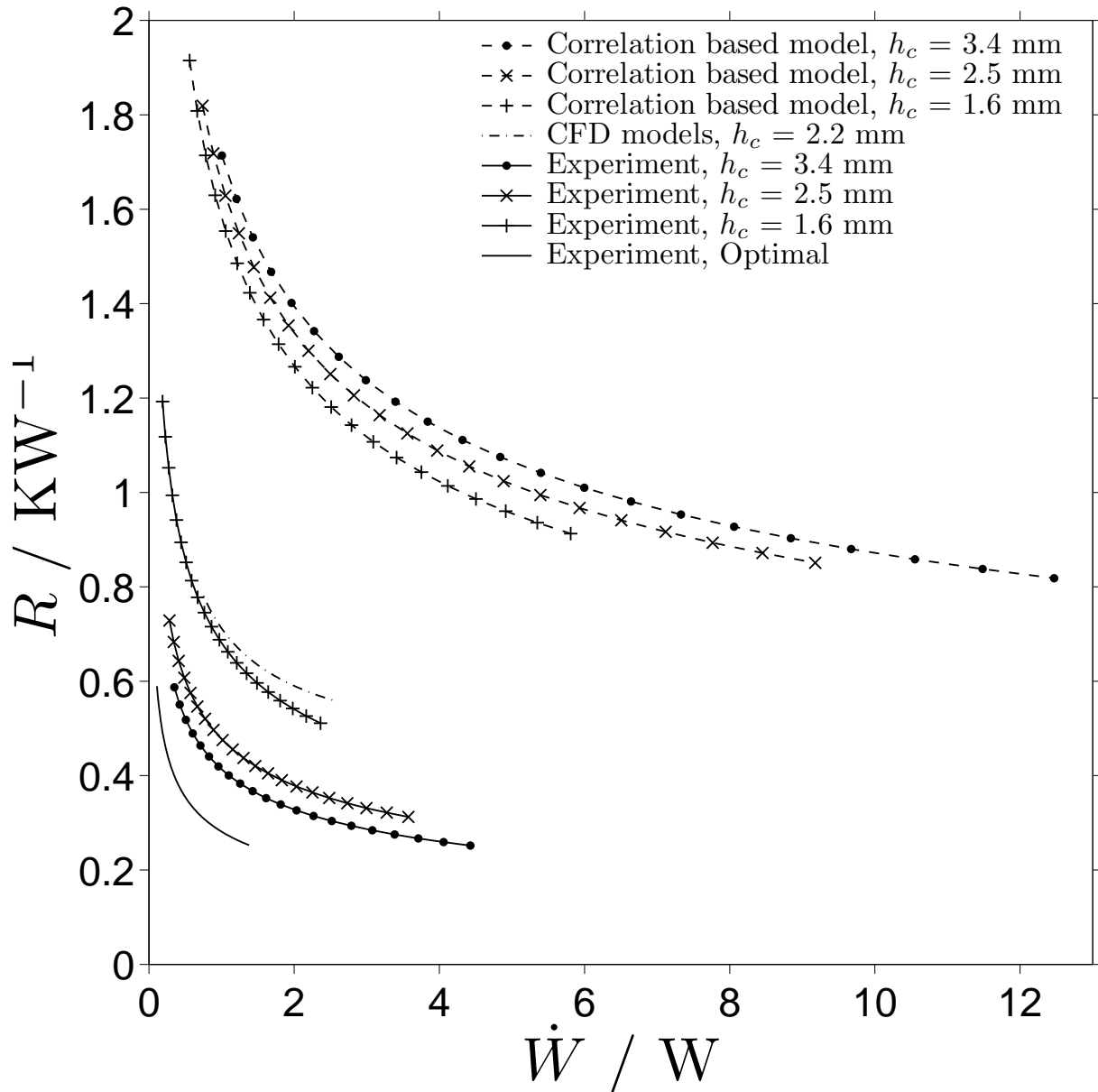


Figure 7.1: Compiled plots of thermal convection resistance,  $R$ , versus pumping power,  $\dot{W}$ , for a single layer heat sink for the correlation based model, CFD model, and experimental results.

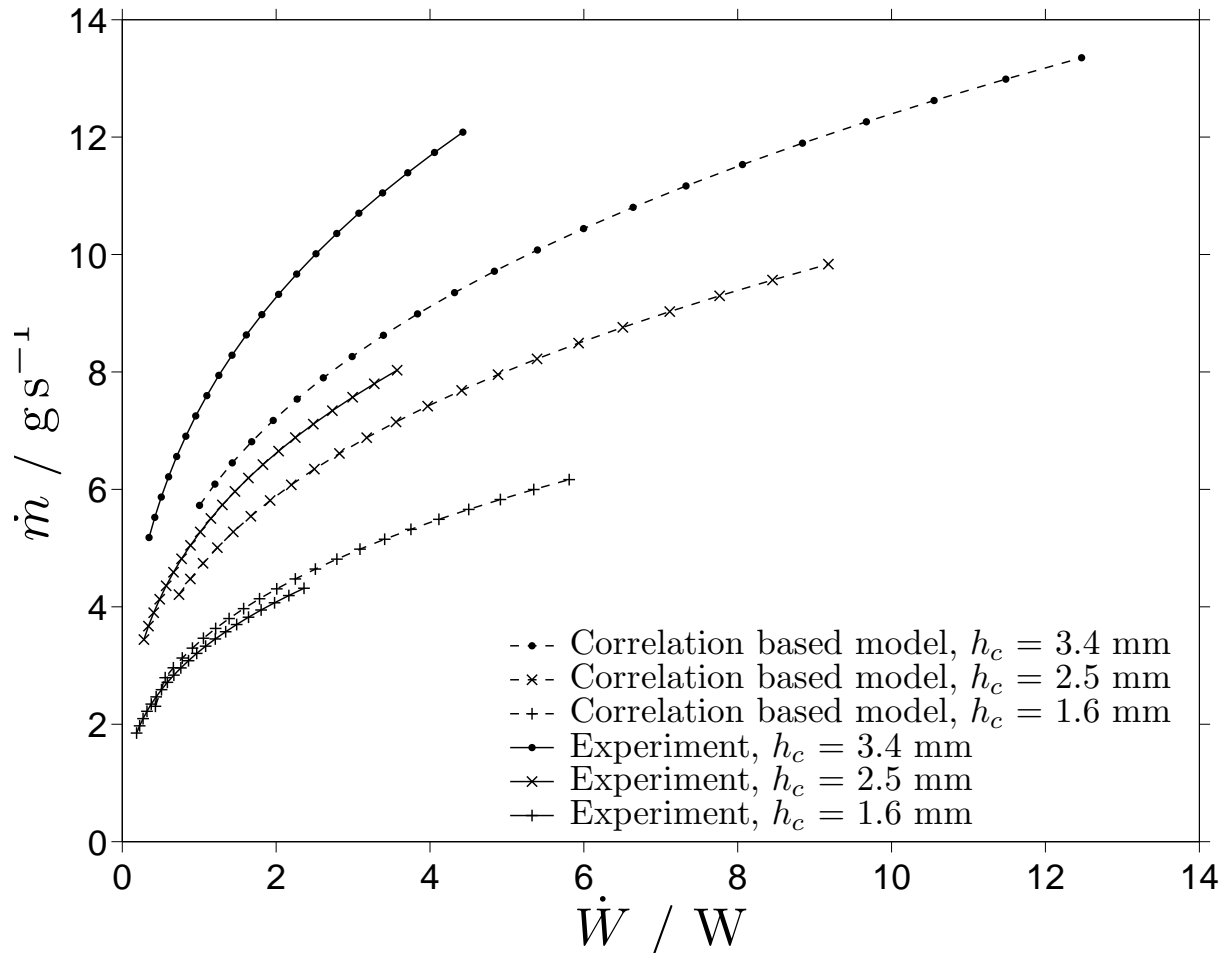


Figure 7.2: Compiled plots of mass flow rate,  $\dot{m}$ , versus pumping power,  $\dot{W}$ , for a single layer heat sink for the correlation based model and experimental results.



---

main figure and the inset), this indicates that the CFD model predicts that the tangential air velocity in the rotor channel is higher than it truly is.

Possible issues with the CFD model include the turbulence model, the steady nature of the model, the cell size, the inlet and outlet boundary conditions, and the reduced heat transfer surface area. The turbulence model used was a simple one-equation turbulence model which may not accurately model the high turbulence intensity flow; this flow may be so turbulent that the steady model that was used does not account for significant unsteady (time dependent) features in the flow on the time scale of the reduced frequency of the blades. It is also possible that the size of the cells in the model was not sufficiently dense to capture the high gradients in temperature and momentum at the interfaces between the blades and the air and the stators and the air. For simplicity, the model enforced a jet inflow and jet outflow, although a larger model with a plenum would allow more accurate boundary conditions. Finally, the heat transfer surface area of the CFD model does not include the area in the corners of the heat sink. Although this surface area is also not modeled in terms of the frictional losses, the net effect of not accounting for these corners may also create some of the discrepancy seen in Fig. 7.1.

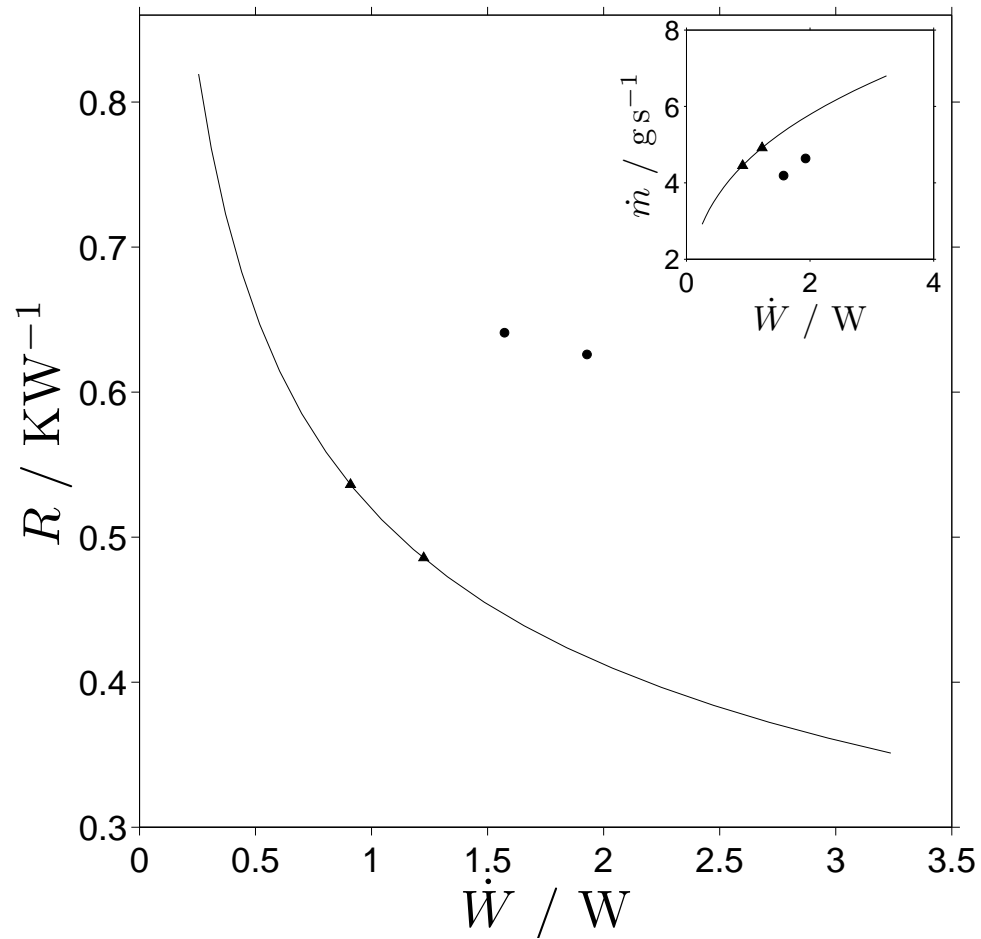


Figure 7.3: Comparison of performance of CFD versus experiment. Circles represent two CFD models of the same geometry at two different angular speeds, the solid curve represents the experimental data for a similar geometry, with triangles marking the same experimental angular speeds as the CFD data. Inset is the mass flow rate as a function of pumping power for the same datasets.

# Chapter 8

## Conclusion and Future Work

### 8.1 Future Work

Future work will study the flow rate through the multilayer assembly and attempt to improve it in the complete multilayer heat sink. The primary difference between the multilayer heat sink and the single layer heat sink is that the flow through all layers of the multilayer heat sink must pass through the inlet, whereas in the single layer heat sink only the flow through the single layer passes through the inlet. This increased flow rate through the inlet of the multilayer causes a pressure drop associated with the acceleration of the air from ambient into the inlet of the multilayer heat sink; this pressure drop will be significant and may be the dominant pressure drop in the system. This increased pressure drop will reduce the flow rate below what would be expected from the number of layers in the multilayer heat sink times the flow rate through the single layer heat sink. Both the pumping power and the heat transfer through the multilayer heat sink will need to be calculated to allow predictions of multilayer heat sink performance before construction. After construction, these performance parameters must be measured.

The pumping power for a multilayer heat sink must be both measured for an already constructed device, and predicted mathematically. Experimentally, the shaft power output by the motor that drives the multilayer assembly can be calculated by the program that drives the motor. The motor has no knowledge of what the shaft power is used for and thus it cannot calculate the pumping power of the rotors, but it can calculate the shaft power output of the motor. The shaft power is the pumping power plus the mechanical power losses (primarily in the bearings). This shaft power is more relevant to the performance of the complete heat sink than the pumping power, and it can be found without testing the bearing power consumption with and without the rotors. For a complete characterization of the heat sink, the input electrical power can be used instead. This power consumption can be measured with the current multilayer assembly, but if the power consumption for other geometries is desired, Eqn. (5.27) may be useful. This equation has been developed from data for the single layer experiments, but it may be used as a component in a fluidic circuit with multiple resistive and pumping elements to predict the power consumption. It should be noted that the fluidic resistances of the multilayer heat sink will be larger than for the single layer heat sink because of the faster velocities and therefore lower pressures at the inlet.

The thermal resistance of the system is more complex to measure. The multilayer assembly, as constructed, does not include resistive heaters in the stator analogs, although these could be incorporated into future versions. A Biot number calculation (the ratio

of convective to conductive thermal resistance) should be done to determine if the stator analog (with a given thickness and thermal conductivity) is able to evenly spread the heat produced by resistive heaters. When the heat pipe component of the heat sink is built, this can be used as the heat source for the stator walls. The thermal resistance can either be calculated as in Eqn. 3.10 or as Eqn. 3.11; the former may be used if the following are known: thermal power (with losses accounted for), the ambient temperature, and the stator temperature. The latter may be used if the mass flow rate, the bulk temperature of the fluid at the exit, the ambient temperature, and the stator temperature are known. But before the experimental heat transfer for the multilayer heat sink is measured, it will need to be designed. For this, Eqn. 5.26 will hopefully prove suitable. Eqn. 5.26 was calculated for the flow channel in the single layer experiment, but the heat transfer in the heat sink is primarily in the flow channels. These thermal resistors can be arrayed in parallel based on the number of stators available. It should be noted that Eqn. 5.26 was correlated with the bottom stator analog as a 4 inch by 4 inch square with no central hole, which gives it more surface area than a typical stator, which has holes through both sides.

Calculations of the behavior of a multilayer sink should include both fluid mechanics and heat transfer so that efforts to improve mass flow are done for the sake of improving the heat transfer and not simply for its own sake.

## 8.2 Conclusion

This work has described a novel heat sink design and studied its air-side fluid mechanics and heat transfer. The analytical underpinnings of forced convection heat sinks are explored, generating a nondimensionalization that has been coupled with experimental data to allow predictions of air convection thermal resistance and pumping power for a range of air-cooled heat sinks. Pareto optimal designs are determined in a specified range.

Heat sinks of this novel type have significantly improved thermal resistance and pumping power in comparison to currently available air-cooled heat sinks. This improved performance is created by the interdigitation of the fan within the heat transfer surfaces of the heat sink. Interdigitation allows the thermal boundary layer to be kept very thin and also allows air to be driven smoothly through the heat sink. In contrast, classic air-cooled heat sinks have a single fan forcing air toward many fins. This situation creates many stagnation points and high pressure loss and causes the thermal boundary layer to develop only at the beginning of the fins.

A design is presented for a heat sink with a convection thermal resistance of  $R = 0.43 \text{ KW}^{-1}$  and a pumping power of  $\dot{W} = 0.72 \text{ W}$  at an angular speed of  $f = 5000 \text{ rpm}$ . The mass flow rate is  $4.9 \text{ g s}^{-1}$ , and the volume through which air flows is  $35 \text{ cm}^3$ .

# Appendix A

## Blade Shape

The blade begins at the shaft,  $r_s$ , and goes out to  $r_t$ . The angle of the camber line of the blade in radians is defined as

$$\beta_b(r) = \left( \beta_b(r_t) - \beta_b(r_s) \right) \left( \frac{r - r_s}{r_t - r_s} \right)^{w.t.} \quad (\text{A.1})$$

The camber line is drawn following this angle up until a predetermined cutoff radius,  $r_{\text{cut}}$  at which the camber line ends and the trailing edge is terminated with a circular arc. The length of the blade is

$$l_b = l_{cr} + r_{\text{cut}} \quad (\text{A.2})$$

Where  $l_{cr}$  is the camber line length as determined by integrating along (A.1). The length of camber line between a point on  $r$  and the next point on  $r$  is found from (A.1) and is named  $l_{b_r}(r)$ .

Define  $l_{\text{max}} = l_{cr}/NACA_{\text{cut}}$  as the hypothetical length of the blade profile if it were not terminated with the trailing edge circular arc. Also,  $l^* = r_t/l_{\text{max}}$ , the normalized length.

Define  $l_{\text{max}}$  as the hypothetical length of the blade profile if it were not terminated with the trailing edge circular arc. Also,  $l^* = r_t/l_{\text{max}}$ , the normalized length. Now the shape of the blade is created; only the back segment of the NACA profile is used, which is the region in which the blade is tapering down, which begins 29% of the way along the chord line of the normalized profile. This normalized blade profile is

$$\begin{aligned} Th(l^*) = 5l_{\text{max}}NACA_N \left[ 0.2969(.71l^* + .29)^{0.5} - 0.126(.71l^* + .29) \right. \\ \left. - 0.3537(.71l^* + .29)^2 + 0.2843(.71l^* + .29)^3 \right. \\ \left. - 0.1015(.71l^* + .29)^4 \right] \quad (\text{A.3}) \end{aligned}$$

where  $NACA_N$  is the last 2 digits of the desired NACA 4-digit profile. This is specified by the user to determine the blade width,  $w_b$ .  $Th$  is then applied to the camber line, defining the thickness of the blade. The locations of the points defining the blade shape are stored in a data file that can be uploaded to a computer aided design (CAD) program. The shape of the final blades is shown in Fig. 2.2.

# Appendix B

## Inflow Heat Transfer

Sec. 5.4.1 discusses the various mechanisms through which heat may be lost from the experiment other than the desired path through the stator analogs into the air that is driven through the heat sink by the rotor. One of these mechanisms is via conduction through the top insulation and into the air passing over the top surface, as seen in Fig. B.1. This heat is then sunk to the air via convection; a calculation of the relative significance of buoyant convection versus forced convection due to the air flow being pulled into the experimental apparatus gives the Richardson number,

$$Ri = \frac{g\beta(T_{\text{top}} - T_{\text{amb}})L}{v_{\text{top}}} \quad (\text{B.1})$$

where  $g$  and  $\beta$  are as defined for previous  $Ri$  calculations,  $T_{\text{top}}$  and  $T_{\text{amb}}$  are the temperatures of the top surface of the top piece of thermal insulation and the ambient, respectively,  $L$  is the length of a side of the heat sink and  $v_{\text{top}}$  is determined as a shell balance of the velocity field for an average position on the top surface of the insulation.

$$\pi r_i^2 v_{\text{inlet}} = 2\pi \left( \frac{r_i + r_t}{2} \right)^2 v_{\text{top}} \quad (\text{B.2})$$

where  $v_{\text{inlet}}$  is the inlet velocity for a known flow rate and  $v_{\text{top}}$  is the bulk velocity through a hemispherical shell centered around the inlet at  $(r_i + r_t)/2$ .

$Ri$  will be a function of the volumetric flow rate through the heat sink, where increased flow rate will cause forced convection to be more significant, denoted by a lower  $Ri$ . The highest flow rate tested,  $13.3 \text{ g s}^{-1}$ , which corresponds to an inlet Reynolds number (defined below),  $Re_{\text{inlet}}$  of 900, had  $Ri = 0.007$ , which indicates that the heat transfer is dominated by the forced convection due to the inlet flow. The lowest flow rate tested,  $1.1 \text{ g s}^{-1}$ , which corresponds to  $Re_{\text{inlet}} = 1.1 \times 10^4$ , had  $Ri = 5.8$ , which indicates that the convection is almost entirely buoyant convection.  $Ri = 1$  occurs for a mass flow rate of approximately  $2 \text{ g/s}$  and  $Re_{\text{inlet}} = 1700$ .  $Ri = 0.2$ , as reasonable boundary between the mixed convection and forced convection regimes, occurs for a mass flow rate of approximately  $4.0 \text{ g/s}$  and  $Re_{\text{inlet}} = 3300$ . Thus the flow rates pertinent to this problem correspond to flow regimes ranging from entirely forced convection to almost entirely buoyant convection. However, most of the range of  $Re_{\text{inlet}}$  tested correspond to the mixed convection and forced convection regime, as can be seen in Fig. B. The Reynolds number of the flow entering the inlet,  $Re_{\text{inlet}}$ , is

$$Re_{\text{inlet}} = \frac{2\rho v_y(j=0)r_i}{\mu} \quad (\text{B.3})$$

which is the Reynolds number associated with the flow through the circular inlet hole. This Reynolds number characterizes the flow across the top insulation surface of the experiment.

Moving on to the experimental data, the thermal power conducting through the top insulation piece,  $\dot{Q}_{\text{top}}$ , is known because all of the requisite information about the thermal insulation piece is known: the temperature of both sides, the physical dimensions, and the thermal conductivity. Now that  $\dot{Q}_{\text{top}}$  is known, the heat transfer coefficient of this convection is

$$h_{\text{top}} = \frac{\dot{Q}_{\text{top}}}{A_{\text{top}}(T_{\text{top}} - T_{\text{amb}})} \quad (\text{B.4})$$

The Nusselt number for this inlet flow with characteristic length  $L$  can be calculated from experimental data as

$$Nu_L = \frac{h_{\text{top}}\kappa}{L} \quad (\text{B.5})$$

This Nusselt number is physically determined by the amount of inflow into the heat sink, the ratio of viscous to thermal diffusion, and the ratio of inlet radius to the radius of the blade tip (which is equal to half the side length),  $\mathcal{I}$ . Thus  $Nu_L$  is expected to be a function of Reynolds number, Prandtl number, and  $\mathcal{I}$  of the inlet flow. Air ( $Pr = 0.7$ ) is the only fluid tested, and  $\mathcal{I}$  is set equal to 0.4. A Rayleigh number would be an appropriate variable for a correlation in a buoyant flow; however since the flow is primarily forced and mixed, the Reynolds number is used. Thus,  $Nu_L$  is only explored as a function of  $Re_{\text{inlet}}$ . The  $Nu_L$  data is plotted in Fig. B, along with a power law fit to the data. As shown in the plot this correlation is:

$$\begin{aligned} Nu_L &= 0.49Re_{\text{inlet}}^{0.27} + 1.2 \\ &\text{for } 900 < Re_i < 1.1 \times 10^4 \end{aligned} \quad (\text{B.6})$$

Note that (B.6) tends to 1.2 as  $Re_{\text{inlet}}$  goes to zero, which is close to the value of 1 that will occur for pure conduction.  $Nu_L$  is positively correlated with  $Re_i$  because increased flow rates generate more convection. Also, the data does not show any clearly identifiable transitions in the flow regime, suggesting that forced convection dominates over buoyant convection in this regime and that the flow remains turbulent within this range of Reynolds numbers. Further research into this problem of a heated, square plate facing upward with an inlet flow through a hole in the center of the plate, could develop other correlations for different geometries (varying  $\mathcal{I}$ ), different fluids, (varying  $Pr$ ), and different flow regimes.

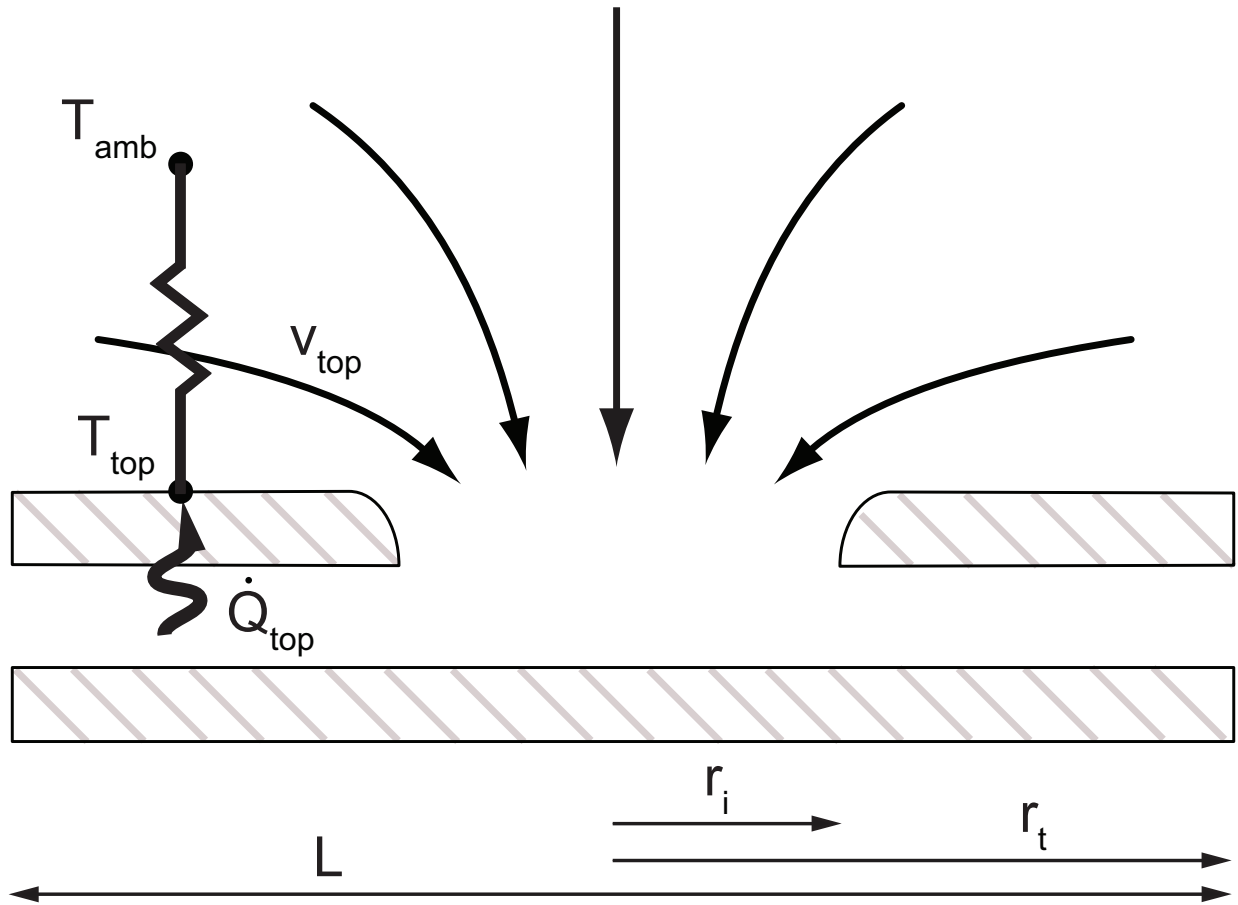


Figure B.1: Cross section of experimental setup, showing air flow at the inlet. Air flowing into the experiment convects across the warm top surface of the experiment, causing convective heat transfer into the air.



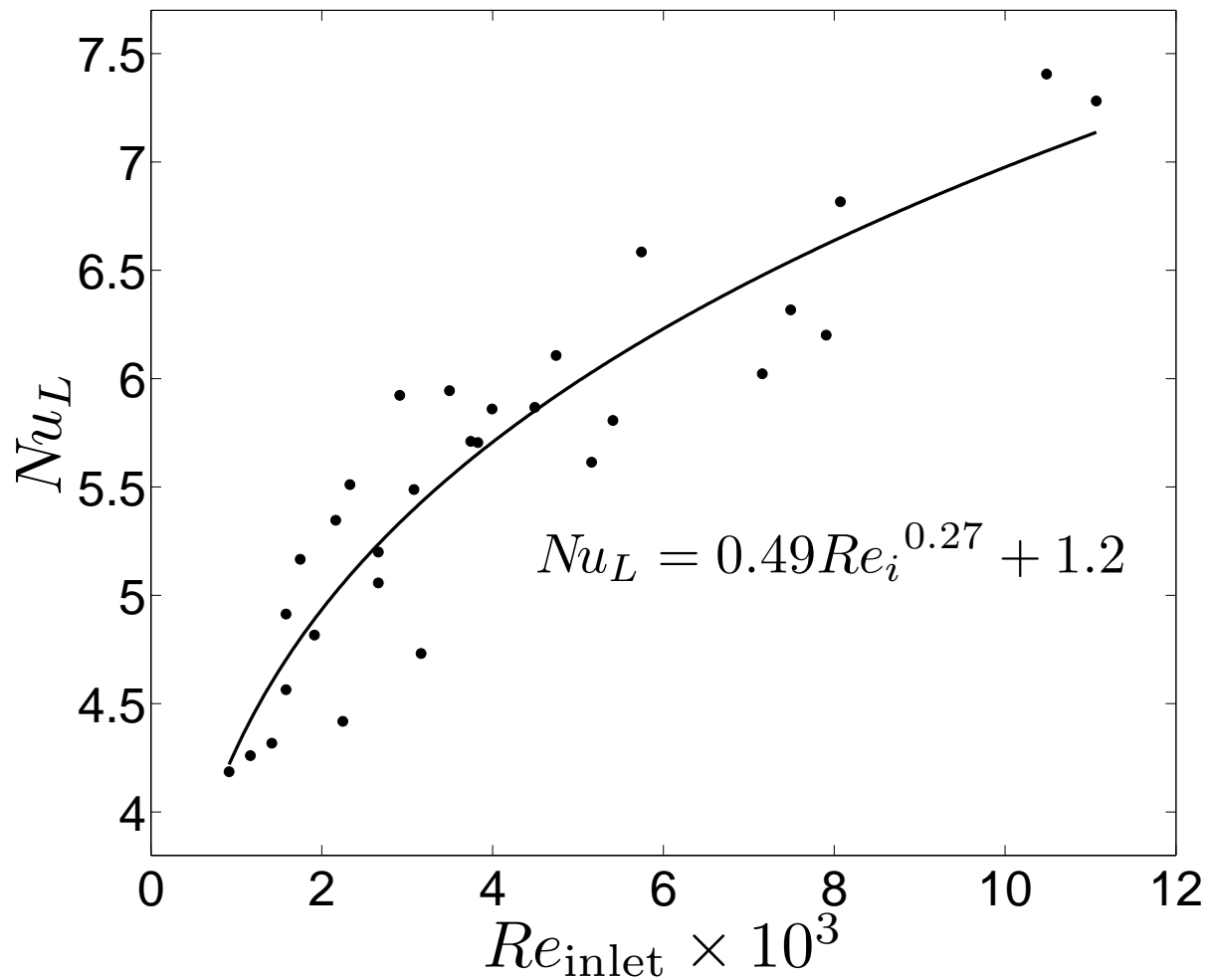


Figure B.2: Nusselt number on outer surface of top insulation,  $Nu_L$ , as a function of inlet Reynolds number,  $Re_{inlet}$ . Dots are experimental data; the curve is a power law least squares fit.  $Pr = 0.7$ ,  $\mathcal{I} = 0.4$ .

# Appendix C

## Solid Mechanics

The solid mechanics and dynamics of the blades and shaft play an important role in this system because of its high aspect ratios and lack of surplus power. From a manufacturing standpoint, there is little margin for error. The maximum angle from which the rotors can be tilted from planar without striking the stators is

$$\phi = \arctan\left(\frac{h_g}{r_t}\right) \quad (\text{C.1})$$

The strength and stiffness of the blades must be considered. Stresses on the blades due to aerodynamic loading and centripetal forces are negligible. However, impact loading due to repeated blade collisions with the stator could cause damage. The blades loaded under their own weight must not deflect greater than the gap height, in order to prevent collisions with the stator. The blades are modeled as cantilever beams of length  $r_t - r_s$ , with a rectangular cross section. The second moment of area of the blade, with a rectangular cross section is  $I = w_b h_b^3 / 12$ .

### C.1 Statics

The static deflection in the axial direction at the tip of a cantilever beam under a uniform distributed load,  $w$  (units of force/length) is

$$\delta = \frac{wL^4}{8EI} \quad (\text{C.2})$$

Where  $L$  is the total length of the beam and  $E_b$  is the elastic modulus of the beam. Inserting  $I_b$  and  $L$  and evaluating  $w = \rho_b g w_b h_b$  where  $\rho_b$  is the density of the beam material

$$\delta_{\text{weight}} = \frac{3\rho g (r_t - r_s)^4}{2E_b h_b^2} \quad (\text{C.3})$$

The blades are also be exposed to handling during manufacture and installation. This handling force is modeled as a tip load of 1 N, about the weight of an apple. The tip deflection due to a concentrated end load is

$$\delta = \frac{FL^3}{3EI} \quad (\text{C.4})$$

Again, inserting and evaluating variables,

$$\delta_{\text{conc}} = \frac{F_{\text{conc}} (r_t - r_s)^3}{3E_b I_b} \quad (\text{C.5})$$

Now it is desirable to see what stress is caused in the blade as a result of this load. The blade is under both shear and bending stress, but bending is dominant by far because of the high aspect ratio of the beam. The bending stress in an Euler-Bernoulli beam is  $\sigma = My/I$ . Where  $M$  is the bending moment and  $y$  is the distance from the neutral axis. The maximum stress is at the root of the beam, on the top and bottom surfaces. Care should be taken that the rotors are not exposed to stresses greater than the yield stress of the material of which they are composed.

$$\sigma_{\text{conc}} = \frac{F_{\text{conc}}(r_t - r_s)h_b}{2I_b} \quad (\text{C.6})$$

## C.2 Dynamics

### C.2.1 Natural Frequencies

(C.3) models the system statically. However, this is a dynamic system, and dynamic systems cause more deflection than static ones, especially at natural frequencies. An important dynamic force applied to this system is the forces due to rotor whirling which is due to inevitable rotor imbalance. This force is periodic in  $f$ . The forces on the blade are applied to the shaft, making this a base-driven system. The first natural frequency, that is, the fundamental, (in units of Hz) of an Euler-Bernoulli cantilever beam is approximately [24]

$$f_1 = \frac{0.597^2\pi}{2(r_t - r_s)^2} \sqrt{\frac{E_b I_b}{\rho_b h_b w_b}} \quad (\text{C.7})$$

Which, for an aluminum blade, is at a higher frequency than the operating range being considered and all other natural frequencies are even higher than the fundamental. Since the system is not operating near any natural frequencies, even if zero damping ratio is conservatively assumed, the dynamic deflection should not be more than a few times greater than the static deflection under the same load. The natural frequencies of rotating turbine blades are higher than nonrotating turbine blades [25] due to the stiffening effect of centrifugal acceleration, thus the operating frequency is expected to be much lower than the fundamental frequency of the rotating blades.

There is a natural frequency associated with the oscillating mass imbalance inherent to all rotors that is known as the critical speed, which should be avoided. The critical speed for a simple shaft (no concentrated masses, only the distributed mass of the shaft) is the square root of the bending stiffness of the shaft divided by the mass of the shaft. Since the mass of the shaft is distributed, the bending stiffness of a simply supported beam under a uniform load is used [26].

$$\omega_s = \sqrt{\frac{384E_s I_s}{5m_s L_s^3}} \quad (\text{C.8})$$

The  $s$  subscript indicates that the variable in discussion refers to the shaft. However, the shaft has  $n_r$  rotors attached to it, adding additional mass but not increasing the shaft

stiffness. These masses act like point loads on the shaft, thus the stiffness of the system is considered as a simply supported beam with a point load. The stiffness of such a beam is [27]:

$$k_j = \frac{3E_s I_s}{L_s^3} \left[ \frac{\tilde{y}(j)}{L_s} \left( 1 - \frac{\tilde{y}(j)}{L_s} \right) \right]^{-1} \quad (\text{C.9})$$

Thus, the natural frequency of each rotor-shaft system is:

$$\omega_j = \sqrt{\frac{3E_s I_s}{m_r L_s^3} \left[ \frac{\tilde{y}(j)}{L_s} \left( 1 - \frac{\tilde{y}(j)}{L_s} \right) \right]^{-1}} \quad (\text{C.10})$$

Where  $\tilde{y}(j)$  is the axial position of the rotor on the shaft;  $\tilde{y}$  is defined from bearing to bearing. Dunkerley's method can be used to find the first critical speed of the overall system, in Hz [28].

$$f_c = \frac{1}{2\pi} \left( \frac{1}{\omega_s^2} + \sum_{j=1}^{n_r} \frac{1}{\omega_j^2} \right)^{-\frac{1}{2}} \quad (\text{C.11})$$

This critical speed is also higher than the operating speed of the rotor, meaning that the whirling mode of vibration will not be excited significantly. For a shaft with rotors similar to the multilayer assembly of Ch. 6,  $f_c = 290$  Hz.

### C.2.2 Shock Loads

The project requirements specify sustained performance in the presence of 10 g shock loads of 11 ms duration. Treating this shock as an impulse, the shock induces a 1.187 m/s initial velocity in the system. The shock is translated to the blades from the shaft, making this a support motion vibration problem. In this case support motion is the same as a load applied directly to the mass. The blade is a continuous system, modeled as a cantilever beam. However, the only mode of interest is the primary mode because it causes tip deflection which will be the point of greatest deflection when an exciting function with every frequency in its spectrum, such as an impulse function, is applied.

Assuming zero damping ratio (a reasonable and conservative assumption) the deflection as a function of time is a sine curve of amplitude initial velocity divided by the first natural frequency of the blade [29].

$$\delta_{\text{shock}} = \frac{10 \times 9.81 \text{ m s}^{-2} \times 11 \text{ ms}}{\omega_1} \quad (\text{C.12})$$

### C.2.3 Centrifugal Acceleration

Since the clearances between the rotors and stators are so tight, the effect of centrifugal acceleration in straightening the blades toward the radial direction is now considered.

Inevitably, during the assembly process there is some amount of misalignment between the plane of rotation of the rotors and the orthogonal plane to the shaft, along which the

stators are also nominally oriented. As the blades spin, they are subjected to an inertial force which tends to straighten them, but that force is resisted by the blades' stiffness. The interplay of these forces can be calculated.

The blade may be modeled as an Euler-Bernoulli beam rotating about one of its ends on an axis nearly perpendicular to the axis of the beam. Small deflection approximations are assumed. The radial force in the radial direction of the blade due to inertial acceleration in the radial direction is:

$$F(r) = \int_r^{r_t} \rho_b w_b h_b \omega^2 r \, dr = \frac{\rho_b w_b h_b \omega^2}{2} (r_t^2 - r^2) \quad (\text{C.13})$$

The shear force in the beam is the component of  $F(r)$  in the transverse direction to the undeflected beam. With a small angle approximation, the shear force in the beam is:

$$V(r) = \frac{d\delta}{dr} F(r) \quad (\text{C.14})$$

The distributed load along the beam, with units of force per length is

$$-w(r) = \frac{d}{dr}(V(r)) = \frac{dF}{dr} \frac{d\delta}{dr} + F \frac{d^2\delta}{dr^2} = EI \frac{d^4\delta}{dr^4} \quad (\text{C.15})$$

Solving for  $dF/dr$  and rearranging

$$EI \frac{d^4\delta}{dr^4} - \frac{1}{2} \rho_b w_b h_b \omega^2 r_t^2 \frac{d}{dr} \left[ \left( 1 - \frac{r^2}{r_t^2} \right) \frac{d\delta}{dr} \right] = 0 \quad (\text{C.16})$$

(C.16) is a linear, homogeneous, non-autonomous, 4<sup>th</sup> order, ordinary differential equation [25]. It is solved numerically and plotted in Fig. C.1.

Fig. C.1 shows the effect of centrifugal straightening for a variety of blades spinning at 5000 rpm. Note that because Fig. C.1 is plotted nondimensionally, the plot is independent of the amount of static misalignment. Metal blades were found to have no appreciable straightening effect at 5000 rpm due to their high elastic modulus. As seen in Fig. C.1, for acrylic blades, the tip deflection while spinning is about 90% as large as the static deflection. For materials with a lower elastic modulus such as ethylene-vinyl acetate and polytetrafluoroethylene, the tip deflection is about 60% of the static misalignment, which is a significant amount of straightening.

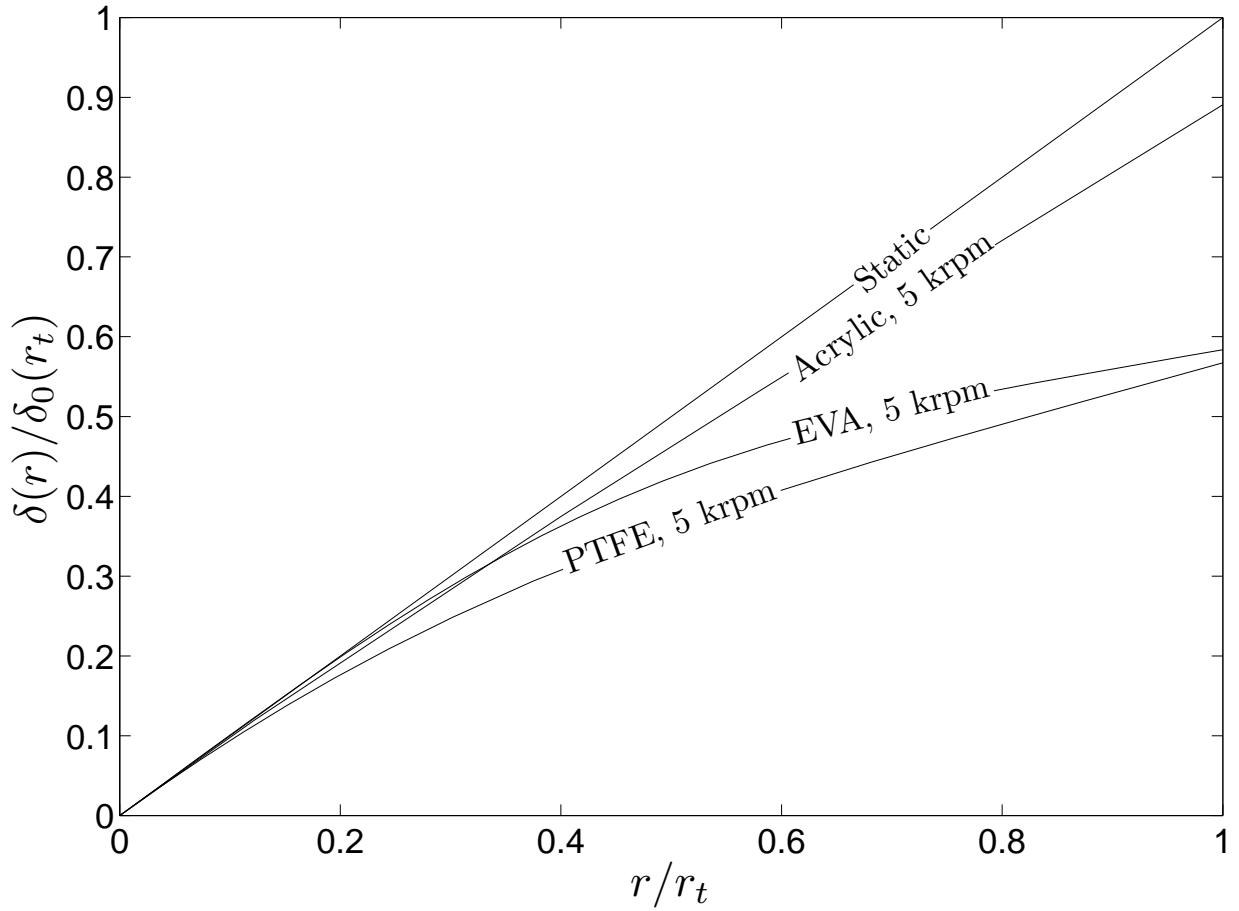


Figure C.1: Dimensionless plot of blade straightening due to centrifugal acceleration. Curves show blade shape as a function of radius. Ordinate is the ratio of deflection from the in-plane condition to the static deflection from the in-plane condition. Abscissa is the ratio of radius to tip radius. The axis of rotation is in the direction of the ordinate. The nominal plane of rotation is in the direction of the abscissa, however manufacturing tolerances cause the rotor to be out of the nominal plane. A statically misaligned blade shape is shown as ‘static’, with static misalignment of  $\delta_0(r) = r\delta_0(r_t)$ . Other curves show straightening of this misalignment for blades made of several materials, spinning at 5000 rpm.

# Appendix D

## Heat Sink Quantities

Table D.1: Pareto optimal single-layer design,  $\dot{W} = 0.72 \text{ W}$

Variable	Value	Unit
$r_i$	20	mm
$r_t$	50	mm
$h_c$	3.4	mm
$h_b$	1.5	mm
$h_g$	950	$\mu\text{m}$
$\beta_b(r_t)$	-45	$^\circ$
$n_b$	5	-
$\omega$	520	$\text{rad s}^{-1}$
$f$	5000	rpm
$f_{\text{Hz}}$	83	Hz
$B$	0.023	-
$G$	0.068	-
$\mathcal{I}$	0.4	-

Table D.2: Pareto optimal single-layer design,  $\dot{W} = 0.72$  W, continued

Variable	Value	Unit
$Re_\omega$	78,000	-
$C_f$	0.065	-
$\sigma$	0.11	-
$\varepsilon$	0.43	-
$\dot{m}$	4.9	g s <sup>-1</sup>
$\dot{V}$	4.3	L s <sup>-1</sup>
$\Delta p_{\text{rise}}$	167	Pa
$R$	0.43	KW <sup>-1</sup>
$\dot{W}$	0.72	W
$\phi$	0.53	°
$\delta_{\text{weight}}$	-2	μm
$\delta_{\text{shock}}$	430	μm
$\delta_{\text{conc}}$	-590	μm
$\sigma_{\text{conc}}$	33	MPa
$f_1$	990	Hz



# Appendix E

## Selected Raw Data

This chapter includes raw data from selected experiments. Table E.1 gives data from a hot-wire anemometer run, Tables E.2 through E.6 are for data from the heat transfer experiment. The data from the CFD experiments is shown in Table 4.1.

### E.1 Hot-Wire Anemometer Data

Table E.1: Raw data from the hot wire anemometer. This test was done in conjunction with many other experiments with the hot-wire anemometer to determine the mass flow rate through the single layer experimental set up. This particular test was run with a rotor angular speed of 5000 rpm, with  $h_b = 1.04$  mm, and  $h_c = 1.6$  mm; the probe scans in the  $y$  direction, which is across the narrower dimension of the heat sink exit plane. In the  $x$  direction (across the width of the heat sink), the probe is located in the middle of the heat sink (i.e. 50 mm from either side); the probe is oriented to face the flow direction which comes out at an angle to the exit plane. The left column displays time in seconds from the initiation of data collection. The middle column displays the electrical potential output of the hot-wire anemometer probe, in volts. This data is then converted to an effective cooling velocity via King's law and calibration constants. The right column displays the voltage of the potentiometer which is used, with calibration data, to find the position of the hot-wire probe. Tables begin on the next page.

time	HWA V.	disp. V.
0.000000	4.354090	3.919414
0.010000	4.139194	3.909646
0.020000	4.266178	3.909646
0.030000	4.188034	3.914530
0.040000	4.275946	3.914530
0.050000	4.339438	3.909646
0.060000	3.987790	3.909646
0.070000	4.339438	3.909646
0.080000	4.090354	3.914530
0.090000	3.777778	3.914530
0.100000	4.041514	3.909646
0.110000	4.427350	3.909646
0.120000	3.953602	3.914530
0.130000	4.686203	3.914530
0.140000	4.217338	3.919414
0.150000	4.661783	3.909646
0.160000	3.909646	3.909646
0.170000	4.349206	3.914530
0.180000	4.481074	3.919414
0.190000	4.300366	3.914530
0.200000	3.963370	3.914530
0.210000	4.178266	3.909646
0.220000	4.456654	3.914530
0.230000	4.271062	3.914530
0.240000	4.393162	3.914530
0.250000	4.085470	3.914530
0.260000	4.065934	3.909646
0.270000	3.914530	3.909646
0.280000	4.476190	3.909646
0.290000	3.782662	3.914530
0.300000	3.948718	3.914530
0.310000	4.534799	3.909646
0.320000	4.041514	3.914530
0.330000	4.105006	3.914530
0.340000	4.490842	3.914530
0.350000	4.715507	3.914530
0.360000	4.090354	3.904762
0.370000	3.890110	3.914530
0.380000	4.134310	3.914530
0.390000	4.021978	3.914530
0.400000	4.280830	3.914530
0.410000	4.290598	3.914530
0.420000	4.114774	3.914530
0.430000	4.056166	3.914530
0.440000	4.207570	3.914530
0.450000	4.271062	3.909646
0.460000	4.358974	3.909646
0.470000	3.963370	3.914530
0.480000	4.329670	3.919414
0.490000	4.427350	3.914530
0.500000	4.105006	3.909646
0.510000	4.603175	3.914530
0.520000	4.124542	3.914530
0.530000	4.241758	3.919414
0.540000	3.758242	3.914530
0.550000	4.490842	3.909646
0.560000	4.310134	3.909646
0.570000	4.490842	3.909646
0.580000	4.461538	3.909646
0.590000	4.134310	3.909646
0.600000	4.007326	3.904762
0.610000	4.251526	3.909646
0.620000	4.339438	3.914530
0.630000	4.334554	3.909646
0.640000	4.114774	3.909646
0.650000	4.315018	3.909646
0.660000	4.031746	3.914530
0.670000	4.095238	3.919414
0.680000	4.329670	3.919414
0.690000	4.334554	3.909646
0.700000	4.715507	3.914530
0.710000	4.031746	3.914530
0.720000	4.222222	3.909646
0.730000	4.520147	3.914530
0.740000	4.222222	3.914530
0.750000	4.358974	3.914530
0.760000	4.280830	3.914530
0.770000	4.163614	3.919414

time	HWA V.	disp. V.
0.780000	4.061050	3.914530
0.790000	4.051282	3.909646
0.800000	4.251526	3.914530
0.810000	4.525031	3.909646
0.820000	4.422466	3.914530
0.830000	4.481074	3.909646
0.840000	4.388278	3.909646
0.850000	4.202686	3.914530
0.860000	4.510379	3.909646
0.870000	4.642247	3.914530
0.880000	4.026862	3.914530
0.890000	4.158730	3.904762
0.900000	4.109890	3.909646
0.910000	4.627595	3.909646
0.920000	4.241758	3.914530
0.930000	4.178266	3.914530
0.940000	4.315018	3.909646
0.950000	4.451770	3.914530
0.960000	4.334554	3.919414
0.970000	4.520147	3.914530
0.980000	4.500611	3.914530
0.990000	4.339438	3.914530
1.000000	4.002442	3.914530
1.010000	4.466422	3.914530
1.020000	4.549451	3.914530
1.030000	4.886447	3.919414
1.040000	4.627595	3.914530
1.050000	4.539683	3.909646
1.060000	4.349206	3.914530
1.070000	4.109890	3.914530
1.080000	3.992674	3.914530
1.090000	4.446886	3.914530
1.100000	4.515263	3.909646
1.110000	4.373626	3.909646
1.120000	4.271062	3.909646
1.130000	4.588523	3.914530
1.140000	4.090354	3.914530
1.150000	4.319902	3.909646
1.160000	4.500611	3.909646
1.170000	4.622711	3.914530
1.180000	4.769231	3.914530
1.190000	4.256410	3.919414
1.200000	4.632479	3.914530
1.210000	4.197802	3.909646
1.220000	4.554335	3.909646
1.230000	4.417582	3.914530
1.240000	4.905983	3.914530
1.250000	4.344322	3.914530
1.260000	4.612943	3.914530
1.270000	4.481074	3.909646
1.280000	4.168498	3.909646
1.290000	4.598291	3.909646
1.300000	4.451770	3.919414
1.310000	4.442002	3.909646
1.320000	4.505495	3.909646
1.330000	4.778999	3.909646
1.340000	4.627595	3.914530
1.350000	4.554335	3.914530
1.360000	4.818071	3.914530
1.370000	4.598291	3.904762
1.380000	3.860806	3.909646
1.390000	4.197802	3.914530
1.400000	4.432234	3.909646
1.410000	4.090354	3.914530
1.420000	4.720391	3.909646
1.430000	4.568987	3.909646
1.440000	4.534799	3.909646
1.450000	4.642247	3.919414
1.460000	4.637363	3.919414
1.470000	4.505495	3.919414
1.480000	4.495726	3.914530
1.490000	4.446886	3.914530
1.500000	4.593407	3.914530
1.510000	4.642247	3.919414
1.520000	4.666667	3.914530
1.530000	4.739927	3.909646
1.540000	4.529915	3.909646
1.550000	4.544567	3.914530

time	HWA V.	disp. V.
1.560000	4.642247	3.909646
1.570000	4.490842	3.914530
1.580000	4.363858	3.909646
1.590000	4.539683	3.904762
1.600000	4.261294	3.909646
1.610000	4.549451	3.909646
1.620000	4.476190	3.914530
1.630000	4.627595	3.914530
1.640000	4.695971	3.909646
1.650000	4.627595	3.909646
1.660000	4.139194	3.914530
1.670000	4.632479	3.909646
1.680000	4.534799	3.909646
1.690000	4.539683	3.904762
1.700000	4.783883	3.919414
1.710000	4.705739	3.919414
1.720000	4.857143	3.914530
1.730000	4.603175	3.909646
1.740000	4.652015	3.914530
1.750000	4.368742	3.919414
1.760000	4.417582	3.914530
1.770000	4.163614	3.914530
1.780000	4.334554	3.919414
1.790000	4.398046	3.909646
1.800000	4.749695	3.914530
1.810000	4.427350	3.919414
1.820000	4.730159	3.914530
1.830000	4.295482	3.909646
1.840000	4.388278	3.904762
1.850000	4.666667	3.909646
1.860000	4.603175	3.914530
1.870000	4.676435	3.909646
1.880000	4.656899	3.904762
1.890000	4.525031	3.909646
1.900000	4.442002	3.909646
1.910000	4.383394	3.914530
1.920000	4.373626	3.919414
1.930000	4.700855	3.904762
1.940000	4.764347	3.909646
1.950000	4.793651	3.909646
1.960000	4.495726	3.914530
1.970000	4.612943	3.914530
1.980000	4.446886	3.909646
1.990000	4.617827	3.909646
2.000000	4.862027	3.914530
2.010000	4.778999	3.909646
2.020000	4.427350	3.914530
2.030000	4.481074	3.914530
2.040000	4.280830	3.914530
2.050000	4.388278	3.909646
2.060000	4.686203	3.914530
2.070000	4.808303	3.914530
2.080000	4.681319	3.909646
2.090000	4.554335	3.904762
2.100000	4.554335	3.909646
2.110000	4.456654	3.909646
2.120000	4.402930	3.914530
2.130000	4.749695	3.909646
2.140000	4.383394	3.904762
2.150000	4.759463	3.909646
2.160000	4.358974	3.909646
2.170000	4.647131	3.919414
2.180000	4.568987	3.909646
2.190000	4.876679	3.909646
2.200000	4.974359	3.909646
2.210000	4.412698	3.914530
2.220000	4.603175	3.914530
2.230000	4.730159	3.914530
2.240000	4.354090	3.914530
2.250000	4.754579	3.914530
2.260000	4.749695	3.914530
2.270000	4.549451	3.914530
2.280000	4.749695	3.914530
2.290000	4.573871	3.909646
2.300000	4.183150	3.909646
2.310000	4.246642	3.914530
2.320000	4.915751	3.919414
2.330000	4.588523	3.909646

time	HWA V.	disp. V.
2.340000	4.852259	3.909646
2.350000	4.700855	3.909646
2.360000	4.349206	3.914530
2.370000	4.700855	3.909646
2.380000	4.603175	3.904762
2.390000	4.969475	3.909646
2.400000	4.886447	3.914530
2.410000	4.774115	3.909646
2.420000	4.554335	3.909646
2.430000	4.388278	3.909646
2.440000	4.329670	3.909646
2.450000	4.886447	3.909646
2.460000	4.393162	3.914530
2.470000	4.735043	3.909646
2.480000	4.656899	3.909646
2.490000	4.124542	3.914530
2.500000	4.730159	3.914530
2.510000	4.515263	3.914530
2.520000	4.671551	3.914530
2.530000	4.471306	3.909646
2.540000	4.940171	3.914530
2.550000	4.525031	3.914530
2.560000	4.451770	3.919414
2.570000	4.388278	3.909646
2.580000	4.647131	3.909646
2.590000	4.564103	3.909646
2.600000	4.891331	3.914530
2.610000	4.710623	3.909646
2.620000	4.476190	3.909646
2.630000	4.564103	3.909646
2.640000	4.617827	3.909646
2.650000	4.847375	3.909646
2.660000	4.710623	3.914530
2.670000	4.818071	3.914530
2.680000	4.808303	3.904762
2.690000	4.803419	3.904762
2.700000	4.485958	3.909646
2.710000	4.725275	3.909646
2.720000	4.676435	3.914530
2.730000	4.803419	3.909646
2.740000	4.764347	3.909646
2.750000	4.959707	3.909646
2.760000	4.642247	3.909646
2.770000	4.568987	3.919414
2.780000	4.080586	3.909646
2.790000	4.246642	3.914530
2.800000	4.490842	3.904762
2.810000	4.925519	3.914530
2.820000	4.862027	3.909646
2.830000	4.344322	3.914530
2.840000	4.578755	3.909646
2.850000	4.153846	3.909646
2.860000	4.652015	3.914530
2.870000	4.627595	3.904762
2.880000	4.862027	3.909646
2.890000	4.588523	3.909646
2.900000	4.642247	3.909646
2.910000	4.505495	3.909646
2.920000	4.275946	3.914530
2.930000	4.432234	3.909646
2.940000	4.466422	3.909646
2.950000	4.632479	3.909646
2.960000	4.510379	3.904762
2.970000	4.334554	3.909646
2.980000	4.554335	3.914530
2.990000	4.280830	3.909646
3.000000	4.300366	3.914530
3.010000	4.178266	3.909646
3.020000	4.822955	3.909646
3.030000	4.774115	3.914530
3.040000	4.612943	3.914530
3.050000	4.319902	3.914530
3.060000	4.446886	3.909646
3.070000	4.412698	3.914530
3.080000	4.446886	3.914530
3.090000	4.866911	3.914530
3.100000	4.212454	3.914530
3.110000	4.393162	3.909646

time	HWA V.	disp. V.
3.120000	4.402930	3.914530
3.130000	4.481074	3.909646
3.140000	4.695971	3.909646
3.150000	4.793651	3.904762
3.160000	4.051282	3.909646
3.170000	4.393162	3.909646
3.180000	4.310134	3.914530
3.190000	4.485958	3.909646
3.200000	4.261294	3.919414
3.210000	4.236874	3.909646
3.220000	4.505495	3.909646
3.230000	4.593407	3.909646
3.240000	4.710623	3.909646
3.250000	4.070818	3.914530
3.260000	4.363858	3.914530
3.270000	4.568987	3.909646
3.280000	4.515263	3.909646
3.290000	4.383394	3.914530
3.300000	4.300366	3.919414
3.310000	4.417582	3.914530
3.320000	4.227106	3.909646
3.330000	4.432234	3.909646
3.340000	4.310134	3.914530
3.350000	4.451770	3.914530
3.360000	4.901099	3.909646
3.370000	4.412698	3.909646
3.380000	3.807082	3.914530
3.390000	4.520147	3.914530
3.400000	4.310134	3.914530
3.410000	4.285714	3.909646
3.420000	4.661783	3.909646
3.430000	4.871795	3.909646
3.440000	4.422466	3.909646
3.450000	4.593407	3.914530
3.460000	4.515263	3.904762
3.470000	4.095238	3.904762
3.480000	4.559219	3.904762
3.490000	4.212454	3.909646
3.500000	4.798535	3.909646
3.510000	4.769231	3.909646
3.520000	4.178266	3.914530
3.530000	3.968254	3.914530
3.540000	4.334554	3.914530
3.550000	4.710623	3.914530
3.560000	4.783883	3.914530
3.570000	4.852259	3.914530
3.580000	4.573871	3.909646
3.590000	3.992674	3.919414
3.600000	3.894994	3.919414
3.610000	4.349206	3.914530
3.620000	4.612943	3.914530
3.630000	4.153846	3.914530
3.640000	4.617827	3.909646
3.650000	4.544567	3.914530
3.660000	4.388278	3.909646
3.670000	3.943834	3.904762
3.680000	4.398046	3.914530
3.690000	4.564103	3.914530
3.700000	4.363858	3.914530
3.710000	4.749695	3.909646
3.720000	4.363858	3.909646
3.730000	4.432234	3.909646
3.740000	3.934066	3.914530
3.750000	4.217338	3.914530
3.760000	4.271062	3.909646
3.770000	4.261294	3.909646
3.780000	4.061050	3.919414
3.790000	4.007326	3.919414
3.800000	4.354090	3.914530
3.810000	4.451770	3.909646
3.820000	3.797314	3.909646
3.830000	4.407814	3.919414
3.840000	4.686203	3.914530
3.850000	4.720391	3.914530
3.860000	4.251526	3.909646
3.870000	3.948718	3.914530
3.880000	4.017094	3.914530
3.890000	4.671551	3.914530

time	HWA V.	disp. V.
3.900000	4.578755	3.919414
3.910000	4.627595	3.909646
3.920000	4.564103	3.909646
3.930000	4.363858	3.914530
3.940000	4.168498	3.909646
3.950000	4.300366	3.909646
3.960000	4.051282	3.909646
3.970000	4.046398	3.909646
3.980000	4.139194	3.914530
3.990000	4.627595	3.909646
4.000000	3.953602	3.914530
4.010000	3.953602	3.909646
4.020000	4.236874	3.909646
4.030000	4.075702	3.909646
4.040000	4.271062	3.914530
4.050000	3.831502	3.919414
4.060000	4.490842	3.914530
4.070000	4.300366	3.909646
4.080000	4.134310	3.914530
4.090000	4.197802	3.909646
4.100000	4.222222	3.919414
4.110000	4.231990	3.914530
4.120000	3.865690	3.914530
4.130000	4.095238	3.909646
4.140000	4.061050	3.919414
4.150000	3.948718	3.919414
4.160000	4.139194	3.914530
4.170000	3.641026	3.914530
4.180000	4.285714	3.909646
4.190000	4.373626	3.914530
4.200000	4.061050	3.909646
4.210000	4.163614	3.914530
4.220000	3.973138	3.914530
4.230000	4.241758	3.909646
4.240000	3.885226	3.914530
4.250000	4.290598	3.914530
4.260000	4.017094	3.914530
4.270000	3.797314	3.914530
4.280000	4.021978	3.909646
4.290000	4.139194	3.909646
4.300000	4.144078	3.914530
4.310000	3.684982	3.919414
4.320000	4.271062	3.919414
4.330000	4.280830	3.909646
4.340000	4.212454	3.914530
4.350000	4.002442	3.914530
4.360000	4.105006	3.914530
4.370000	3.826618	3.914530
4.380000	4.500611	3.914530
4.390000	3.611722	3.909646
4.400000	3.494505	3.909646
4.410000	4.290598	3.919414
4.420000	3.973138	3.919414
4.430000	4.305250	3.909646
4.440000	4.100122	3.909646
4.450000	3.894994	3.914530
4.460000	3.675214	3.909646
4.470000	4.354090	3.909646
4.480000	3.919414	3.919414
4.490000	4.217338	3.914530
4.500000	4.344322	3.909646
4.510000	3.865690	3.914530
4.520000	4.002442	3.909646
4.530000	3.841270	3.919414
4.540000	4.148962	3.909646
4.550000	4.398046	3.904762
4.560000	4.315018	3.914530
4.570000	4.231990	3.914530
4.580000	3.763126	3.914530
4.590000	4.031746	3.919414
4.600000	3.992674	3.914530
4.610000	3.807082	3.914530
4.620000	4.217338	3.914530
4.630000	3.597070	3.919414
4.640000	3.992674	3.914530
4.650000	4.383394	3.919414
4.660000	4.227106	3.909646
4.670000	3.704518	3.909646

time	HWA V.	disp. V.
4.680000	3.758242	3.919414
4.690000	3.768010	3.914530
4.700000	3.938950	3.919414
4.710000	3.836386	3.909646
4.720000	3.885226	3.909646
4.730000	3.953602	3.909646
4.740000	4.632479	3.919414
4.750000	3.831502	3.919414
4.760000	4.041514	3.914530
4.770000	3.851038	3.909646
4.780000	3.943834	3.914530
4.790000	3.743590	3.914530
4.800000	3.978022	3.919414
4.810000	3.748474	3.914530
4.820000	4.031746	3.909646
4.830000	3.929182	3.914530
4.840000	4.173382	3.914530
4.850000	3.938950	3.924298
4.860000	3.992674	3.909646
4.870000	4.231990	3.914530
4.880000	3.733822	3.914530
4.890000	3.855922	3.914530
4.900000	3.943834	3.919414
4.910000	3.870574	3.919414
4.920000	3.528694	3.909646
4.930000	3.792430	3.914530
4.940000	3.719170	3.914530
4.950000	3.826618	3.914530
4.960000	4.046398	3.909646
4.970000	3.699634	3.909646
4.980000	4.017094	3.914530
4.990000	3.870574	3.909646
5.000000	3.851038	3.919414
5.010000	4.036630	3.914530
5.020000	4.026862	3.909646
5.030000	3.748474	3.909646
5.040000	3.811966	3.914530
5.050000	3.719170	3.914530
5.060000	3.987790	3.914530
5.070000	3.934066	3.909646
5.080000	3.807082	3.914530
5.090000	3.904762	3.914530
5.100000	3.943834	3.919414
5.110000	3.958486	3.914530
5.120000	3.797314	3.914530
5.130000	3.489621	3.909646
5.140000	4.031746	3.914530
5.150000	3.865690	3.919414
5.160000	3.899878	3.919414
5.170000	3.846154	3.914530
5.180000	3.973138	3.914530
5.190000	4.021978	3.919414
5.200000	3.548230	3.914530
5.210000	3.606838	3.919414
5.220000	3.894994	3.914530
5.230000	3.821734	3.919414
5.240000	3.894994	3.909646
5.250000	3.973138	3.914530
5.260000	3.728938	3.914530
5.270000	3.455433	3.914530
5.280000	4.017094	3.909646
5.290000	3.938950	3.909646
5.300000	3.997558	3.914530
5.310000	3.807082	3.914530
5.320000	3.792430	3.914530
5.330000	3.606838	3.904762
5.340000	3.455433	3.919414
5.350000	4.173382	3.914530
5.360000	3.890110	3.919414
5.370000	3.992674	3.914530
5.380000	3.890110	3.914530
5.390000	3.909646	3.909646
5.400000	3.694750	3.919414
5.410000	3.802198	3.919414
5.420000	3.860806	3.919414
5.430000	4.109890	3.914530
5.440000	3.743590	3.914530
5.450000	3.860806	3.919414

time	HWA V.	disp. V.
5.460000	3.733822	3.914530
5.470000	3.733822	3.909646
5.480000	3.518926	3.909646
5.490000	3.636142	3.914530
5.500000	3.846154	3.919414
5.510000	3.738706	3.914530
5.520000	3.523810	3.909646
5.530000	3.553114	3.914530
5.540000	3.474969	3.914530
5.550000	3.968254	3.909646
5.560000	3.440781	3.909646
5.570000	3.626374	3.909646
5.580000	3.831502	3.909646
5.590000	3.728938	3.914530
5.600000	4.197802	3.914530
5.610000	3.479853	3.909646
5.620000	3.606838	3.919414
5.630000	3.694750	3.914530
5.640000	3.650794	3.919414
5.650000	3.665446	3.914530
5.660000	3.748474	3.914530
5.670000	3.763126	3.914530
5.680000	3.440781	3.919414
5.690000	3.406593	3.914530
5.700000	3.445665	3.919414
5.710000	3.841270	3.914530
5.720000	3.597070	3.919414
5.730000	3.763126	3.919414
5.740000	3.504274	3.909646
5.750000	3.670330	3.909646
5.760000	3.440781	3.909646
5.770000	3.655678	3.914530
5.780000	3.851038	3.914530
5.790000	3.860806	3.909646
5.800000	3.567766	3.909646
5.810000	3.675214	3.914530
5.820000	3.934066	3.914530
5.830000	3.655678	3.914530
5.840000	4.021978	3.909646
5.850000	3.777778	3.909646
5.860000	3.504274	3.914530
5.870000	3.611722	3.919414
5.880000	3.733822	3.914530
5.890000	3.567766	3.914530
5.900000	3.768010	3.914530
5.910000	3.875458	3.914530
5.920000	3.645910	3.919414
5.930000	3.870574	3.914530
5.940000	3.963370	3.914530
5.950000	3.997558	3.909646
5.960000	3.836386	3.914530
5.970000	3.885226	3.919414
5.980000	3.557998	3.914530
5.990000	3.758242	3.909646
6.000000	3.553114	3.914530
6.010000	3.455433	3.914530
6.020000	3.523810	3.914530
6.030000	3.963370	3.914530
6.040000	3.621490	3.909646
6.050000	3.924298	3.904762
6.060000	3.645910	3.909646
6.070000	3.694750	3.919414
6.080000	3.582418	3.914530
6.090000	4.065934	3.914530
6.100000	3.968254	3.909646
6.110000	3.885226	3.909646
6.120000	3.699634	3.914530
6.130000	3.919414	3.919414
6.140000	3.636142	3.909646
6.150000	4.280830	3.914530
6.160000	3.631258	3.914530
6.170000	3.660562	3.919414
6.180000	3.973138	3.914530
6.190000	3.699634	3.914530
6.200000	3.772894	3.914530
6.210000	3.724054	3.914530
6.220000	3.450549	3.914530
6.230000	3.474969	3.909646

time	HWA V.	disp. V.
6.240000	3.968254	3.919414
6.250000	3.968254	3.909646
6.260000	3.621490	3.914530
6.270000	3.772894	3.914530
6.280000	3.748474	3.914530
6.290000	3.597070	3.914530
6.300000	3.406593	3.914530
6.310000	3.684982	3.909646
6.320000	3.948718	3.914530
6.330000	3.772894	3.914530
6.340000	3.841270	3.909646
6.350000	3.616606	3.914530
6.360000	3.748474	3.914530
6.370000	4.017094	3.919414
6.380000	3.841270	3.914530
6.390000	3.626374	3.909646
6.400000	3.880342	3.919414
6.410000	3.455433	3.919414
6.420000	3.582418	3.919414
6.430000	3.416361	3.914530
6.440000	3.577534	3.909646
6.450000	3.343101	3.919414
6.460000	3.772894	3.919414
6.470000	3.641026	3.919414
6.480000	3.535578	3.914530
6.490000	3.465201	3.914530
6.500000	3.684982	3.919414
6.510000	3.440781	3.914530
6.520000	3.650794	3.909646
6.530000	3.948718	3.909646
6.540000	3.650794	3.914530
6.550000	3.665446	3.914530
6.560000	3.264957	3.914530
6.570000	4.358974	3.909646
6.580000	3.548230	3.909646
6.590000	4.075702	3.909646
6.600000	3.650794	3.914530
6.610000	3.435897	3.914530
6.620000	3.636142	3.909646
6.630000	3.899878	3.909646
6.640000	3.885226	3.914530
6.650000	3.660562	3.919414
6.660000	4.090354	3.919414
6.670000	3.641026	3.914530
6.680000	4.031746	3.914530
6.690000	3.645910	3.914530
6.700000	4.134310	3.914530
6.710000	3.763126	3.914530
6.720000	3.557998	3.909646
6.730000	3.929182	3.914530
6.740000	3.562882	3.914530
6.750000	3.543346	3.914530
6.760000	3.719170	3.914530
6.770000	3.387057	3.914530
6.780000	3.841270	3.909646
6.790000	3.851038	3.914530
6.800000	3.885226	3.919414
6.810000	3.719170	3.909646
6.820000	3.797314	3.909646
6.830000	4.124542	3.914530
6.840000	3.372405	3.919414
6.850000	3.675214	3.914530
6.860000	3.528694	3.914530
6.870000	3.548230	3.904762
6.880000	3.870574	3.909646
6.890000	3.860806	3.919414
6.900000	3.909646	3.919414
6.910000	3.411477	3.914530
6.920000	3.611722	3.919414
6.930000	3.504274	3.919414
6.940000	3.870574	3.919414
6.950000	3.855922	3.914530
6.960000	3.587302	3.909646
6.970000	3.758242	3.914530
6.980000	4.246642	3.914530
6.990000	3.816850	3.919414
7.000000	3.934066	3.914530
7.010000	3.743590	3.909646

time	HWA V.	disp. V.	time	HWA V.	disp. V.
7.020000	3.831502	3.914530	7.800000	3.904762	3.914530
7.030000	3.636142	3.914530	7.810000	3.816850	3.909646
7.040000	3.592186	3.914530	7.820000	3.841270	3.909646
7.050000	3.724054	3.909646	7.830000	4.046398	3.909646
7.060000	3.606838	3.904762	7.840000	3.626374	3.914530
7.070000	3.870574	3.909646	7.850000	3.894994	3.914530
7.080000	4.026862	3.914530	7.860000	3.362637	3.909646
7.090000	3.836386	3.909646	7.870000	3.782662	3.909646
7.100000	3.489621	3.909646	7.880000	3.572650	3.914530
7.110000	3.968254	3.909646	7.890000	4.393162	3.914530
7.120000	3.567766	3.914530	7.900000	3.963370	3.909646
7.130000	3.953602	3.914530	7.910000	3.616606	3.909646
7.140000	3.860806	3.909646	7.920000	3.660562	3.909646
7.150000	3.616606	3.904762	7.930000	3.445665	3.919414
7.160000	3.860806	3.919414	7.940000	3.601954	3.914530
7.170000	3.396825	3.919414	7.950000	3.684982	3.919414
7.180000	4.192918	3.914530	7.960000	3.704518	3.914530
7.190000	3.733822	3.914530	7.970000	3.636142	3.919414
7.200000	3.904762	3.919414	7.980000	3.543346	3.914530
7.210000	3.885226	3.914530	7.990000	3.851038	3.919414
7.220000	3.636142	3.919414	8.000000	3.621490	3.919414
7.230000	3.870574	3.909646	8.010000	3.826618	3.914530
7.240000	3.494505	3.914530	8.020000	3.455433	3.914530
7.250000	3.435897	3.919414	8.030000	4.231990	3.914530
7.260000	4.105006	3.919414	8.040000	3.641026	3.919414
7.270000	3.753358	3.914530	8.050000	3.738706	3.914530
7.280000	3.997558	3.914530	8.060000	3.992674	3.909646
7.290000	3.689866	3.914530	8.070000	3.601954	3.909646
7.300000	3.426129	3.914530	8.080000	3.870574	3.909646
7.310000	3.982906	3.914530	8.090000	3.772894	3.914530
7.320000	3.680098	3.909646	8.100000	3.816850	3.919414
7.330000	4.002442	3.909646	8.110000	3.709402	3.914530
7.340000	3.851038	3.909646	8.120000	3.758242	3.919414
7.350000	3.865690	3.914530	8.130000	3.709402	3.914530
7.360000	3.416361	3.914530	8.140000	3.821734	3.914530
7.370000	3.904762	3.904762	8.150000	3.641026	3.914530
7.380000	3.953602	3.909646	8.160000	3.802198	3.909646
7.390000	3.494505	3.914530	8.170000	3.597070	3.909646
7.400000	4.158730	3.914530	8.180000	3.694750	3.914530
7.410000	3.738706	3.909646	8.190000	3.533578	3.914530
7.420000	3.992674	3.914530	8.200000	3.338217	3.914530
7.430000	3.816850	3.914530	8.210000	3.855922	3.919414
7.440000	3.665446	3.919414	8.220000	3.797314	3.914530
7.450000	3.738706	3.919414	8.230000	3.694750	3.919414
7.460000	3.592186	3.914530	8.240000	4.100122	3.914530
7.470000	4.241758	3.919414	8.250000	3.548230	3.909646
7.480000	3.724054	3.914530	8.260000	3.797314	3.914530
7.490000	3.743590	3.919414	8.270000	3.728938	3.919414
7.500000	3.787546	3.919414	8.280000	3.377289	3.919414
7.510000	3.557998	3.914530	8.290000	3.523810	3.914530
7.520000	3.670330	3.919414	8.300000	3.831502	3.914530
7.530000	3.787546	3.914530	8.310000	3.689866	3.914530
7.540000	3.758242	3.919414	8.320000	3.631258	3.919414
7.550000	3.557998	3.909646	8.330000	3.963370	3.914530
7.560000	3.489621	3.909646	8.340000	3.514042	3.914530
7.570000	3.606838	3.914530	8.350000	3.802198	3.914530
7.580000	3.611722	3.914530	8.360000	3.548230	3.914530
7.590000	3.645910	3.914530	8.370000	3.601954	3.919414
7.600000	4.227106	3.909646	8.380000	3.973138	3.914530
7.610000	3.753358	3.909646	8.390000	3.636142	3.914530
7.620000	3.938950	3.914530	8.400000	3.489621	3.919414
7.630000	3.855922	3.914530	8.410000	3.411477	3.919414
7.640000	3.675214	3.914530	8.420000	4.505495	3.909646
7.650000	3.357753	3.914530	8.430000	4.202686	3.909646
7.660000	3.626374	3.909646	8.440000	3.670330	3.919414
7.670000	4.402930	3.914530	8.450000	4.017094	3.909646
7.680000	4.080586	3.914530	8.460000	4.002442	3.914530
7.690000	3.689866	3.919414	8.470000	3.577534	3.914530
7.700000	3.724054	3.919414	8.480000	3.357753	3.914530
7.710000	3.719170	3.914530	8.490000	3.963370	3.914530
7.720000	3.914530	3.914530	8.500000	3.631258	3.919414
7.730000	3.787546	3.914530	8.510000	3.855922	3.919414
7.740000	4.090354	3.919414	8.520000	4.007326	3.914530
7.750000	3.641026	3.919414	8.530000	3.772894	3.909646
7.760000	3.758242	3.919414	8.540000	3.719170	3.909646
7.770000	3.694750	3.914530	8.550000	3.557998	3.919414
7.780000	3.606838	3.919414	8.560000	3.724054	3.914530
7.790000	3.851038	3.919414	8.570000	3.626374	3.919414

## E.2 Temperature Data

Following is selected temperature data from several experiments with the single layer experimental setup. The data is arranged in various tables corresponding to specific combinations of channel height, blade height, and rotor angular speed. The experiment was run at an input thermal power of 73.144 W and allowed to reach the steady state, then data was recorded for approximately 10 seconds. The first column is time, in seconds, from the initiation of data collection, the second column is the potentiometer voltage indicating the vertical position of the thermocouple at the exit of the heat sink. This thermocouple was left in place for the duration of the experiment. All temperature measurements are listed in degrees Celsius. The next six columns are the temperatures of the stator analogs.  $T_s$ , as measured by thermocouples in various locations. The first three of these thermocouples are embedded in the top stator analog at increasing radii from the center of the heat sink. The last three are in the bottom stator analog, again at increasing radii. The next column is the temperature measurement of the thermocouple located at the exit of the heat sink  $T_o$ , whose position was discussed earlier. The next column is the temperature of the ambient air,  $T_{\text{amb}}$ . The final two columns are the temperatures at the top and bottom surfaces of the thermal insulation.

Table E.2: This test was run with a rotor angular speed of 3000 rpm, with  $h_b = 1.04$  mm, and  $h_c = 1.6$  mm.

time	disp. V.	$T_{s,1}$	$T_{s,2}$	$T_{s,3}$	$T_{s,4}$	$T_{s,5}$	$T_{s,6}$	$T_o$	$T_{\text{amb}}$	$T_{\text{top}}$	$T_{\text{bot}}$
0.000	4.000	76.326	75.935	76.312	74.073	73.848	74.320	53.118	22.904	37.760	25.662
0.702	4.026	76.331	75.942	76.319	74.079	73.843	74.335	53.160	22.921	37.756	25.666
1.403	3.964	76.338	75.950	76.314	74.086	73.853	74.337	53.059	22.939	37.724	25.666
2.102	3.995	76.333	75.946	76.309	74.073	73.847	74.332	52.954	22.948	37.697	25.671
2.803	4.000	76.340	75.947	76.312	74.083	73.841	74.334	53.055	22.946	37.725	25.666
3.503	4.005	76.343	75.949	76.322	74.091	73.855	74.333	53.050	22.971	37.751	25.676
4.204	4.000	76.336	75.945	76.314	74.085	73.855	74.336	53.035	22.955	37.756	25.676
4.904	4.010	76.342	75.944	76.312	74.076	73.845	74.328	52.959	22.941	37.780	25.661
5.604	4.000	76.342	75.949	76.315	74.075	73.845	74.328	53.082	22.919	37.776	25.657
6.305	4.000	76.341	75.947	76.315	74.081	73.847	74.329	52.931	22.913	37.791	25.669
7.005	3.979	76.343	75.954	76.321	74.077	73.848	74.334	52.837	22.907	37.778	25.670
7.706	3.995	76.342	75.952	76.315	74.081	73.849	74.330	52.920	22.899	37.792	25.664
8.405	4.000	76.349	75.959	76.324	74.088	73.859	74.330	52.970	22.911	37.776	25.671
9.106	4.000	76.354	75.963	76.330	74.090	73.851	74.338	52.876	22.920	37.773	25.675
9.803	3.995	76.346	75.950	76.320	74.069	73.845	74.339	52.982	22.915	37.739	25.665
10.505	4.000	76.357	75.963	76.330	74.089	73.858	74.339	52.912	22.924	37.734	25.667

Table E.3: This test was run with a rotor angular speed of 5000 rpm, with  $h_b = 1.04$  mm, and  $h_c = 1.6$  mm.

time	disp. V.	$T_{s,1}$	$T_{s,2}$	$T_{s,3}$	$T_{s,4}$	$T_{s,5}$	$T_{s,6}$	$T_o$	$T_{amb}$	$T_{top}$	$T_{bot}$
0.000	4.026	58.501	58.070	58.497	58.069	57.801	58.315	39.891	23.045	32.019	25.755
0.701	3.990	58.494	58.073	58.489	58.071	57.800	58.310	39.803	23.043	32.022	25.752
1.400	4.010	58.484	58.060	58.481	58.064	57.802	58.305	39.864	23.046	32.019	25.753
2.101	3.985	58.486	58.071	58.480	58.071	57.804	58.308	39.793	23.039	32.032	25.751
2.802	3.985	58.505	58.079	58.484	58.078	57.817	58.324	39.891	23.059	32.058	25.761
3.504	3.995	58.495	58.062	58.484	58.072	57.796	58.302	39.860	23.049	32.036	25.742
4.203	3.995	58.501	58.069	58.488	58.079	57.811	58.315	39.788	23.053	32.024	25.758
4.903	3.979	58.497	58.080	58.489	58.078	57.809	58.314	39.972	23.051	32.031	25.761
5.605	3.995	58.508	58.081	58.491	58.083	57.818	58.327	39.956	23.051	32.023	25.757
6.306	3.990	58.500	58.077	58.485	58.083	57.811	58.319	39.880	23.050	32.012	25.755
7.003	3.995	58.500	58.077	58.487	58.072	57.807	58.309	39.800	23.052	32.003	25.751
7.705	4.005	58.504	58.077	58.495	58.081	57.813	58.318	39.709	23.065	31.995	25.759
8.402	4.000	58.494	58.078	58.502	58.081	57.817	58.322	39.780	23.068	32.017	25.754
9.104	4.000	58.510	58.078	58.498	58.089	57.827	58.322	39.955	23.080	32.028	25.759
9.807	3.990	58.520	58.088	58.505	58.105	57.822	58.325	39.992	23.090	32.037	25.760
10.508	3.990	58.520	58.084	58.500	58.093	57.824	58.329	39.942	23.088	32.028	25.753

Table E.4: This test was run with a rotor angular speed of 7000 rpm, with  $h_b = 1.04$  mm, and  $h_c = 1.6$  mm.

time	disp. V.	$T_{s,1}$	$T_{s,2}$	$T_{s,3}$	$T_{s,4}$	$T_{s,5}$	$T_{s,6}$	$T_o$	$T_{amb}$	$T_{top}$	$T_{bot}$
0.000	4.077	51.058	50.660	51.033	50.558	50.311	50.803	36.739	22.939	29.785	25.570
0.693	4.021	51.065	50.670	51.038	50.556	50.309	50.804	36.631	22.940	29.792	25.571
1.391	4.021	51.060	50.660	51.032	50.549	50.302	50.790	36.569	22.934	29.789	25.564
2.093	4.010	51.059	50.665	51.032	50.554	50.304	50.801	36.584	22.938	29.792	25.566
2.794	4.021	51.059	50.663	51.037	50.545	50.306	50.797	36.629	22.928	29.786	25.571
3.492	4.026	51.057	50.662	51.032	50.552	50.300	50.792	36.628	22.911	29.774	25.570
4.194	4.041	51.066	50.657	51.033	50.556	50.299	50.797	36.579	22.922	29.795	25.571
4.893	4.015	51.067	50.671	51.040	50.565	50.309	50.801	36.560	22.932	29.807	25.574
5.594	4.031	51.068	50.678	51.040	50.554	50.309	50.797	36.582	22.936	29.818	25.564
6.296	4.031	51.069	50.673	51.036	50.557	50.312	50.795	36.773	22.908	29.836	25.563
6.996	4.036	51.074	50.681	51.048	50.556	50.313	50.808	36.802	22.924	29.859	25.568
7.696	4.026	51.075	50.685	51.047	50.570	50.316	50.805	36.730	22.918	29.879	25.575
8.395	4.036	51.067	50.679	51.045	50.561	50.314	50.793	36.769	22.910	29.896	25.567
9.094	4.057	51.065	50.685	51.040	50.567	50.318	50.798	36.872	22.912	29.914	25.569
9.795	4.046	51.081	50.686	51.053	50.572	50.329	50.814	36.730	22.914	29.934	25.574
10.498	4.010	51.084	50.693	51.053	50.578	50.325	50.806	36.742	22.912	29.964	25.571

Table E.5: This test was run with a rotor angular speed of 5000 rpm, with  $h_b = 0.50$  mm, and  $h_c = 3.4$  mm.

time	disp. V.	$T_{s,1}$	$T_{s,2}$	$T_{s,3}$	$T_{s,4}$	$T_{s,5}$	$T_{s,6}$	$T_o$	$T_{amb}$	$T_{top}$	$T_{bot}$
0.000	4.067	77.293	76.845	77.165	68.490	68.229	68.644	47.583	22.701	37.584	25.300
0.702	4.067	77.299	76.851	77.153	68.495	68.237	68.652	47.622	22.710	37.593	25.305
1.403	4.057	77.303	76.852	77.169	68.505	68.238	68.659	47.524	22.717	37.615	25.293
2.102	4.067	77.308	76.861	77.172	68.508	68.241	68.667	47.567	22.730	37.606	25.307
2.801	4.067	77.311	76.856	77.167	68.502	68.238	68.663	47.571	22.729	37.616	25.297
3.502	4.067	77.309	76.863	77.177	68.504	68.246	68.660	47.493	22.729	37.635	25.304
4.203	4.072	77.305	76.857	77.177	68.505	68.239	68.661	47.388	22.723	37.623	25.295
4.901	4.077	77.322	76.867	77.182	68.510	68.244	68.665	47.410	22.729	37.639	25.298
5.604	4.057	77.304	76.858	77.180	68.495	68.239	68.661	47.385	22.712	37.642	25.293
6.306	4.098	77.316	76.865	77.183	68.504	68.248	68.665	47.592	22.712	37.647	25.304
7.005	4.067	77.308	76.861	77.179	68.499	68.241	68.654	47.718	22.695	37.651	25.296
7.706	4.072	77.313	76.869	77.181	68.498	68.242	68.664	47.905	22.690	37.675	25.303
8.403	4.072	77.327	76.870	77.191	68.501	68.250	68.668	47.996	22.690	37.713	25.310
9.109	4.077	77.313	76.873	77.187	68.501	68.238	68.658	48.105	22.676	37.719	25.302

Table E.6: This test was run with a rotor angular speed of 5000 rpm, with  $h_b = 1.65$  mm, and  $h_c = 3.4$  mm.

time	disp. V.	$T_{s,1}$	$T_{s,2}$	$T_{s,3}$	$T_{s,4}$	$T_{s,5}$	$T_{s,6}$	$T_o$	$T_{amb}$	$T_{top}$	$T_{bot}$
0.000	4.015	53.011	52.534	52.905	51.459	51.191	51.593	34.306	23.105	29.953	25.384
0.702	4.015	53.015	52.545	52.908	51.454	51.195	51.598	34.314	23.116	29.950	25.393
1.402	4.015	53.023	52.557	52.915	51.468	51.203	51.609	34.407	23.125	29.955	25.395
2.103	4.026	53.021	52.556	52.916	51.463	51.189	51.600	34.364	23.115	29.949	25.391
2.804	4.031	53.012	52.542	52.909	51.453	51.187	51.595	34.361	23.111	29.936	25.389
3.504	4.031	53.028	52.551	52.911	51.457	51.182	51.602	34.302	23.123	29.924	25.389
4.205	4.031	53.027	52.548	52.912	51.458	51.184	51.601	34.297	23.123	29.920	25.391
4.905	4.046	53.021	52.542	52.909	51.452	51.185	51.602	34.262	23.121	29.901	25.386
5.605	4.021	53.023	52.542	52.911	51.454	51.197	51.596	34.318	23.130	29.912	25.388
6.306	4.031	53.031	52.544	52.915	51.469	51.195	51.592	34.371	23.139	29.907	25.390
7.006	4.026	53.020	52.545	52.910	51.458	51.193	51.599	34.456	23.108	29.909	25.384
7.703	4.021	53.019	52.559	52.923	51.460	51.199	51.604	34.462	23.109	29.918	25.396
8.405	4.026	53.019	52.553	52.909	51.460	51.196	51.594	34.441	23.088	29.921	25.378
9.107	4.015	53.019	52.556	52.909	51.458	51.192	51.593	34.361	23.087	29.920	25.383
9.804	4.031	53.030	52.560	52.914	51.464	51.197	51.599	34.335	23.078	29.925	25.386
10.503	4.026	53.023	52.552	52.912	51.461	51.187	51.592	34.289	23.065	29.909	25.379



# Bibliography

- [1] V. Egan, P. Walsh, E. Walsh, R. Grimes, Thermal analysis of miniature low profile heat sinks with and without fins, *J. Electron Packaging* 131 (2009).
- [2] G. P. Beretta, E. Malfa, Flow and heat transfer in cavities between rotor and stator disks, *Int. J. Heat Mass Trans.* 46 (2003) 2715–2726.
- [3] Y. Yan, M. Gord, G. Lock, M. Wilson, J. Owen, Fluid dynamics of a pre-swirl rotor-stator system, *J. Turbomachinery* 125 (2003) 641–647.
- [4] R. Webb, Heat exchanger design methodology for electronic heat sinks, *J. Heat Trans.* 129 (2007) 899–901.
- [5] Broad agency announcement: Microtechnologies for air-cooled exchangers (MACE), Broad Agency Announcement, 2008.
- [6] D. Japikse, N. C. Baines, Introduction to Turbomachinery, Concepts ETI Inc., pp. 4–6.
- [7] S. Kakaç, R. Shah, W. Aung, Handbook of Single-Phase Convective Heat Transfer, John Wiley & Sons, p. 3.42.
- [8] S. Kakaç, R. Shah, W. Aung, Handbook of Single-Phase Convective Heat Transfer, John Wiley & Sons, p. 3.31.
- [9] S. Kakaç, R. Shah, W. Aung, Handbook of Single-Phase Convective Heat Transfer, John Wiley & Sons, p. 4.72.
- [10] S. Kakaç, R. Shah, W. Aung, Handbook of Single-Phase Convective Heat Transfer, John Wiley & Sons, pp. 4.34, 4.57, 4.58.
- [11] S. Kakaç, R. Shah, W. Aung, Handbook of Single-Phase Convective Heat Transfer, John Wiley & Sons, pp. 3.35, 4.16, 4.43, 4.74.
- [12] J. Cimbala, Y. Çengel, Fluid Mechanics Fundamentals and Applications, McGraw Hill, pp. 269–270.
- [13] G. Naterer, Heat Transfer in Single and Multiphase Systems, CRC Press LLC, pp. 129–130.

- 
- [14] A. Husain, K. Kim, Multiobjective optimization of a microchannel heat sink using evolutionary algorithm, *J.Heat Trans.* 130 (2008).
- [15] S. Ndao, Y. Peles, M. Jensen, Multi-objective thermal design optimization and comparative analysis of electronics cooling technologies, *Int. J. Heat and Mass Transfer* 52 (2009) 4317–4326.
- [16] D. Lelea, A. Ciobală, I. Laza, L. Mihon, The micro-heat sink with the double-layer single path channels, *Scientific Bulletin of the Politehnica University of Timisoara, Romania Transactions on Mechanics* 54 (2009) 4317–4326.
- [17] E. Cravalho, *Thermal–Fluids Engineering II Course Reader*, pp. 49–51.
- [18] F. M. White, *Fluid Mechanics*, McGraw–Hill, fifth edition, pp. 760–761.
- [19] S. L. Dixon, *Fluid Mechanics and Thermodynamics of Turbomachinery*, Elsevier Butterworth-Heinemann, fifth edition, p. 227.
- [20] F. E. Jørgensen, *How to measure turbulence with hot-wire anemometers – a practical guide*, Dantec Dynamics, 2002.
- [21] I. Lekakis, Calibration and signal interpretation for single and multiple hot-wire/hot-film probes, *Meas. Sci. Technol.* 7 (1996) 1313–1333.
- [22] H. Bruun, C. Tropea, The calibration of inclined hot-wire probes, *J. Phys. E: Sci. Instrum* 18 (1985) 405–413.
- [23] N. E. Kotsovinos, A note on the conservation of the axial momentum of a turbulent jet, *J. Fluid Mech.* 87 (1977) 55–63.
- [24] E. Kausel, *Advanced Structural Dynamics Course Notes*.
- [25] N. Cheremisinoff (Ed.), *Encyclopedia of Fluid Mechanics*, volume 8, Gulf Publishing Company, pp. 881–882.
- [26] M. Spotts, T. Shoup, L. Hornberger, *Design of Machine Elements*, Pearson Education, fifth edition, p. 42.
- [27] H. Rothbart, *Mechanical Design Handbook*, McGraw Hill Companies Inc., p. 5.75.
- [28] C. W. De Silva, *Vibrations and Shock Handbook*, Taylor & Francis Group, LLC, p. 34.20.
- [29] C. W. De Silva, *Vibrations and Shock Handbook*, Taylor & Francis Group, LLC, p. 1.22.